Università degli Studi "Roma Tre"

Dipartimento di Matematica e Fisica
Scuola dottorale in Matematica e Fisica - XXVII Ciclo
Tesi di Dottorato in Fisica

Looking for the broad emission lines in AGN2 with deep NIR spectroscopy

A thesis submitted for the degree of

Doctor of Phylosophy

Author:
Francesca Onori

Tutor:
Prof. Fabio La Franca

Coordinatore:
Prof. Roberto Raimondi

Abstract

Nowadays there is robust evidence that every galaxy hosts a super massive black hole (SMBH; 10^6-10^9 $M_\odot$) and the correlations of its mass with the host galaxy properties have been fairly well estabilished. Indeed the accretion of matter on the supermassive black holes and the related radiative and kinetic power output play an important role in the galaxy evolution, by suppressing/tuning the star formation and feeding the AGN itself (feedback). In this framework, it appears clear that the study of AGN evolution is very important to understand the evolution of the star formation rate and galaxies in the Universe (AGN/galaxy co-evolution). Moreover, the existence of the scaling relationships between the AGN BH mass and the bulge galaxies properties, implies that the evolution of galaxies and the growth of SMBHs are intricately tied together. Thus, in order to obtain a clear picture of the AGN/galaxy co-evolution, it is important to accurately derive the shape and the evolution of both AGNs luminosity and SMBH mass functions.

In the last decade, using hard X-ray selected AGN samples, it has been possible to accurately derive the AGN luminosity function up to z$\sim$4 and, recently, using virial based techniques in the optical band on samples of broad line AGN (AGN 1), it has been possible to obtain some estimates of the Super Massive BH Mass Function (SMBHMF). However these measurements are affected by several selection biases against the narrow line AGN (AGN 2), where the Broad Line Region (BLR) is not visible in the optical because of dust extinction.

According to the original standard unified model the different observational classes of AGN (AGN1 and AGN2) were believed to be the same kind of objects, observed under different conditions (e.g. different orientations to the observer). Instead, nowadays there are indications that AGN1 and AGN2 have on average different accretion rates (smaller for AGN 2), different host galaxy properties (more early type for AGN 2) and different masses (smaller for AGN2). It is therefore fundamental to measure the BH masses of both AGN 1 and AGN 2 in a consistent way.

In the few studies where AGN2 BH masses have been derived the authors used the BH-bulge scale relations which were instead calibrated on AGN1 samples and are unlikely to hold also for all AGN2. It is therefore crucial to directly measure AGN2 BH masses also to verify the validity of the scaling relations for this population of AGNs.

The work performed in this thesis is inserted in this scientific framework. Following the studies of Landt et al (2008; 2011b and 2013) we have developed a new virial method that make use of the less affected by dust exstinction Paβ NIR emission line in combination with the hard X-ray continuum luminosity of the AGN, which suffer less from galaxy starlight contamination. Such a relationship represent a usefull tool since it is potentially able to work also with AGN2, allowing us to derive for the first time a reliable measure of the AGN2 BH masses. To this porpuse we have randomly selected a complete sample of ∼40 obscured and intermediate AGN (AGN2, AGN1.9 and AGN1.8) from the *Swift*/BAT 70 Month hard X-ray survey, which provides an accurate hard X-ray luminosities measurements in the 14−195 keV band. We have observed the selected sources using the NIR spectrographs ISAAC at VLT and LUCI at LBT, and also using the multiwavelenght spectrograph Xshooter at VLT. We found broad component in BLR emission lines (Paα ; Paβ and He I) in ∼30% of our sources and, applying to them the NIR virial estimator, we have been able to measure in a direct way the AGN2 BH masses, finding that AGN2 have on average lower BH masses and higher Eddington ratio with respect AGN1 population of same luminosity.

I'm astounded by people who want to 'know' the universe when it's hard enough to find your way around Chinatown

Woody Allen

The most exciting phrase to hear in science, the one that heralds new discoveries, is not 'Eureka!' (I found it!) but 'That's funny!'

Isaac Asimov

Mi domando se le stelle sono illuminate perché ognuno possa un giorno trovare la sua.

Antoine de Saint-Exupéry, Il piccolo principe.

Alla mia famiglia.

Contents

Chapter 1

Introduction

Nowadays there are robust evidences that every galaxy hosts a super massive black hole (SMBH; 10^6-10^9 $M_\odot$) and the study of this astrophysical black holes (BH) is mainly driven by three different rationales. First of all, the existence of this kind of objects is one of the strongest implications of the theory of General Relativity, and their study can give useful informations on strong gravity effects in action.
Secondly, the emission processes, which allow us to detect such a kind of sources, originate from accretion flows or relativistic jets. Both of these mechanisms take place in regions very close to the BH, thus allowing to study not only the physics of matter in extreme conditions, but also radiative effects and relativistic magnetohydrodinamics.
Lastly, BH affect the formation and evolution of the structures they live in, like galaxies, groups and clusters, and therefore play a key role in a broader cosmological context. This tight link between BH activity and galaxy evolution has been indicated by several discoveries:

- the observation of a supermassive BH (SMBH) in most of the nearby bulge-dominated galaxies (see e.g. Gebhardt et al. 2000, Ferrarese and Merritt 2000, Marconi and Hunt 2003 and and references therein);

- the growth of SMBH happen mainly during active phases, and therefore most local bulge galaxies should have passed an active phase in their lifetime (see Soltan 1982 and Marconi et al. 2004);

- the evolution of active BH (Ueda et al. 2003; Hasinger et al. 2005; La Franca et al. 2005) and of star-forming galaxies (Cowie et al. 1996; Franceschini et al. 1999) have a very similar shape.

Indeed the accretion of matter on the supermassive black holes and the related radiative and kinetic power output play an important role in the galaxy evolution, by suppressing/tuning the star formation and feeding the AGN itself (feedback; Silk and Rees 1998; Fabian and Iwasawa 1999; Croton et al. 2006; Cattaneo et al. 2009 for a review). In this framework, it appears clear that the study of AGN evolution is very important to understand the evolution of the star formation rate and galaxies in the Universe (AGN/galaxy co-evolution). Moreover, the existence of the scaling relationships between the AGN BH mass and the bulge galaxies properties, implies that the evolution of galaxies and the growth of SMBHs are intricately tied together. Thus, in order to obtain a clear picture of the AGN/galaxy co-evolution, it is important to accurately derive the shape and the evolution of both AGNs luminosity and SMBH mass functions.

In the last decade, using hard X-ray selected AGN samples, it has been possible to accurately derive the AGN luminosity function up to z$\sim$4 (Ueda et al. 2003; La Franca et al. 2005; Ebrero et al. 2009) and, recently, using virial based techniques in the optical band on samples of broad line AGN (AGN 1), it has been possible to obtain some estimates of the Super Massive BH Mass Function (SMBHMF). However these measurements are affected by several selection biases against the narrow line AGN (AGN 2), where the Broad Line Region (BLR) is not visible in the optical because of dust extinction.

According to the original standard unified model (Antonucci, 1993), the different observational classes of AGN (AGN1 and AGN2) were believed to be the same kind of objects, observed under different conditions (e.g. different orientations to the observer). Instead, nowadays there are indications that AGN1 and AGN2 have on average different accretion rates (smaller for AGN 2, Winter et al. 2010), different host galaxy properties (more early type for AGN 2) and different masses (smaller for AGN2, Georgakakis et al. 2009, see also Lusso et al. 2012). It is therefore fundamental to measure the BH masses of both AGN 1 and AGN 2 in a consistent way.

In the few studies where AGN2 BH masses have been derived (e.g. Heckman et al. 2004 from SDSS), the authors used the BH-bulge scale relations which were instead calibrated on AGN1 samples and are unlikely to hold also for all AGN2 (see Graham 2008 and Kormendy et al. 2011). It is therefore crucial to directly measure AGN2 BH masses also to verify the validity of the scaling relations for this population of AGNs. Moreover, different studies have shown that AGN 2 are representative of a population of AGN characterised by low intrinsic X-ray luminosity and low BH masses (Tueller et al., 2010) that likely contain clues about the formations of the first BH.

The work performed in this thesis is inserted in this scientific framework. Following the studies of Landt et al. (2008); Landt et al. (2011) and Landt et al. (2013) we have developed a new virial method that make use of the less affected by dust exstinction Paβ NIR emission line in combination with the hard X-ray continuum luminosity of the AGN, which suffer less from galaxy starlight contamination. Such a relationship represent a usefull tool since it is potentially able to work also with obscured AGN, allowing us to derive for the first time a reliable measure of the AGN2 BH masses. To this porpuse we have randomly selected a complete sample of ∼40 obscured and intermediate AGN (AGN2, AGN1.9 and AGN1.8) from the *Swift*/BAT 70 Month hard X-ray survey, which provides an accurate hard X-ray luminosities measurements in the 14−195 keV band. We have observed the selected sources using the NIR spectrographs ISAAC at VLT and LUCI at LBT, and also using the multiwavelenght spectrograph Xshooter at VLT. We found broad component in BLR emission lines (Paα ; Paβ and He I) in ∼30% of our sources and, applying to them the NIR virial estimator, we have been able to measure in a direct way the AGN2 BH masses, finding that AGN2 have on average lower BH masses and higher Eddington ratio with respect AGN1 population of same luminosity.

A general overview of the AGN phenomena, their physical and observational characteristics and their classification in the framework of the unified model are summarized in Chapter 2, while in Chapter 3 the main methods to derive the AGN BH mass estimates are described. The project, the *Swift* catalog, the sample selection, the observations and data reductions steps are described in Chapter 4. The development of the new NIR virial relations and the first main results are accurately described in Chapter 5, while the line fitting procedures and the finding of broad component of Paschen lines in AGN2 spectra are discussed in the Chapter 6. Finally the measure of the AGN2 BH masses and the related results are described in Chapter 7 and the conclusions and the future applications of this work are discussed in Chapter 8.

Chapter 2

Active Galactic Nuclei

This Chapter aims at providing a very brief introduction on the physics of Active Galactive Nuclei (AGN), and their evolution in the context of galaxy formation and evolution models. A more detailed discussion can be found in Peterson (1997) and Krolik (1998) textbooks. For the evolutionary topics, see also Merloni and Heinz (2013).

2.1 Basic concepts

The term *Active Galactic Nuclei* (AGN) is used to describe galaxies with energetic phenomena in their nuclei, or central regions, that cannot be clearly and directly attributed to stellar activity. *Seyfert galaxies* and *quasars* represent the largest subclasses of AGN; the fundamental difference between these two classes is the amount of emitted radiation: while in a Seyfert galaxy the luminosity of the central source at visible wavelengths is comparable to the luminosity of the whole galaxy, in a quasar the central source may be up to 100 times brighter.

There are some peculiar features that are usually present in an AGN, although not necessary at the same time, including:

- small, unresolved angular size;

- nuclear broad-band emission, over a wide portion of the electromagnetic spectrum;

- strong nuclear emission lines, mainly found in the infrared and optical/UV part of the spectrum;

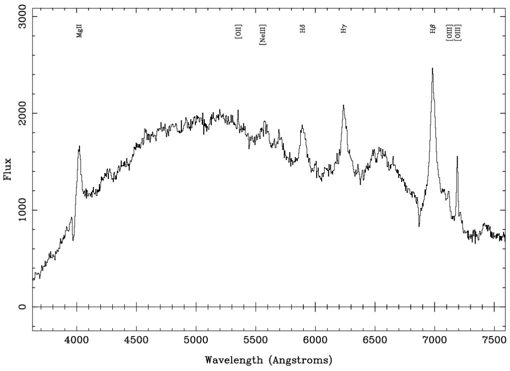

FIGURE 2.1. Optical spectrum of a typcal Seyfert 1 (adopted from Hawkins 2004)

- variability, both in the continuum emission and in the emission lines, especially in the X-rays;

- higher degree of polarization (0.5-2%) with respect to the normal galaxies.

AGN have been classifed on the basis of their emission in the optical, X-ray and radio band. In the optical/UV band, the classification is based on the shape of the emission lines; it is possible to distinguish between two main groups:

Broad-line emission galaxies (or *Type-1* AGN, AGN1) show two separate emission line systems: broad lines corresponding to permitted transitions (e.g. Lyα , C IV , Mg II , Balmer hydrogen lines) in a gas with $v \gtrsim 10^4$ Km s^{-1} , and narrow lines corresponding to forbidden transitions (e.g. [Ne IV] , [Ne V] , [O II] , [O III]) in an ionized gas with low density ($n_e = 10^3$ - 10^6 cm^{-3} and $v \simeq 10^2$ Km s^{-1} . An example of a typical spectrum of a Type-1 AGN is shown in Figure 2.1.

Narrow-line emission galaxies (or *Type-2* AGN, AGN2) are only characterized by narrow emission lines, from both permitted and forbidden transitions. In Type-2 AGN the continuum emission is weaker with respect to the continuum seen in Type-1 AGN, and is almost flat. Figure 2.2 shows an example of a typical spectrum of a Type-2 AGN.

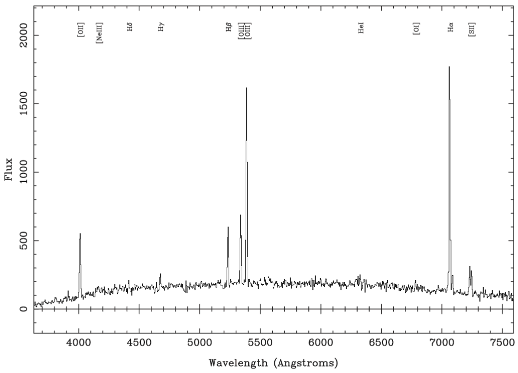

FIGURE 2.2. Optical spectrum of a typcal Seyfert 2 (adopted from Hawkins 2004)

In the X-rays the absorption effect is weaker than in the optical/UV band, but it is still able to induce variations in the spectrum. The obscuration in the X-ray band is usually parametrized in term of the *column density* N_H , which represents the number density per unit area of hydrogen-equivalent atoms integrated along the line of sight. The presence of this material induces a flattening in the low energy part of the X-ray spectrum; the cutoff energy depends on the N_H and increases for increasing N_H . AGN with $N_H < 10^{22}$ cm^2 are usually defined as *unobscured* (or *unabsorbed*) AGN, while AGN with $N_H > 10^{22}$ cm^2 are defined as *obscured* (or *absorbed*) AGN. The latter are further divided in two classes of absorption.
The observed absorbed flux F$_{obs}$ can be written as:

$$F_{obs}(\lambda) = F_{int}(\lambda)e^{-\tau}, \tag{2.1}$$

where F_{int} is the intrinsic unabsorbed flux and τ is the *optical depht*:

$$\tau = \int \sigma_T \cos\theta n(r)dr = N_H\sigma_T, \tag{2.2}$$

where the integral is defined along the line of sight, $n(r)$ is the number density, θ is the angle to the normal and σ_T= 6.65×10^{-25} cm^{-2} is the Thomson cross-section. If τ >1, the source becomes optically-thick, and it is opaque to the optical/UV and X-ray photons. This happens when $N_H \geq 1/\sigma_T$ ($\sim 10^{24}$ cm^{-2}); sources with N_H >10^{24} cm^{-2} are therefore defined as *Compton-thick* AGN, while absorbed sources with N_H <10^{24} cm^{-2} are usually defined as *Compton-thin* AGN.

At radio wavelength, AGN have been divided in two main groups, depending on the intensity of their radio emission. A fraction of $\sim 10\%$ of the AGN population is defined as *radio-loud*, while the remaining sources are *radio-quiet*. However, the criterion used to distinguish between these two classes is not well defined.

2.2 Inner structure

The most bright AGN may emit *bolometric* luminosities (emitted across the whole electroelectromagnetic spectrum) as high as 10^{48} erg s^{-1} , in a volume that is significantly smaller than a cubic parsec. The fundamental question about AGN is then how this great amount of energy is generated.

It is widely accepted that the central engine of AGN consists in a supermassive black hole (SMBH) surrounded by an accretion disk, where the material in gravitational infall dissipates its kinetic energy. This accretion disk is then heated to high temperatures and it is thus responsible of most of the observed radiation.

It is possible to estimate the mass of the SMBH by assuming that the accreting material is a fully-ionized hydrogen gas, and that the central source is stable and isotropic. The radial component of the gravitational force acting on an electron-proton pair, with masses m_e and m_p respectively, is:

$$F_{grav} = -\frac{GM(m_p + m_e)}{r^2} \simeq -\frac{GMm_p}{r^2}, \tag{2.3}$$

where M is the mass of the central source. For high energy production rates, the radiation pressure due to Thomson electron scattering become important on the accreting gas. The radial component of the outward force on a single electron due to radiation pressure is given by:

$$F_{rad} = \sigma_T \frac{L}{4\pi r^2 c}, \tag{2.4}$$

where L is the luminosity of the source. To avoid disintegration of the source, the outward radiation force must be balanced by the inward gravitational force. Therefore, the luminosity of the source must not exceed a maximum allowed value, the *Eddington luminosity* (L_{Edd}) :

$$L_{Edd} = \frac{4\pi G c m_p M}{\sigma_T} \simeq 1.26 \times 10^{38} \frac{M}{M_\odot}\ erg\, s^{-1}. \tag{2.5}$$

If we consider sources with bolometric luminosity $L_{bol} = 10^{46}$- 10^{48} erg s^{-1} , a central mass of 10^8-10^{10} $M_\odot$ is obtained from Equation 2.5.
Another key question is how efficiently the accreted mass is converted into radiated energy. The rate at which energy is emitted by the nucleus is

$$L = \epsilon \dot{M} c^2, \tag{2.6}$$

where ϵ is the *radiative efficiency* and $\dot{M}$ = dM/dt is the *mass accretion rate*. The potential energy of a mass m at a distance r from the central source of mass M is $U = GMm/r$, so the luminosity of the source can be written as:

$$L \simeq \frac{dU}{dt} = \frac{GM\dot{M}}{r}. \tag{2.7}$$

Combining Equations 2.6 and 2.7 we obtain:

$$\epsilon = \frac{GM}{c^2 r} = \frac{1}{2}\frac{R_S}{r}, \tag{2.8}$$

where we have introduced the *Schwarzschild radius* $R_S = 2GM/c^2$. The bulk of the emission of the optical/UV emission from the accretion disk is believed to be produced at $r \simeq 5R_S$. Therefore, this simple calculation suggest that $\epsilon \simeq 0.1$. With this radiative efficiency, a relatively low accretion is requested to fuel even a fairly high luminosity source (e.g. $\dot{M} \simeq 2\ M_\odot \mathrm{yr}^{-1}$ for $L \simeq 10^{46}$ erg s^{-1}). However, the value of the radiative efficiency depends on how the accretion actually occurs, though $\epsilon \simeq 0.1$ is a fairly good approximation.

2.3 Continuum emission

The AGN *Spectral energy distribution* (SED) is quite complex, and spans a very wide range of wavelengths, from radio to γ-rays. At a first order approximation, it can be described with a power-law:

$$F_\nu \propto \nu^{-\alpha}, \tag{2.9}$$

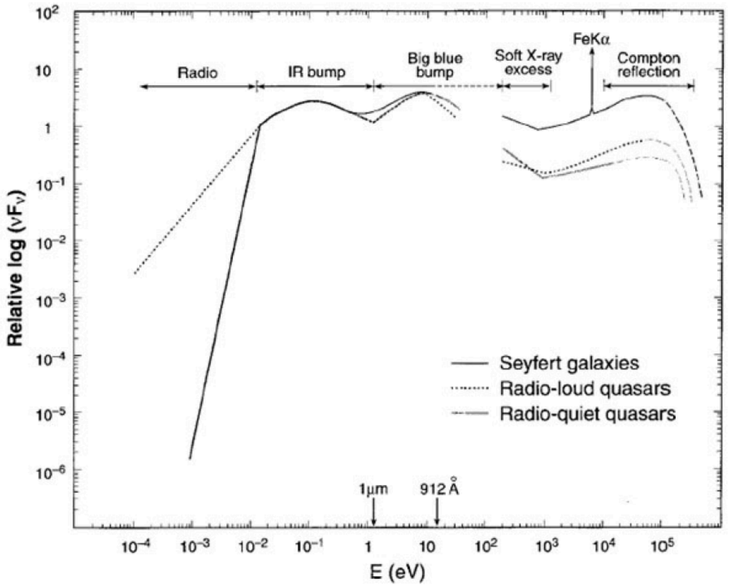

FIGURE 2.3. SED from radio to X-rays of a Seyfert galaxy, a radio-loud quasar and a radio-quiet quasar (adopted from Koratkar and Blaes (1999))

where the *energy index* α is usually found in the range $0 < \alpha < 1$.
As an example, Figure 2.3 shows typical SED of a a Seyfert galaxy, a radio-loud quasar and a radio-quiet quasar. The gap in the UV part of the spectrum, between 912 $\AA$ (the *Lyman continuum edge*) and $\sim$ 100 $\AA$ is due to absorption by neutral hydrogen in our own Galaxy, which makes any detection impossible at these wavelenghts.

While a power-law representation is a reasonable description of the SED when looking over several decades of frequency, a deeper analysis reveals many features, suggesting that the continuum emission is produced by different processes in different regions of the spectrum.

A great amount of energy is emitted in a feature that dominates the spectrum at wavelengths shorter than 4000 $\AA$ and extends beyond 1000 $\AA$, the so called *big blue bump*. In the X-ray region, AGN spectra usually show a sharp rise with decreasing photon energy, the *soft X-ray exces*, that may be the high energy end of this feature. The big blue bump is attributed to a thermal emission with T$\sim$$10^5$ K.

As a first order approximation we can assume that the accretion disk radiates locally like a blackbody:

$$B_\nu = \frac{2h\nu^3}{c^2}\frac{1}{e^{h\nu/kT(r)}-1}, \tag{2.10}$$

where $T(r)$ is the disk temperature at a distance r from the center. Under the assumption that the disk is geometrically thin (and optically thick), it is possible to obtain the total specific luminosity of the disk by integrating over the full range of radii:

$$L_\nu = \frac{4\pi^2 h\nu^3 \cos i}{c^2}\int_{R_{in}}^{R_{out}} \frac{r dr}{e^{h\nu/kT(r)}-1}, \tag{2.11}$$

where i is the inclination angle of the disk to the plane of the sky, and R_{in} and R_{out} are the inner and outer boundaries of the disk, respectively.

At low frequencies, $h\nu \ll kT(R_{out})$, the emission follows the Rayleigh-Jeans approximation (i.e. $B_\nu \propto \nu^2$), while in the high-frequency regime the Wien law holds (i.e. $B_\nu \propto \nu^3 e^{-h\nu/kT}$). The thermal spectrum at intermediate frequencies, where indeed most of the energy is emitted, can be also approximated in a simple fashion, by assuming $R_{out} \gg R_{in}$. This approximation holds when there is a wide range of temperatures in the disk; otherwise, the emitted spectrum should look fairly close to a single-temperature blackbody spectrum. If we further assume that $R_{in} \simeq R_S$ and $R_{out} \to \infty$ we obtain from Equation 2.11 that $L_\nu \propto \nu^{1/3}$. An important prediction of this simple model is that the UV radiation and the optical radiation are emitted mostly in different parts of the disk.

The infrared continuum has probably a thermal origin, as supported by several pieces of evidence. Most AGN show a local minimum in their SED around 1 μm, which may represent the transition region between the hot thermal emission from the accretion disk and a cooler ($T \lesssim 2000K$) thermal emission. Hot dust grains in the nuclear regions have indeed a temperature around 2000 K; higher temperatures should induce sublimation of dust grains. This temperature limit allows to explain the constancy of the frequency where the infrared spectrum is weakest with a Wien cut-off of a 2000 K blackbody. Some observations show that the far infrared spectrum decreases rather sharply at higher wavelength, with a spectral index of $\alpha \lesssim -2.5$. A thermal spectrum can produce a cut-off this sharp because the emitting efficiency of dust grains has a strong dependence on the frequency ($Q_\nu \propto \nu^\gamma$, with $\gamma \sim 2$). Therefore, the emitted spectrum can have a very strong frequency dependence, $F_\nu \propto \nu^{2+\gamma}$.

The mid infrared part of the spectrum is also characterized by several emission bands from Polycyclic Aromatic Hydrocarbons (PAH). PAH are carbon-based molecules that are excited in the regions of star formation, and have characteristic infrared bands at 3.29, 6.2, 7.7, 8.7, 11.3 and 12.7 μm; other weaker features are present at other wavelengths, in the range 3−15 μm. Silicates also play an important role at mid infrared wavelengths: bands around 10 and 18 μm are often observed in obscured AGN and high infrared luminosity galaxies.

The X-ray emission accounts for typically $\sim 10\%$ of the bolometric luminosity of AGN. With its rapid variability, on timescales of the order of a day, it provides a probe of the innermost regions of the source. Historically, the X-ray region of the SED has been divided in *soft* X-rays ($\sim$ 0.1−2 keV) and *hard* X-rays ($\sim$ 2−100 keV), due to the different technologies used in the observations. In X-ray astronomy, SEDs are usually fitted in photons per keV rather than in energy per unit frequency, $P_E \propto E^{-\Gamma} \propto \nu^{-\gamma}$ [$\mathrm{photons\,s^{-1}\,keV^{-1}}$]; in units of energy flux we have:

$$F_\nu \propto \nu^{-\Gamma+1} \propto \nu^{-\alpha}, \tag{2.12}$$

where α is called *energy index* and $\Gamma = \alpha+1$ is called *photon index.* Figure 2.4 shows the average total X-ray spectrum of a Type-1 AGN, as well as the various components that contribute to the spectrum. Soft X-ray region is usually well fitted with a power law with $\alpha \gtrsim 1$, while in the hard X-ray region a flatter slope ($\alpha \sim$ 0.7−0.9) is required. At higher energies, fits to the X-ray spectrum of Seyfert galaxies suggest a high-energy cut-off around a few hundreds keV. At even higher energies, only blazar-type sources (i.e. those with a strong beamed component) have been observed.

The origin of the X-ray emission is ascribed to inverse-Compton scattering of low energy photons by more energetic electrons. The basic idea is that the optical/UV photons emitted from the accretion disk are scattered to higher energies by hot (probably relativistic) electrons in a corona surrounding the disk (this process is usually called *Comptonization*).

In addition to the basic power-law described above, AGN spectra show several indipendent features. As already discussed, in the soft X-ray region many AGN show a soft excess, usually explained as the Comptonized Wien tail of the big blue bump. At low energies ($h\nu \lesssim$ 2 keV), absorption of heavy elements with

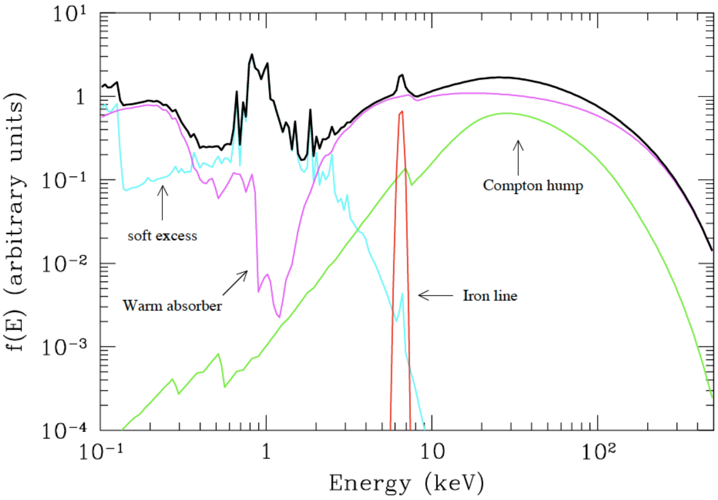

FIGURE 2.4. Average total X-ray spectrum (thick black line) of a Type-1 AGN. Thin lines show the main components of the spectrum (adopted from Risaliti and Elvis 2004).

column densities around $\sim 10^{22}$cm^{-2} are also often observed; these are commonly referred to as *warm absorbers*. In the high energy region ($h\nu \gtrsim 10$ keV) AGN spectra rise above the power-law spectrum. This feature is attributed to Compton reflection of high energy photons on a lower energy electron gas, perhaps the disk itself.

The radio continuum has clearly a non-thermal origin, and it is associated to synchrotron emission. There are at least two pieces of evidence for a non-thermal emission. The spectral index is almost flat, but it becomes progressively steeper at shorter wavelengths. This behavior is characteristic of optically thick sources that undergo continued injection of higher energy electrons. Low energy cutoffs, attributed to synchrotron self-absorption, are detected in some sources, with a frequency dependence weaker than expected ($F_{nu} \propto \nu^{5/2}$). This dependence, as well as the flatness of the spectral index, are usually explained with the complexity of the source structure.

The specific intensity I_ν of a radio source at a given frequency can be determined by measuring the flux and angular size of the source. It is possible to associate to the source an equivalent temperature T_B (the *brightness temperature*), defined as the temperature that the source would have if it was indeed radiating like a blackbody. At radio wavelengths, the Rayleigh-Jeans approximation holds for any temperature, so for an optically thick thermal source the intensity is given by the Planck function B_ν for $h\nu \ll kT$:

$$I_\nu = \frac{F_\nu}{\pi\theta^2} = B_\nu = \frac{2kT_B}{\lambda^2}, \tag{2.13}$$

where F_ν is the observed flux at a frequency $\nu = c/\lambda$ and θ is the angular size of the source. Measurements of F_ν and θ for several compact extragalactic radio sources constrain T_B in the range $10^{11}-10^{12}$ K, which clearly rules out a thermal origin for radio emission.

2.4 The Unified Model of AGN

The presence of both strong high ionization and low ionization narrow lines is common to both types of AGN, and with similar line ratios. This suggested that all AGN are powered by the same intrinsic engine and led to the formulation of the standard Unifed Model for AGN (Antonucci 1993; Urry and Padovani 1995). In this scenario, the observed differences between Type-1 and Type-2 AGN arise from orientation dependence, while the basic source structure remains the same. There is indeed abundant evidence that AGN have axisymmetric structure, and thus radiates anisotropically. The observed properties of a particular source thus depend on the location of the observer.
The current paradigm is built around a central engine, that consists of an accretion disk surrounding a supermassive black hole ($M_{BH} \gtrsim 10^6 \mathrm{M}_\odot$). Relativistic jets emerge from the central region along the disk axis, emitting Doppler-boosted radiation via synchrotron emission and inverse Compton scattering mechanisms. The broad lines observed in Type-1 AGN are thought to be produced in the *Broad Line Region* (BLR), a dense ($\mathrm{n}_e \gtrsim 10^9 \mathrm{cm}^2$) gas region nearby the central source (within a few thousands gravitational radii), where the influence of the gravitational field of the BH is strong. On parsec scales, the entire system is enshrouded in a dusty torus that is opaque to most of the electromagnetic radiation. The torus plays a key role in the framework of the Unified Model, since it allows the direct observation of the central region (including the BLR) only along particular directions. Narrow lines are generated in distant (on torus scale), rarefied gas regions, where the gravitational influence from the BH is less intense, the *Narrow Line Region* (NLR).
Therefore, an observer looking at the AGN on the torus plane (i.e. edge-on)

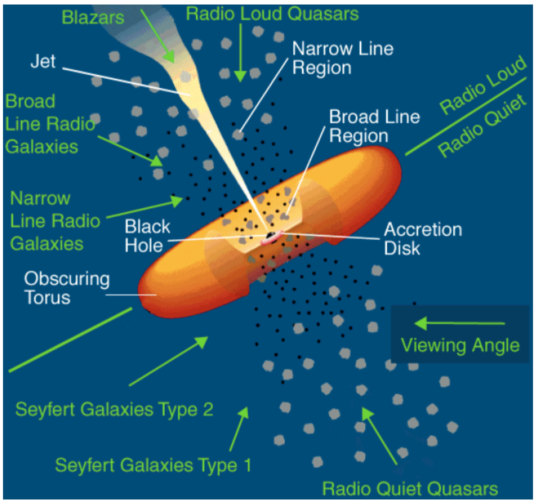

FIGURE 2.5. The Unified Model of AGN. Green arrows show the lines of sight associated whith each class of object.

has the view of the innermost regions (that produce the optical/UV and soft X-ray continuum) and of the BLR obstructed by the intercepting material. Only narrow emission lines are directly visible in this case. An observer looking along the axis has instead a direct view of both the BLR and the NLR, as well as the accretion disk continuum emission (Figure 2.5).

One of the most convincing evidences in favor of this model is the detection of broad optical lines in the polarized spectra of Type-2 AGN. This suggests that the BLR is still present in Type-2 nuclei, but is actually hidden from our line of sight due to the obscuring material. However, the emitted light is scattered in our direction from material distributed on larger scales. Such reflected light is very weak compared to the light of the galaxy, but it has a high degree of polarization, and therefore can be detected in the polarized spectrum.
Although this simple model has allowed to explain much of the complex AGN phenomenology, there is evidence supporting that additional effects are requested to explain the differences between Type-1 and Type-2 AGN, like the discovery of Type-2 sources without broad optical lines in the polarized spectrum.

2.5 Number counts and luminosity function

In order to describe how the AGN population has changed during cosmic time, several statistical technique have been employed. The simplest observational tool that can be used to describe the evolution of a sample of objects are the number counts. By number counts one typically means the surface density in the sky of a given class of sources as a function of the limiting flux of the observations.

More informations can be drawn from the *luminosity function* (LF), defined as the number of sources per unit volume and luminosity with luminosity in the range between L and $L + dL$:

$$\Phi(L) = \frac{dN}{dV dL} \tag{2.14}$$

Let us assume that the local universe is Euclidean and filled with sources with LF $\Phi(L)$. Sources with luminosity L can be observed out to a distance $r = (L/4\pi S)^{1/2}$, being S the limiting flux of the observations. The number counts of sources over the solid angle Ω are then:

$$N(> S) = \int_{L_{min}}^{\infty} \frac{1}{3}\Omega r^3 \Phi(L) dL = \frac{1}{3}\frac{\Omega}{(4\pi)^{3/2}} S^{-3/2} \int_{L_{min}}^{\infty} L^{3/2}\Phi(L) dL \tag{2.15}$$

where $L_{min}(r)$ is the faintest luminosity that can be observed over a flux limit S out to a distance r_{max}. Therefore, the slope of the cumulative number counts of a (non-evolving) class of objects in an Euclidean universe is fixed to $-3/2$.

In a more general case, the correct relativistic expression for number counts differs from Equation 2.15, due to cosmological effects. Radiation emitted at frequency ν' is observed at a redshifted frequency $\nu = \nu'/(1 + z)$, and therefore the observed flux density depends on the shape of the spectrum of the source. Moreover, curvature effects modify the volume element per unit redshift, making it smaller at increasing z.

The simplest general approach to describe the evolution of a LF is by defining two functions $f_d(z)$ and $f_l(z)$ that take into account the evolution of the number density and luminosity, respectively:

$$\Phi(L, z) = f_d(z)\Phi(L/f_l(z), z = 0). \tag{2.16}$$

In the *pure luminosity evolution* (PLE; Mathez 1976) scenario, the comoving number density of sources is constant (so $f_d = cost$), but luminosity varies with cosmic time. In the *pure density evolution* (PDE; Schmidt 1968) case the shape of the LF and the source luminosity are fixed ($f_l = cost$), while the comoving density of sources of any luminosity varies.

While the PDE models fails to describe the observed quasar number counts and overpredicts the cosmic X-ray Background (CXRB), the PLE model tends to overpredict the number of SMBH whith M_{BH} >$10^{10}M_{\odot}$. Therefore, more complex models have been developed throughout the years.

The most accurate description of the overall evolution of the LF comes from deep X-ray surveys. While for optically selected quasar the PLE model still provide a good fit of the data, the *luminosity dependent density evolution* (LDDE) model is invoked to describe the evolution of the X-ray LF (Ueda et al. (2003), see also Hasinger et al. (2005) for soft X-ray selected AGN). As in the PDE model, the redshift evolution of the LF is described as

$$\frac{d\Phi(L_X,z)}{dlog(L_X)} = \frac{d\Phi(L_x,z=0)}{dlogL_X}e(L_X,z), \tag{2.17}$$

where the local LF is usually represented with a power-law with two different indexes, for low and high luminosities:

$$\frac{d\Phi(L_X,z=0)}{dL_X} = \begin{cases} AL_\star^{\gamma_1-\gamma_2}L_X^{-\gamma_1} & L_X \leq L_\star \\ AL_X^{\gamma_2} & L_X > L_\star \end{cases} \tag{2.18}$$

and the evolution factor $e(z)$ is defined as:

$$e(z) = \begin{cases} (1+z)^{p_1} & z \leq z_c(L_X) \\ e(z_c)[(1+z)/(1+z_c(L_X))]^{p_2} & z > z_c. \end{cases} \tag{2.19}$$

The z_c parameter represents the redshift at which the evolution stops. The parameters p_1 and p_2 characterize the rate of the evolution and the rate of counterevolution for $z > z_c$ respectively.

The LDDE model is obtained by introducing a luminosity dependence of z_c, assumed to be a power-law (La Franca et al., 2005):

$$z_c(L_X) = \begin{cases} z_c^\star & L_X \geq L_a \\ z_c^\star(L_X/L_a)^\alpha & L_X < L_a. \end{cases} \tag{2.20}$$

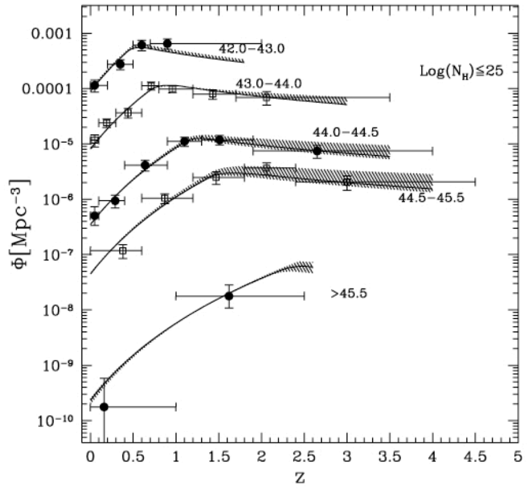

FIGURE 2.6. The space density of AGN as a function of redshift in different luminosity bins. Solid lines show the best-fit values in LDDE model with evolving N_H depending on L_X and z. Adopted from La Franca et al. (2005).

It has been shown that (a) the peak of the AGN space density moves to smaller redshift with decreasing luminosity, and (b) the rate of evolution from the local Universe to the peak redshift is slower for less luminous AGN (*downsizing*; see Figure 2.6.)

It appears that SMBH generally grow in an anti-hierarchical fashion, i.e. while more massive SMBH ($10^{7.5}$– $10^9 M_\odot$) in rare, luminous AGN could grow efficiently at $z = 1 - 3$, smaller SMBH in more common, less luminous AGN had to wait longer to grow ($z < 1.5$).
There is also strong evidence on the redshift and luminosity dependence of the fraction of obscured (N_H >10^{22} cm^{-2}) AGN, indeed it has been shown that this fraction increases with decreasing luminosity (Ueda et al. 2003; La Franca et al. 2005; Treister and Urry 2005) and increasing redshift (La Franca et al. 2005; Treister and Urry 2006; Hasinger 2008).
Attempts to constrain models for galaxy formation and evolution from the optical and X-ray luminosity functions were made in the last decade by several authors (see e.g. Granato et al. 2001; Granato et al. 2004; Di Matteo et al. 2005; Menci et al. 2004: Menci et al. 2005). The predictions of these models are in good agreement with some of the observations, like the downsizing trend; however, they overestimate by a factor of ∼ 2 the space density

of low-luminosity Seyfert-like AGN at $z = 1.5 - 2.5$.

2.6 X-ray surveys and the X-ray background

AGN are powerful X-ray emitters. The discovery of the cosmic X-ray background (CXRB; Giacconi et al. 1962) opened up a privileged window for the study of the energetic phenomena associated with accretion onto black holes. The X-ray sky is almost dominated by the AGN population, due to the relative weakness of the other X-ray emitters (mostly X-ray binaries, but also magnetically active stars and cataclysmic variables), at least down to the faintest fluxes probed by current X-ray telescopes. The goal of reaching a complete census of evolving AGN has therefore been intertwined with that of fully resolving the CXRB into individual sources.

In the last decade, the launch of modern X-ray telescopes like *Chandra* (NASA) and *XMM-Newton* (ESA) has enabled strong observational progress. Sensitive imaging spectroscopy in the 0.5−10 keV band with up to 50−250 times the sensitivity of previous missions, as well as high quality positional accuracies (up to $\sim 0.3{-}1$" for Chandra) were made available for X-ray astronomy studies. Deep extragalactic surveys have probed the X-ray sky down to extremely faint fluxes (as low as $\sim 10^{-17}$ erg s^{-1} cm^{-2} in the 0.5−2 keV band and $\sim 10^{-16}$ erg s^{-1} cm^{-2} in the 2−8 keV band), thus making available large source samples for statistical X-ray source population studies.

With these deeper and larger X-ray surveys that have been performed, a new generation of synthesis model for the CXRB has been developed (see Gilli et al. 2007; Treister et al. 2009). These new models have progressively reduced the uncertainties in the N_H absorption distribution, providing an almost complete census of the unobscured and moderately obscured AGN populations. These sources dominate the X-ray counts in the lower energy band, where almost all the CXRB radiation has been resolved into individual sources.

However, at the peak energy of the CXRB (around ~ 30 keV), only a small fraction ($\sim 5\%$) of the emission has been resolved into individual sources. CXRB synthesis models ascribe a substantial fraction of this unresolved emission to Compton-thick AGN. Gilli et al. (2007) model requires a population of Compton-thick AGN as large as that of Compton thin AGN to fit the residual background emission. Still, the redshift and luminosity distribution of

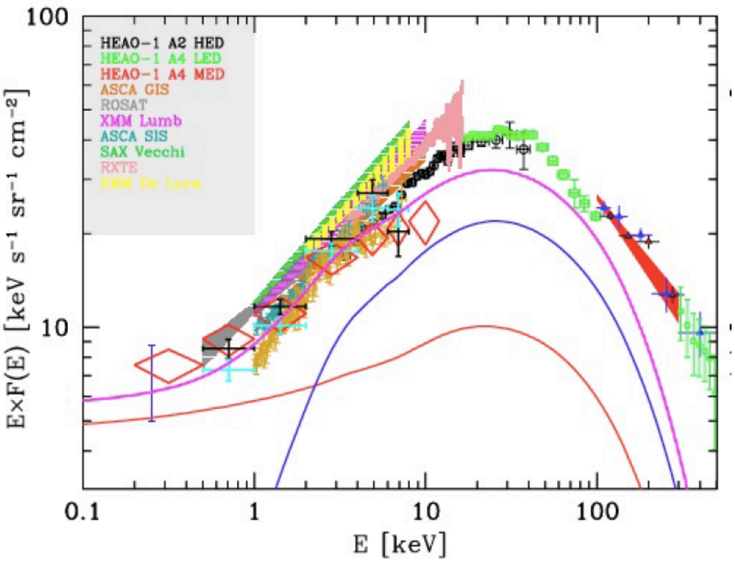

FIGURE 2.7. Observed spectrum of the extragalactic CXRB from several X-ray satellites data. The solid magenta line shows the prediction of the Gilli et al. (2007) model for AGN (unobscured + Compton-thin) and galaxy clusters; red and blue solid lines represent the contribution from unobscured and Compton-thin AGN respectively. Adopted from Gilli et al. (2007)

these sources is essentially unknown, due to their faintness even at hard X-ray energies. The quest for the physical characterization of this missing AGN population represents one of the last current frontiers of the study of AGN evolution.

2.7 SMBH growth in galaxies

In the early 1990s, deep optical surveys of star-forming galaxies began to probe the cosmological evolution of the rate at which stars are formed within galaxies, thus providing robust constraints for models of galaxy formation and evolution (see Madau et al. (1996)). It was soon clear that the QSO (optical) luminosity density and the *Star Formation Rate* (SFR) density evolved in a similar fashion, being much higher in the past, with a broad peak around z∼2 (Boyle and Terlevich, 1998).

Direct measures of the SMBH masses can be obtained from stellar dynamics or spectral analysis of circumnuclear dust and gas. However, it has been possible to perform these measures only for a small (∼50) number of SMBH, due to limitations induced by spatial resolution. With these measures available, it has been observed that the SMBH mass (M_{BH}) correlates tightly with some structural parameters of the host galaxy, like the host spheroid mass (Kormendy and Richstone 1995; Marconi and Hunt 2003), luminosity (Magorrian et al. 1998; Sani et al. 2011) and stellar velocity dispersion (Ferrarese and Merritt 2000; Gebhardt et al. 2000).

Direct or indirect (from scaling relations) knowledge of the SMBH masses allows to test the classical "Soltan argument" (Soltan (1982)), according to which the local mass budget of SMBH in galactic nuclei should be accounted by integrating the overall energy density released by AGN, assuming an appropriate radiative efficiency parameter. The total accreted mass can be computed as a function of redshift:

$$\rho_{BH} = \int_{z}^{z_s} \dot{\rho}_{BH}(z)\frac{dt}{dz}dz, \tag{2.21}$$

where the black hole accretion rate density $\dot{\rho}_{BH}(z)$ is given by:

$$\dot{\rho}_{BH}(z) = \frac{1-\epsilon}{\epsilon c^2}\int \Phi(L_{bol}, z)dL_{bol}, \tag{2.22}$$

were $\Phi(L_{bol}, z)$ and L_{bol}=$\epsilon\dot{M}c^2$ represent the bolometric LF and the bolometric luminosity respectively.

This computation has been performed either using the CXRB as a "bolometer" to derive the total energy density released by the accretion process (Fabian and Iwasawa, 1999), or by considering evolving AGN luminosity functions (Yu and Tremaine 2002; Marconi et al. 2004; Merloni and Heinz 2008). This approach represents a major success of the standard paradigm of accreting black holes as AGN power-sources, as the radiative efficiencies requested in order to explain the local relic population are within the range ϵ= 0.06−0.20, predicted by standard relativistic accretion disc theory.

These evidences suggest that a tight link should exist between SMBH growth and host galaxy evolution. Many processes have been proposed which could forge this direct connection, including galaxy major mergers, star formation winds and AGN-driven outflows. From a physical point of view, these feedback mechanisms by which AGN can regulate the growth of their host galaxies can be distinguished into two main modes.

The first mode is associated with the phases of fast SMBH growth in bright AGN. Star formation and SMBH growth are fueled by the same cool gas located in the inner regions of the galaxy. The fast, explosive energy injection from the central source can heat and disperse this gas, thus quickly terminating both star formation and SMBH growth. In this scenario (*quasar mode* feedback; see e.g. Menci et al. 2008), the triggering of such bright phases is thought to be related to galaxy mergers, in which cold gas is injected. The quasar mode efficiency must be proportional to the AGN fraction (i.e. the AGN luminosity function versus the galaxy luminosity function) and to how efficiently the AGN energy is released into the interstellar medium.

The second mode is related to the numerous, long-lived, low-luminosity AGN, that accrete hot gas coming from the halo's hot atmosphere continuously during cosmic time. This accretion happens at very low rates ($\sim 10^{-5} M_{\odot} \mathrm{yr}^{-1}$) in an inefficient regime, where the cooling of the central source is dominated by advective processes rather than radiation. The contribution of this accretion rate is too small to contribute significantly to the bolometric output of the AGN. However, these sources can still drive powerful, collimated outflows in the form of relativistic jets, which can perturb mechanically the surrounding gas (*radio mode* feedback; Croton et al. (2006); Bower et al. (2006)). This feedback action has been observed in several systems; by combining radio (synchrotron jet emission) and *Chandra* X-ray (hot, bremsstrahlung emitting intracluster medium) images, it has been observed that these jets are capable of excavate cavities in the intracluster gas on sub-galactic scales (McNamara et al., 2000). The radio mode efficiency depends on the total accreted mass (and then to the SMBH mass function).

Both these feedback modes are then capable to release energy directly in the environment from which the SMBH grows: the cooling, star-forming gas in the central region of the galaxy. This energy transfer not only reduces the rate at which the gas cools and form stars, but it also reduce the rate of accretion onto the SMBH. Feedback from AGN has been included in recent semianalytical models of galaxy evolution to switch off star formation in most massive galaxies, thus reproducing both the observed shape of the galaxy LF and the red, early type, passive evolving nature of the local massive galaxies. Quasar mode feedback is usually invoked to quench star formation at higher redshift, while radio mode feedback is assumed to suppress the cooling flows in massive galaxies at late times, thus maintaining the gas in a hot, tenuous state.

Chapter 3

The Black Hole mass of AGN

The aim of this Chapter is to provide a brief review on the current status of AGN black hole mass estimations and to discuss their main results and limits. For a more detailed discussion on this topic see the reviews of Shen (2013); Peterson (2010); Vestergaard et al. (2011) and references therein.

3.1 The Mass of the Black Holes hosted in AGN

Today is widely accepted that the high enery phenomena involved in the AGN activity have their origins in the accretion of matter onto a supermassive black hole (SMBH) at the center of the hosting galaxy. If SMBH grows mostly via this accretion process, its mass growth rate is given by:

$$\dot{M}_{BH} = \lambda_{Edd} L_{Edd} \frac{(1-\epsilon)}{\epsilon c^2} \tag{3.1}$$

where ϵ is the radiative efficiency (i.e. the fraction of accreted mass energy converted into radiation), $\lambda_{Edd} = L_{bol}/L_{Edd}$ is the Eddington ratio, L_{bol} is the bolometric luminosity of the AGN and L_{Edd}=$\lambda_{Edd} M_{BH}$ is the Eddington luminosity, defined as:

$$L_{Edd} = 1.26\ 10^{38} \left(\frac{M_{BH}}{M_{\odot}}\right) [ergs^{-1}]. \tag{3.2}$$

If λ_{Edd} and ϵ are non-evolving in time, thus the BH mass increases on a charecteristic time scale, named *Salpeter time*, t_e:

$$t_e \approx 4.5 \times 10^8 \frac{\epsilon}{\lambda_{Edd}(1-\epsilon)} yr \tag{3.3}$$

If quasars do not radiate beyond the Eddington limit ($L_{bol} = L_{Edd}$, thus λ_{Edd}=1), the observed luminosity provides a lower limit on their BH mass. The discovery of high luminosities quasars at redshift z>6 suggests that the more massive BH, with M_{BH} >10^9M$_\odot$, are the firsts to be formed, although they have had short time to evolve (*cosmic downsizing*).

In the past two decades it has come to the consensus that SMBHs are almost ubiquitous at the center of massive galaxies with significant bulge component, and also exist in some low-mass galaxies. More remarkably, tightly scaling relations between the mass of the nuclear BH and the galaxy bulge properties are found (e.g. bulge mass, luminosity and stellar dispersion-Ferrarese and Merritt 2000, Gebhardt et al. 2000, Marconi and Hunt 2003, Sani et al. 2011), suggesting that the evolution of galaxies and the growth of the super massive BHs (SMBH) are tied together (the AGN/galaxy co-evolution scenario).

In the framework of this scenario the energy released from the accreting BH self-regulates its own growth and impacts on the formation and evolution of the bulge through feedback processes (Silk and Rees 1998; Di Matteo et al. 2005). The Soltan argument (see Section 2.7) represents an elegant way to tie the local relic of SMBH population to the past active population, thus, if the SMBH grows mainly through a luminous (or obscured) quasar phase, the accreted luminosity density of quasars to z=0 should be equal to the local relic BH mass density (See Equations 2.21 and 2.22, Section 2.7), a reasonably good match between this two quantities can be achieved with an average radiative efficiency of ϵ ~0.1 (e.g. Yu and Tremaine 2002; Shankar et al. 2004; Marconi et al. 2004). The Soltan argument and its variants have been used in recent years to model the growth of SMBH.

As one of the few fundamental quantities describing a BH, the mass of AGN is of paramount importance to essentially all AGN-related science, such as the evolution and phenomenology of AGNs, the accretion physics itself and also the relations and interplays between SMBHs and their host galaxies through feedback processes. Thus it is fundamental to be aware of the current methodologies about the AGN BH mass estimations, their results but also theis limits and biases.

3.2 Methods for the BH mass estimation

3.2.1 Virial mass estimators: from reverberation mapping to single-epoch estimates

Reverberation mapping. As previously introduced in Section 2.4, the BLR is the AGN region where the broad emission lines are produced, powered by the UV continuum from the nucleous through photoionization processes. The emission line fluxes vary strongly in response to changes in the continuum caused by the ionizing source. The emission line variation shows with a time delay τ. Since the lag in the line response is proportional to the light travel time from the ionizing source to the BLR, it is possible to estimate the BLR size (R_{BLR}) by measuring this delay:

$$R_{BLR} = c \cdot \tau. \tag{3.4}$$

Moreover, by mapping the response function of the broad emission line to continuum variations it is possible in principle to reconstruct both the structure and the kinematics of the BLR.

This technique is known as *reverberation mapping* (RM) and has become a practical and powerful tool to study BLRs (see reviews by Peterson 1993; Netzer and Peterson 1997; Horne et al. 2004), whose spatial extent (sub-pc) is too small to be resolved by current instrumentation.

Under the assumpition that the motion of the emitting clouds is dominated by the gravitational field of the BH and that the BLR is virialized, the mass of the BH can be determinated by (e.g. Wandel et al. 1999):

$$M_{RM} = \frac{V_{vir}^2 R_{BLR}}{G} = f \frac{W^2 R_{BLR}}{G} \tag{3.5}$$

where V_{vir} is the virial velocity and W is the width of the broad emission lines. The latter can be used as an indicator of the virial velocity if it is assumed that the width of the lines of interest are Doppler broadened by the virial motion of the emitting gas. The quantity $W^2 R_{BLR}/G$ is also called *virial product.*

The broad lines width can be measured using the FWHM or the σ_{line}, both quantities are taken from *rms* spectra of the monitoring period, in order to have only the contribution of the variable part of the line to the width calculation.

The relation between the virial velocity and the line of sight (LOS) velocity inferred from W is determined by the structure and geometry of the BLR, which is not know. Thus, in virial methods is introduced a geometric factor f. This represent a great semplification since the line profile is affected by both the geometrical structure and the LOS, thus the line width W cannot fully describe the underlying kinematic. Similarly it is an approximation to describe the BLR with a single radius R since recent studies have shown evidences of a BLR stratification.
The value of f is empirically determined by requiring the derived RM masses to be consistent with those predicted using the BH mass - bulge stellar velocity dispertion scaling relation of local inactive galaxies (e.g. Onken et al. 2004, f ∼1.4 (5.5) for FWHM (σ_{line})). The determination of the f value remains one of the major uncertainties in RM mass estimations and show a typical scatter of ∼0.4−0.5 *dex*.

Luminosity-Radius relation. In the framework of reverberation mapping campaigns, the most remarkable finding is a tight correlation between the measured BLR size and the adjacent optical continuum luminosity (L_{opt}) at λ 5100 Å, $R_{BLR} \propto L_{opt}^{\alpha}$ (see Kaspi et al. 2000; Bentz et al. 2009). To first order L_{opt} is proportional to the luminosity of the ionizing continuum (L_{ion}) that is described by the ionization parameter in a photoionized medium (U):

$$U = \frac{Q(H)}{4\pi r^2 c n_e}, \tag{3.6}$$

where $Q(H)$ is the number of ionizing photons per second coming from the central source, c is the speed of light and n_e is the electron density. If both U and n_e are constant in the BLR, or if the BLR size is set by dust sublimation (Netzer and Laor, 1993), thus a slope of α=0.5 in the $R-L$ relation is expected. The latest version of the $R-L$ relation based on Hβ RM measurments is (Bentz et al., 2009):

$$\log \frac{R}{light\,days} = -2.13 + 0.519 \log \frac{\lambda L_\lambda(5100\mathring{A})}{ergs^{-1}}. \tag{3.7}$$

Single−epoch virial BH mass estimators. Starting from the $R-L$ relation it is possible to derive the BLR size through a single measure of the optical continuum luminosity and, combining this information with the width of a broad line, to build a relation for the BH mass estimate (M_{SE}):

$$\log\left(\frac{M_{SE}}{M_\odot}\right) = a + b\log\left(\frac{L}{10^{44} ergs^{-1}}\right) + c\log\left(\frac{W}{kms^{-1}}\right). \tag{3.8}$$

The latter has to be calibrated on the BH masses inferred from RM tecniques in order to derive the values for a, b coefficients, while $c = 2$ as expected for virial motion. Based on the general similarity of AGN SEDs, different luminosities have been used as an alternative to the L_{opt} in different versions of these SE virial estimators: X-ray and rest frame UV continuum luminosities, as well as line luminosities itself, (Vestergaard 2002; Greene and Ho 2005a; Vestergaard and Peterson 2006; Greene et al. 2010; Shen and Liu 2012). The uncertainty of the various single-epoch virial relations is estimated to be on the order of ∼0.5 *dex*. The virial RM and SE methods are currently considered the best way to estimate AGN BH masses.

3.2.2 Non virial methods

There are several other methods to estimate the BH masses of AGNs, although they are much less popular than the RM and SE. Nevertheless there are certain advantages in further developing these alternative methods in order to provide complementary mass estimates and consistency checks. In the following it will be briefly discussed some of these non virial estimators.

Photoionization method. Adopting the Woltjer's postulation that the BLR gas is in virial equilibrium in the gravitational potential of the central BH (Woltjer, 1959), an alternative way to derive the BLR size was first developed by Dibai (1977). The author makes use of the Equation 3.5 to estimates the BH mass, where the R_{BLR} is measured by using the photoionization argument:

$$L(H\beta) = \frac{4\pi}{3} R^3 j(n_e T_e)\epsilon_V, \tag{3.9}$$

where $L(H\beta)$ is the Hβ luminosity, $j(n_e T_e)$ is the volume emissivity in the Hβ line from photoionized gas and ϵ_V is the volume filling factor of BLR clouds. Thus, this method can be considered as a single-epoch estimator with an effective $R - L_{H\beta}$ relation with α=1/3. The BH masses derived using this method have an intrisic scatter of ∼0.3 *dex* with respect the RM estimates.

Accretion disk model fitting or SED fitting. Another way to infer the mass of the BH is by fitting the SED of quasars. The development of accretion disk theory over the last four decades (for a recent review, see Abramowicz and Fragile 2013) has enabled predictions of continuum luminosity, thus, by fitting the observed AGN continuum SED it is possible to constrain the model parameters (such as BH mass, accretion rate, BH spin, inclination) with adequate accretion disk models. Many studies have used this SED fitting method to derive AGN's BH masses (e.g. Calderone et al. 2012) assuming a standard thin accretion disk model (Shakura and Sunyaev, 1973), that successfully reproduce the observed ″Big Blue Bump″, but do not have the capability to explain the full AGN SED. The resulting BH mass constrain can be sensitive to deviations from standard accretion disk models. Moreover, due to the parameter degeneracies and model assumptions/simplifications in the SED fitting procedures, this method cannot provide an accuracy of better than a factor of ∼5 in BH mass estimates.

Direct dynamical BH masses. This is an observationally challenging method, since usually the AGN continuum diluites the stellar absorption features. Nevertheless there have been several attempts to get direct dynamical measurements of BH masses in Type 1 AGNs, using spatially resolved stellar kinematics (Onken et al., 2007) or gas kinematic (Hicks and Malkan, 2008) down to the sphere of influence of the black hole, $R_{SI} = GM_{BH}/\sigma^2$. Untill now, the number of AGNs with reliable dynamical BH mass measurements is still small.

Scaling relations. The well known correlations between BH mass and the bulge properties of the hosting galaxy are used to infer the BH mass in AGN. These scaling relations are calibrated with know BH mass derived usually by direct methods, such as RM campaigns, and they are usually applied also to non-broad line AGN (type 2). Nevertherless caution should be paid in appling this method, expecially on obscured AGNs, since recent studies have demonstrated that these scaling relations are unlikely to hold also for all AGN2 (see Graham 2008 and Kormendy et al. 2011).

3.3 Caveats, uncertainties, and biases of virial BH masses

3.3.1 The virial assumption

There are evidence supporting the virial assumption in RM in at least several AGNs. Here RM lags have been successfully measured for multiple lines with different ionization potentials and line widths (such as Hβ , C IV , He II) which, in the framework of a stratified BLR model, are supposed to arise at different distances from the BH. The measured lags and line widths fall close to the expected virial relation $W \propto R^{-0.5}$, although such a velocity radius relation does not necessarily rule out other BLR models where the dynamics is not dominated by the gravity of the central BH.

A possible way to test the virial assumption can be performed by monitoring if the variation of the line width in response to the continuum luminosity L can be described by the following Equation:

$$\Delta \log W = -0.25 \Delta \log L. \tag{3.10}$$

Indeed, if the source luminosity increases, the BLR is expected to expand due to the growth of radiation pressure. As a conseguence, the medium responsible of the production of the emission line gets away from the ionizing source thus producing a decrease of the corresponding line width.

Tests like this are very usefull to verify reliability of SE techniques. In effect, if the line width does not varies accordingly to luminosity changes, the infered SE BH mass values will be different for the same object, introducing a luminosity-dependent bias in the mass estimates. Fig. 3.1 (Shen, 2013) shows an example of this test, which is performed on a sample of AGN1 from the *Sloan Digital Sky Survey* (SDSS). The majority of this objects do not span a large dynamic range in luminosity and they cluster near the center. Only for the low luminosity Hβ sample the median relation is consistent with the virial relation (the solid lines in Figure 3.1). For the other samples, based on Mg II and C IV , the line width does not seem to respond to luminosity changes as expected from the virial relation. This difference could be a luminosity effect, but more detailed analyses are needed (Shen, 2013).

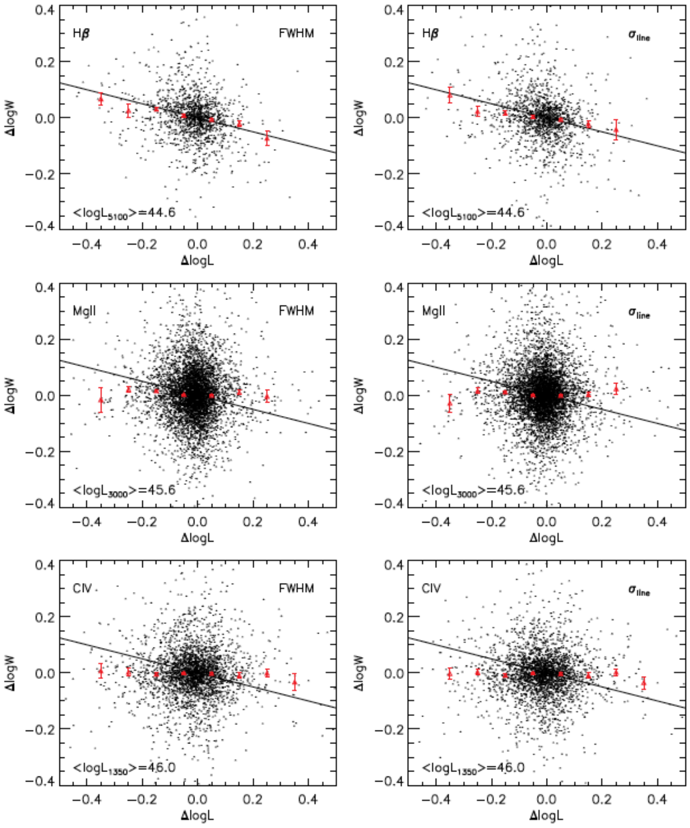

FIGURE 3.1. A test of the virial assumption using two-epoch spectroscopy from SDSS for Hβ (upper), Mg II (middle) and C IV (bottom). Plotted here are the changes in line width as a function of changes in continuum luminosity. The left column is for the FWHM, while the right column is for the σ_{line}. The red triangles are the median values in each $\Delta \log L$ bin (Shen, 2013).

As seen in Section 3.2.1 to relate the observed broad line width to the underlying virial velocity it is necessary to make some assumptions on the geometry and kinematics of the BLR, introducing in Equation 3.5 the geometric factor f. In principle the RM tecniques can provide such information, and determine the value of f. Unfortunately the current RM data are still not good enough for such purposes. Early studies made assumptions about the geometry and structure of the BLR in deriving RM masses (e.g. Kaspi et al. 2000) or SE virial masses. Actually the average value of f is mostly determined empirically by requiring that the RM masses are consistent with those predicted from the $M_{BH} - \sigma_\star$ relation of local inactive galaxies ($f \sim$1.4 if FWHM is used, Onken et al. 2004; $f \sim 5.2$ using σ_{line}, Woo et al. 2010). The use of the scaling relation involve other problems, indeed there is growing evidences that different galaxies follow different scaling relations, thus the results can change depending on the correlation used. Moreover, the use of the average value of the geometric factor $< f >$ causes the overstimation or underestimation of the BH masses of the single objects, due to orientation effects.

3.3.2 Limitations on virial estimators

In the rest-frame UV to near infrared AGN continuum there are several emission lines and, despite their different ionization potentials and probably different BLR structures, many of them have been used in SE mass estimates. The most used are the Balmer lines, expecially Hα and Hβ , but also Lyman and Paschen lines are used. Some other lines, such as Mg II and the high ionized C IV ,are also involved in these methods but, several tests in which the different line widths are compared, have shown that SE mass estimators based on Hydrogen lines are the most reliable ones (see Shen 2013 for a more detailed decription).

Another element to be taken into account is the adopted luminosity in the L-R relation. As introduced in Section 3.2.1 several SE estimator using continuum luminosities from different bands (i.e. UV, IR or X-ray) have been calibrated. Indeed the luminosity that enters the R−L relations and the SE estimators refers to the AGN continuum, thus the contamination from host starlight in the optical band can be significant, in particular for low luminosity sources. This motivated the alternative uses of Balmer line luminosities, usually preferred for radio-laud AGN where the continuum may be severely contaminated by the nonthermal emission from the jet (Bentz et al., 2009). For UV luminosities (L_{3000}, L_{1350} or L_{1450}) the host contamination is usually negligible, but it could be serious problems from dust reddening which can significantly attenuate AGN UV luminosity.

Regardless of the choice of the specific SE estimator, a concern is that the AGN variability, which spans a wide range of time scales, may affected the SE BH masses. However, as several studies have shown by using multi-epoch spectra of AGN samples, the changes in luminosity do not introduce significant scatter ($>$0.1 *dex*) to the SE mass estimates (Denney et al. 2009; Park et al. 2012).

Last but not least, the current sample with RM BH mass estimates is not representative of the general AGN population. In effect this estimator can be used only for local sources (z<0.3) and it poorly samples the high-luminosity regime of AGN. These limitations affects reliability of extrapolations of locally calibrated SE relations to high z and high luminosity quasars. Moreover the total number of RM AGNs is also small (∼50), thus are not enough to probe the diversity in BLR structure and other general quasar properties. The current sample size and inhomogeneity of RM AGNs represents another obstacle in the development of accurate BH mass estimators based on virial methods.

3.3.3 Practical concerns

Usually the continuum and line properties are measured either directly from the spectrum, or derived from χ^2 fits to the spectrum, in which some functional forms for the continuum and for the lines are applied. It is essential to measure these quantities in a properly way, especially when using SE calibrations, because different methods sometimes can yield to systematically different results, in particular for the line width measurements. Indeed single-component and multi-component line fits could differ significantly in some cases.

A detailed description of spectral fitting procedures can be found in some papers (e.g. Greene and Ho 2005b; Shen and Liu 2012). Basically the spectrum is first fit with a power-law in order to decribe the continuum, and later an Iron emission template is added. The broad line region is then fit with multiple Gaussians. Moreover there are some additional precautions that have to be taken into account:

- **Narrrow line subtraction**: The NLR dynamics are not dominated by the gravitational influence of the BH, thus in the velocity estimation of the BLR gas the narrow line component has to be removed before measuring the broad line width from the spectrum.

- **Remedy for absorption**: Sometimes there are absorption features superposed on the spectrum and not accounting for these absorption features will bias the continuum and line measurements.

- **Effects of low S/N**: The quality of the continuum luminosity and line width measurements decreases as the quality of the spectrum degrades.

3.4 Application to statistical samples

Despite the many caveats of SE mass estimators discussed above, they have been extensively used in recent years to measure BH mass function (SMBHMF), the Eddington ratio function (BHERF), the luminosity function (LF) and the scaling relations between BH and the hosting galaxy bulge properties. It is important to recognize, however, that the uncertainty in these mass estimates has influences on the interpretation of these measurements.

3.4.1 Demographics in the mass-luminosity plane

The AGN distribution in the two dimensional BH mass-luminosity ($M_{BH} - L$) plane involve important information on the accretion process of the active SMBHs. In Figure 3.4.1 the observed $M - L$ plane (i.e. the one obtained from SE BH mass estimates) from an SDSS AGN sample is compared with the simulated one at $z = 0.6$. In the left panel of Figure 3.4.1 is shown the observed distribution for a sample of quasar whose masses has been derived using virial methods in the redshift range $0.7 < z < 7$. In these cases several emission lines have been used, such as Hβ , Mg ii and C iv . The observed distribution suffers from the flux limit effect, indeed low Eddington ratio objects have a lower probability to be selected into the sample.

The best way to overcome this issue is to use a modeling approach in which an underlying distribution of simulated masses and luminosities is specified and mapped to the observed mass-luminosity plane by imposing the flux limit of the survey (see Kelly et al. 2009 and Kelly et al. 2010). The comparisons between model and observed distributions constrain the model parameters.

Shen and Kelly 2012 used forward modeling with Bayesian inference to model the observed distribution in the mass luminosity plane of SDSS quasars, taking into account a possible luminosity dependent bias to be constrained by the data. In Figure 3.4.1, right panel is shown the comparison between the simulated $M - L$ distribution (red contours) and the mesured one based on Hβ SE virial masses (black contours). The distribution based on SE virial BH masses is flatter than the one based on true masses due to the scatter and to the luminosity dependent bias of these SE masses. Moreover the flux limited survey selects only the most luminous objects into the SDSS sample, missing the bulk of low Eddington ratio objects.

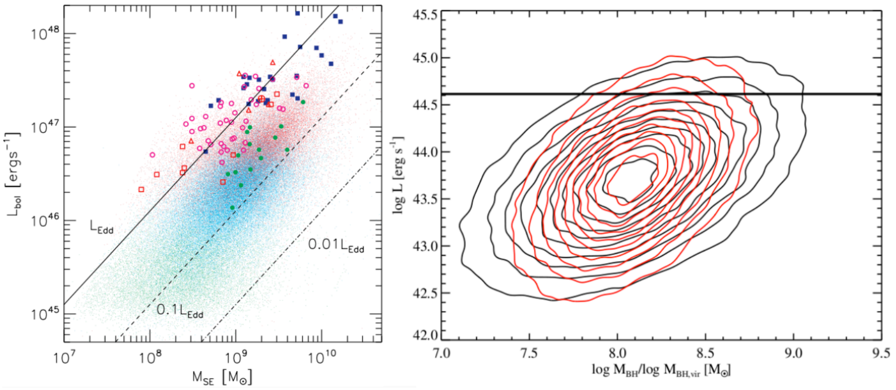

Figure 3.2. Left: $M - L$ plane for a sample of quasars with virial BH mass estimates. The green dots refer to SE BH mass estimates using Hβ ($z < 0.7$), the cyan dots are for Mg ii line ($0.7 < z < 1.9$) and red dots for C iv ($z > 1.9$). Different symbols refer to different quasar samples. Solid line represent the Eddington limit, while the dashed lines shows the places of sub-Eddington regions. Right: Simulated $M - L$ plane of an AGN population at $z = 0.6$, the red contours are the "true″ distribution of quasars and is determined by the model BHMF and Eddington ratio distribution in Shen and Kelly (2012). The black contours are the measured distribution based on Hβ SE virial masses. The flux limit of the SDSS sample is shown with the solin black line. For more detail about the two planes see Shen (2013) review.

The $M - L$ plane can be also used to measure the abundance of AGN and to study their redshift evolution. This is a much more powerful way to study the cosmic evolution of quasars than traditional 1D distribution functions such as the luminosity function (LF) and the quasar BHMF, since the latters are its monodimensional projections. Figure 3.4.1, taken from Shen (2013), shows the simulated quasar $M - L$ plane at $z = 0.6$ constrained using SDSS sources. The objects abundance is shown with the colour-code contours and the traditional LF and BHMF are represented in the rigth panel. The 1D distribution functions lose information by collapsing on one dimension, and a better way to study the demography of quasars is to measure their abundance in 2D, since the mass and luminosity of a quasar are physically connected by the Eddington ratio.

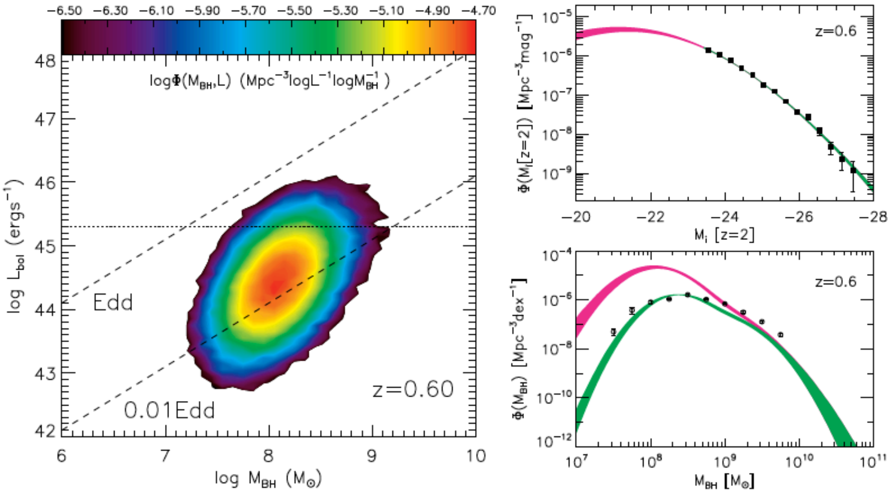

FIGURE 3.3. Left: Quasar simulated $M - L$ distribution at $z = 0.6$ with the source density shown with the colour code contours. Right: LF (up) and BHMF (bottom). The two projections shows the “true″ population of broad line AGN (magenta) and the observed, flux limited one (green) (Shen, 2013).

.

Chapter 4

The project and the observations

4.1 The AGN2 SWIFT/BAT sample

4.1.1 The idea

In recent works, Landt et al. (2008, 2011, 2013) have performed NIR observations of AGN1 whose BH masses were measured with reverberation mapping techniques, and they have demonstrated that the virial method can be efficently used also with the Paα and Paβ lines. These authors developed a NIR virial relationship to estimate the AGN BH masses based on the width of the Paschen hydrogen broad emission lines and the total 1 μm continuum luminosity. However, the latter has to be derived by a SED fitting method and can suffer from galaxy contamination, especially for intrinsic low-luminosity AGNs, such as the obscured ones.

Since several studies have shown that most AGN2 exhibit faint components of broad lines if observed with high S/N in the near infrared, where the dust absorption is less severe than in the optical (Veilleux et al. 1997; Riffel et al. 2006; Cai et al. 2010), we decided to calibrate a new NIR virial relation able to work also with obscured AGN. Thus, in order to overcome the galaxy contamination and the dust obscuration problems, we choose to use the hard X-ray luminosity in the 14-195 keV as a measure of the BLR radius and the FWHM of NIR hydrogen emission lines for the gas velocity estimation. Such a NIR virial relation could then be used to derive, for the very first time, a direct measurment of the AGN2 BH masses.

4.1.2 The sample

The *Swift* Gamma-ray burst observatory was launched in November 2004, and has been continually observing the hard X-ray sky in the 14-195 keV band with the Burst Alert Telescope (BAT), a large coded-mask telescope optimized to detect transient GRBs. Its characteristics, such as the wild field of view (FOV), the broad sky coverage and the improved sensitivity with respect to the previous surveys, make the *Swift*/BAT 70 month one of the most uniform and complete hard X-ray survey. Since its beginning the *Swift*/BAT 70 month has detected 1171 hard X-ray sources in the 14-195 keV band down to a significance level of 4.8 σ and among these ∼600 are Seyfert galaxies. In Figure 4.1 is shown an all sky map of the *Swift* sources distribution (Baumgartner et al., 2013).

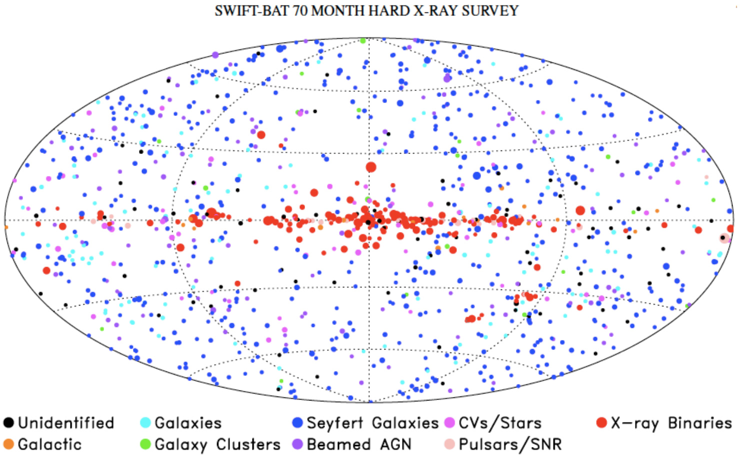

FIGURE 4.1. All-sky map showing classification of the BAT 70 month survey sources. The flux of the source is proportional to the size of the circle. The source type is encoded by the color of the circle (Baumgartner et al., 2013).

Among the 1171 sources in the *Swift*/BAT 70 month catalogh, the 80% have solid counterpart associations that have been verified with X-ray observations, although 100% of the BAT sources have archival X-ray data. More than the 60% of the associations are with extragalactic objets. The median 5σ sensitivity achieved in the 70 month survey is 0.43 mCrab, that is equivalent to $\sim 10^{11}$ erg s^{-1} cm^{-2} in the 14-195 keV band. These characteristics make it the deepest uniform hard X-ray survey ever conducted (Baumgartner et al., 2013), and with the detection of over 600 AGN in the hard X-ray band, the Swift-BAT 70 month catalog contains a valuable reference set of active galaxies in the local universe.

In order to have a complete sample of obscured and intermediate AGN (AGN2, AGN1.9 and AGN1.8) with hard X-ray luminosity determination, we randomly selected 41 sources from the ∼600 Seyfert galaxies indentified in the *Swift*/BAT 70 month hard X-ray survey. We observed all these sources with NIR spectrographs both in the south and in the north emispheres. In the southern emisphere, we obtained observing time at the VLT with the near infrared spectrograph ISAAC and with the multiwavelenght, medium resolution spectrograph Xshooter. Our observations in the nothern emisphere were conducted at the LBT using the LUCI facility. In Table 4.1 we report the principal characteristics of the selected sources. In Figure 4.2 we show the hard X-ray luminosity distribution of the *Swift*/BAT AGN1 (in black), *Swift*/BAT AGN2 (in red) together with our subsample of 41 AGN2.

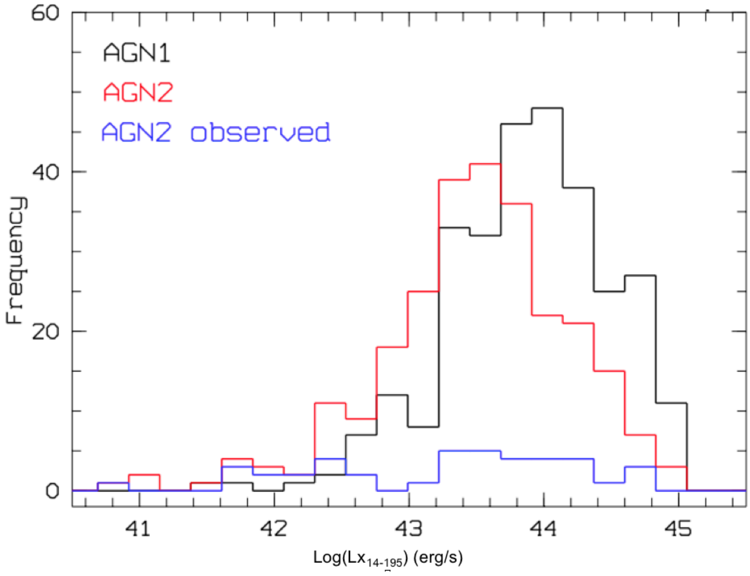

FIGURE 4.2. Hard X-ray luminosity distribution for *Swift*/BAT AGNs: the black histogram shows the AGN1 distribution, the red one is referred to AGN2, while in blue is our subsample of AGN2 randomly selected from *Swift*/BAT 70 Month.

In the following sections we will describe the three spectrographs used for the acquisition of the NIR data and the observational setup.

Obderved AGN randomly selected from SWIFT 70 month catalog

Object name (1)	α [hh : mm : ss.s] (2)	δ [°:′:″] (3)	**z** (4)	$\mathbf{logL_X}$ [erg/s] (5)	$\mathbf{logN_H}$ [$\mathbf{cm^{-2}}$] (6)	**cl** (7)	**obs. date** (8)	**instrument** (9)
2MSXJ05+32	06:41:18.0	+32:49:32	0.0470	44.26	-	2	20/10/2012	LUCI
2MSXJ09+45	09:11:30.0	+45:28:06	0.0268	43.42	23.42 (T08)	2	20/10/2012	LUCI
2MSXJ11+19	11:27:16.3	+19:09:20	0.1059	44.65	-	1.8	06/12/2012	LUCI
3C403	19:52:15.8	+02:30:24	0.059	44.46	23.60 (T08)	2	25/10/2012	LUCI
Mrk 417	10:49:30.9	+22:57:52	0.0327	43.90	$24.08^{+0.02}_{-0.02}$	2	05/12/2012	LUCI
NGC3079	10:01:57.8	+55:40:47	0.00372	42.00	-	2	23/10/2012	LUCI
NGC4138	12:09:29.8	+43:41:07	0.0029	41.76	$23.12^{+0.02}_{-0.02}$	1.9	06/12/2012	LUCI
NGC4388	12:25:46.7	+12:39:44	0.0084	43.64	$23.81^{+0.02}_{-0.02}$	2	19/02/2013	LUCI
NGC4395	12:25:48.8	+33:32:49	0.0013	40.79	$23.01^{+0.02}_{-0.02}$	1.9[a]	05/12/2012	LUCI
NGC4686	12:46:39.9	+54:32:03	0.0167	43.24	$23.89^{+0.03}_{-0.03}$	Glx/XBONG	07/12/2012	LUCI
2MASX J05-23	05:05:46.5	-23:51:22	0.0350	44.24	-	2	03/11/2011	ISAAC
3C105	04:07:16.4	+03:42:26	0.089	44.74	23.43 (T08)	2	07/10/2011	ISAAC
CGCG 420-15	04:53:25.7	+04:03:42	0.0294	43.75	-	2	19/12/2011	ISAAC
ESO-005-G004	06:05:44.0	-86:37:57	0.0062	42.46	23.88 (T08)	2	04/11/2011	ISAAC
ESO-157-G023	04:22:24.2	-56:13:33	0.0435	43.97	-	2	09/10/2011	ISAAC
ESO-297-018	01:38:39.3	-40:00:40	0.0252	44.0	23.84 (T08)	2	13/10/2011	ISAAC
ESO -374-G44	10:13:20.4	-35:59:07	0.0284	43.57	-	2	22/01/2012	ISAAC
ESO 416-G002	02:35:14.1	-29:36:26	0.0592	44.29	<19.60 (T08)	1.9	08/10/2011	ISAAC

Continued on next page

---

[a] Sy1 from literature

Obderved AGN randomly selected from SWIFT 70 month catalog

Object name (1)	α [hh : mm : ss.s] (2)	δ [°:′:″] (3)	**z** (4)	**logL$_X$** [erg/s] (5)	**logN$_H$** [cm^{-2}] (6)	**cl** (7)	**obs. date** (8)	**instrument** (9)
ESO-417-G006	02:56:21.6	-32:11:26	0.0163	43.26	-	2	11/10/2011	ISAAC
Fairall 272	08:23:01.1	-04:56:05	0.0218	43.70	-	2	22/12/2011	ISAAC
LEDA 093974	10:40:22.3	-46:25:26	0.0239	43.35	22.96 (T08)	2	08/01/2012	ISAAC
MCG-01-24-12	09:20:46.2	-08:03:22	0.0196	43.55	22.80 (T08)	2	07/01/2012	ISAAC
MCG-05-23-16	09:47:40.3	-30:57:10	0.0085	43.51	22.47 (T08)	2	01/01/2012	ISAAC
Mrk 1210	08:04:06.2	+05:06:31	0.0135	43.35	-	2	19/12/2011	ISAAC
NGC 612	01:33:59.3	-36:29:41	0.0298	44.05	23.70 (T08)	2	13/10/2011	ISAAC
NGC 788	02:01:06.4	-06:48:57	0.00136	43.52	23.48 (T08)	2	07/10/2011	ISAAC
NGC 1052	02:41:04.8	-08:15:21	0.005	42.22	-	2	04/11/2011	ISAAC
NGC 1142	02:55:12.3	-00:11:02	0.0289	44.23	23.38 (T08)	2	09/10/2011	ISAAC
NGC1365	03:33:38.0	-36:08:31	0.0055	42.63	23.60 (T08)	1.8	13/10/2011	ISAAC
NGC 2992	09:45:42.1	-14:19:35	0.0077	42.55	22.00 (T08)	2	07/10/2012	ISAAC
NGC 3081	09:59:29.1	-22:49:23	0.0080	43.07	23.52 (T08)	2	06/01/2012	ISAAC
NGC 3281	10:31:52.1	-34:51:13	0.0107	43.34	24.30 (T08)	2	14/11/2011	ISAAC
PKS-0326-288	03:28:36.8	-28:41:57	0.108	44.60	- (T08)	1.9	07/10/2011	ISAAC
ESO-263-G13	10:09:48.2	-42:48:40	0.0333	43.96	-	2	11/02/2013	XSHOOTER
LEDA 093974	10:40:22.3	-46:25:26	0.0239	43.35	22.96 (T08)	2	11/02/2013	XSHOOTER
MCG-05-23-16	09:47:40.3	-30:57:10	0.0085	43.51	22.47 (T08)	2	11/02/2013	XSHOOTER
2MASXJ18+09			0.0190	42.40	-	2	05/06/2014	XSHOOTER/P93
ESO-234-G50	20:35:57.8	-50:11:32	0.0088	42.29	-	2	25/06/2014	XSHOOTER/P93

Continued on next page

Obderved AGN randomly selected from SWIFT 70 month catalog

Object name	α [hh : mm : ss.s]	δ [°:′:″]	**z**	**logL$_X$** [erg/s]	**logN$_H$** [cm^{-2}]	**cl**	**obs. date**	**instrument**
(1)	**(2)**	**(3)**	**(4)**	**(5)**	**(6)**	**(7)**	**(8)**	**(9)**
NGC 3783	11:39:01.7	-37:44:18	0.0097	43.58	22.47 (T08)	1	11/02/2013	XSHOOTER/P93
NGC 4941	13:04:13.1	-05:33:06	0.0037	41.79	$24.12^{+0.12}_{-0.17}$(V12)	2	21/07/2014	XSHOOTER/P93
NGC 4945	13:05:27.3	-49:28:04	0.0019	42.35	24.60 (T08)	2	23/4/2014	XSHOOTER/P93
NGC 5643	14:32:40.8	-44:10:29	0.0040	41.80	-	2	20/06/2014	XSHOOTER/P93
NGC 6221[b]	16:52:46.3	-59:13:01	0.0050	42.17	-	2	24/4/2014	XSHOOTER/P93
NGC 7314	22:35:46.2	-26:03:01	0.0048	42.42	21.79 (T08)	1.9	25/06/2014	XSHOOTER/P93
NGC7465[c]	23:02:00.9	+15:57:54	0.0066	42.14	23.66	LINER/Sy2	05/07/2005	LIRIS/WHT

TABLE 4.1. Our AGN2 sample randomly selected from the *Swift*/BAT 70-month survey (Baumgartner et al., 2013). (1) Source name; (2) and (3) source coordinates; (4) Redshift; (5) X-ray luminosity in the 14-195 keV band; (6) Intrinsic column density (T08=Tueller et al. 2008; V12=Vasudevan et al. 2013); (7) AGN classification; (8) Date of observation; (9) Instrument used.

Continued on next page

---

[b] Lx is obtained from L20-100 keV from INTEGRAL data from Beckmann et al. (2009)

[c] Ramos Almeida et al. (2009)

4.2 LUCI/LBT Observations

LUCI (LBT NIR Spectrograph Utility with Camera and Integral-Field Unit for Extragalactic Research) is a NIR spectrograph and imager at the Large Binocular Telescope (LBT) working in the wavelength range from 0.85 μm to 2.5 μm, corresponding to the photometric z, J, H and K bands. It is mounted on the bent Gregorian focus of the SX mirror of the telescope at LBT observatory (LBTO) in Arizona. The instrument observing modes available are:

- seeing-limited imaging over a $4'$ field of view (FOV) with the N 3.75 camera (image scale $0.12''$/px);
- seeing-limited spectroscopy, using the N 1.8 camera (image scale $0.25''$/px).

Spectroscopic observations can be carried out with a resolution of up to 8500 (seeing limited). The instruments are equipped with Rockwell HAWAII-2 HdCdTe 2048×2048 px^2 array. However, the observing range is limited on the blue side by the cut-off wavelength of the entrance window at λ=0.87 μm and on the red side by the cut-off of the atmospheric window after λ=2.4 μm.
We observed at the Large Binocular Telescope (LBT), using the LUCI facilities, a total of 10 sources from our Swift/BAT AGN sample. The observations have been performed between October 2012 and February 2013 and all the objects have been acquired in the zJ (0.92−1.5 μm) band using the grating 200 H+K in combination with the zJspec filter, but one of them has been observed also in the K (2.025−2.353 μm) band using the 210 zJHK grating. We used a 1"×2.8' slit corresponding to a Δv=220 km s^{-1} and Δv=87 km s^{-1} spectral resolution for J and K band, respectively. The characteristics of the 200 H+K grating, used for the zJ band observations, are the following:

- *wavelenght range*: 1.38−2.4 μm;
- *grating dispersion*: 2.16 Å/px
- *resolution*: R=1360 for the $1''$ slit width at λ_c=11750 Å, corresponding at a velocity resolution of Δv=220 km s^{-1} .

For the zJHK 210 lines/mm grating, used in the K band, the characteristics are the following:

- *wavelenght range*: 2.02−3.18 μm;
- *grating dispersion*: 1.60 Å/px
- *resolution*: R=3437 for the 1″ slit width at λ_c=22000 Å, corresponding at a velocity resolution of Δv=87 km s^{-1} .

The images acquisition have been performed using the CCD HdCdTe HAWAII-2 camera, with the following characteristics:

- *field of view*: 4′×4′ in seeing limited imaging;
- *array*: 2048×2048 px^2;
- *scale*: The camera N3.75 (for imaging) has a scale of 0.125"/px, while the camera N1.8 for spectroscopy has a scale of 0.25″/px;
- *readout noise (RON)*: $<5e^- = 1.27$ ADU in lecture mode MER (Multiple-Endpoint Read);
- *gain*: 3.93e^-/ADU;
- *linearity*: <2 10^5 ADU.

All the observations have been carried out by rotating the slit in order to observe also a bright star, the telluric star, that was later used to correct for OH absorptions, which are known to vary across the night. We acquired 8 images with exposures of 350 s for each sources, using the nodding technique, in order to perform a better sky correction during the data reduction phase. We also have observed a bright standard star (O-B or Solar spectral type) for each sources, in order to use it for the flux calibration step, if the telluric star was not availabe. Flats and arcs were taken within one day from the observations. The observational features for each source are reported in Table 4.2.

4.3 ISAAC/VLT Observations

ISAAC is an IR (1−5 μm) imager and spectrograph, that was mounted at the Nasmyth A focus of the UT3 of the Very Large Telescope in Chile till the 12th

LBT observing log
$1'' \times 2.8'$ slit width
velocity resolution of Δv=220 km s^{-1} for zJ, Δv=87 km s^{-1} for K.

object name **(1)**	**date** **(2)**	**UT** **[hh:mm]** **(3)**	**exposure** **[s]** **(4)**	**seeing** **[$''$]** **(5)**	**airmass** **(6)**	FIlter **(7)**	Grating **(8)**
2MASX J0641+3249	2012 Oct 20	08:15	8×350	1.47	1.52	zJspec	200 H+K
2MASX J0911+4528	2012 Oct 20	10:57	8×350	0.75	1.39	zJspec	200 H+K
2MASX J0911+4528	2012 Oct 20	10:57	6×350	0.71	1.12	zJspec	200 H+K
NGC 3079	2012 Oct 23	12:43	5×350	1.21	1.22	zJspec	200 H+K
NGC 3079	2012 Oct 24	12:24	8×350	1.08	1.26	zJspec	200 H+K
3C 403	2012 Oct 25	02:14	2×350	1.33	1.21	zJspec	200 H+K
Mrk 417	2012 Dec 05	10:03	8×350	0.73	1.38	zJspec	200 H+K
NGC 4395	2012 Dec 05	12:09	8×350	0.54	1.21	zJspec	200 H+K
NGC 4138	2012 Dec 06	10.55	8×350	0.54	1.37	zJspec	200 H+K
2MASX J1127+1909	2012 Dec 06	11:06	8×350	0.53	1.10	zJspec	200 H+K
2MASX J1127+1909	2012 Dec 06	13:08	8×350	0.53	1.04	K	210zJHK
NGC 4686	2012 Dec 07	11:16	8×350	1.05	1.42	zJspec	200 H+K
NGC 4388	2013 Feb 19	09:36	8×350	0.74	1.07	zJspec	200 H+K

TABLE 4.2. LUCI/LBT observation log for the 10 sources observed. (1) Source name; (2) Date of observation; (3) Starting time of acquisition; (4) Number of acquisitions and exposure time for each acquisition; (5) seeing; (6) airmass; (7) Filter used during the observations; (8) Grating used during the observations. We used a $1'' \times 2.8'$ slit width, corresponding in a velocity resolution of Δv=220 km s^{-1} and Δv=87 km s^{-1} for zJ and K observations, respectively.

December 2013. It has two arms, one equipped with the 1024×1024 Hawaii Rockwell array, used for short wavelenght (SW; 1−1.5 μm), and the other with a 1024×1024, used for long wavelenghts (LW; 3−5 μm). The instrument has several observing modes available: imaging and spectroscopy in both short wavelength (SW) and long wavelength (LW), FastPhot (Burst and FastJitter) imaging in LW only, and imaging polarimetry in SW only. All modes are offered for both Service and Visitor Programs. In spectroscopic modes ISAAC is equipped with two gratings, for Low and Medium resolutions (LR and MR, respectively) spectroscopy, six slits with widths ranging from 0.3 to 2 arcsec, and order sorting filters for each spectroscopic band. A calibration unit allows calibration lamps to be used for both wavelength calibration and flat fielding (in spectroscopy only). The lamps used for wavelength calibration are Xenon and Argon.

We observed at VLT, using the ISAAC spectrograph, a total of 25 sources from our *Swift*/BAT AGN sample. All the observations have been performed between October 2011 and January 2012 in the SW mode, equipped with the 1024×1024 Hawaii Rockwell array arm. All the ojects have been observed in the J band, but two sources with z∼0.1 have been observed also in the K band. In all cases we used both LR and MR instument modes and a 0.8″ ×120″ wide slit, corresponding to a spectral resolution of ∼ 430 km s^{-1} and ∼ 60 km s^{-1} for LR and MR mode, respectively. The characteristics of the SW/LR and SW/LR grating are:

- *wavelenght range*: 1.1−1.4 μm for J filter; 1.82−2.5 μm fot SK filter;
- *pixel scale*: 0.147 ″/px
- *resolution* LR: R=730 at λ_c=1.25μm (J filter); R=600 at λ_c=2.16 μm (SK filter), for the 0.8″×120″ slit width.
- *resolution* MR[d]: R=4700 at λ_c=1.25μm (J filter); R=3900 at λ_c=2.16 μm (SK filter), for the 0.8″×120″ slit width.

The images acquisition have been performed using the Hawaii detector with the following characteristics:

- *Spectral range*: 0.98−2.5 μm;

---

[d] In MR mode λ_c varies slightly in order to center the NIR lines in the spectra.

- *Field of view*: 152″×152″;
- *Array*: 1024×1024 px^2;
- *Scale*: 0.1484″/px;
- *Pixel size*: 18.5 μm;
- *Readout noise (RON)*: ∼10 e$^-$;
- *gain*: 4.6 e$^-$/ADU.

The observations were performed in order to center the galaxy's nucleus at the best and, when possible, the slit has been rotated in order to include also a telluric star. We acquired 6 LR frames with exposures of 180 s and 4 MR with exposures of 340 s for each sources, using the nodding technique to remove the sky contribution to the spectra. We also observed a bright standard star within 30 minutes to the target observations, and use it to both calibrate the absolute flux and correct for OH absorptions every time the telluric star was not available. As usual, flats and arcs were taken within one day from the observations. The main datails of all the ISAAC observations are shown in Table 4.3.

ISAAC observing log
0.8″ ×120″ slit width
velocity resolution of Δv ∼430 km s^{-1} for LR, Δv ∼60 km s^{-1} for MR.

object name (1)	**Obs. date** (2)	**Obs. time (UT)** [hh:mm] (3)	**exposure** [s] (4)	**seeing** [″] (5)	**airmass** (6)	**Filter** (7)	**Grating/λ_c** mode /[μm] (8)
PKS 0326-288	07 Oct 2011	04:41	6×180	1.22	1.192	SK	LR/2.2
PKS 0326-288	07 Oct 2011	04:15	4×340	1.22	1.239	SK	MR/2.078
3C 105	07 Oct 2011	05:13	6×180	0.90	1.406	SK	LR/2.2
3C 105	07 Oct 2011	05:00	4×340	0.89	1.263	SK	MR/2.042
PKS 0326-288	07 Oct 2011	03:01	6×180	0.88	1.549	J	LR/1.25
PKS 0326-288	07 Oct 2011	02:45	4×340	0.99	1.551	J	MR/1.2
NGC 788	07 Oct 2011	02:09	6×180	1.06	1.685	J	LR/1.25
NGC 788	07 Oct 2011	01:43	4×340	0.93	1.977	J	MR/1.299
ESO 416-G002	08 Oct 2011	02:37	6×180	1.05	1.481	J	LR/1.25
ESO 416-G002	08 Oct 2011	02:59	4×340	0.94	1.360	J	MR/1.147
NGC 1142	09 Oct 2011	04:53	6×180	0.90	1.197	J	LR/1.25
NGC 1142	09 Oct 2011	05:16	4×340	0.90	1.154	J	MR/1.319
ESO 417-G006	11 Oct 2011	06:37	6×180	1.00	1.011	J	LR/1.25
ESO 417-G006	11 Oct 2011	06:11	4×340	0.88	1.009	J	MR/1.303
NGC 612	13 Oct 2011	02:43	6×180	1.12	1.150	J	LR/1.25

Continued on next page

ISAAC observing log

0.8″ ×120″ slit width

velocity resolution of Δv ∼430 km s^{-1} for LR, Δv ∼60 km s^{-1} for MR.

object name (1)	**Obs. date** (2)	**Obs. time (UT)** [hh:mm] (3)	**exposure** [s] (4)	**seeing** [″] (5)	**airmass** (6)	**Filter** (7)	**Grating/λ_c** mode /[μm] (8)
NGC 612	13 Oct 2011	03:26	4×340	0.98	1.076	J	MR/1.320
NGC 1365	13 Oct 2011	05:56	6×180	0.87	1.028	J	LR/1.25
NGC 1365	13 Oct 2011	06:32	4×340	0.92	1.023	J	MR/1.289
ESO -297-018	13 Oct 2011	04:34	6×180	1.22	1.040	J	LR/1.25
ESO -297-018	06 Oct 2011	05:17	4×340	1.09	1.037	J	MR/1.314
ESO -157-G023	19 Oct 2011	07:41	6×180	1.03	1.173	J	LR/1.25
ESO -157-G023	19 Oct 2011	07:23	4×340	1.09	1.179	J	MR/1.338
3C 105	21 Oct 2011	07:22	6×180	0.76	1.146	J	LR/1.25
3C 105	21 Oct 2011	07:06	4×340	0.90	1.170	J	MR/1.179
2MASX J0505-2351	03 Nov 2011	03:41	6×180	0.90	1.412	J	LR/1.25
2MASX J0505-2351	03 Nov 2011	04:05	4×340	0.77	1.294	J	MR/1.327
ESO 005- G 004	04 Nov 2011	03:04	6×180	1.36	2.300	J	LR/1.25
ESO 005- G 004	04 Nov 2011	03:25	4×340	1.23	2.276	J	MR/1.290
NGC 1052	04 Nov 2011	01:14	6×180	0.90	1.540	J	LR/1.25
NGC 1052	04 Nov 2011	01:39	4×340	1.04	1.390	J	MR/1.288
NGC 3281	14 Nov 2011	07:26	6×180	1.09	1.641	J	LR/1.25
NGC 3281	14 Nov 2011	08:17	4×340	1.08	1.414	J	MR/1.296
Mrk 1210	19 Dec 2011	07:56	6×180	0.69	1.241	J	LR/1.25
Mrk 1210	19 Dec 2011	07:25	4×340	0.77	1.193	J	MR/1.299
CGCG -420-015	19 Dec 2011	06:04	6×180	0.71	1.451	J	LR/1.25
CGCG -420-015	19 Dec 2011	04:49	4×340	0.78	1.593	J	MR/1.32
Fairall 272	22 Dec 2011	04:49	6× 180	0.96	1.264	J	LR/1.25
Fairall 272	22 Dec 2011	05:31	4× 340	0.89	1.134	J	MR/1.31
MCG -05-23-016	01 Jan 2012	04:39	6×180	0.82	1.288	J	LR/1.25
MCG -05-23-016	01 Jan 2012	04:12	4×340	0.81	1.205	J	MR/1.293
NGC 3081	06 Jan 2012	03:55	6×180	1.16	1.592	J	LR/1.25
NGC 3081	06 Jan 2012	04:19	4×340	0.82	1.433	J	MR/1.292
MGC -01-24-012	07 Jan 2012	03:06	6×180	1.19	1.665	J	LR/1.25
MGC -01-24-012	07 Jan 2012	02:27	4×340	1.39	1.539	J	MR/1.307
NGC 2992	07 Jan 2012	04:32	6×180	1.14	1.275	J	LR/1.25
NGC 2992	07 Jan 2012	05:09	4×340	1.10	1.192	J	MR/1.292
LEDA 093974	08 Jan 2012	04:51	6×180	0.85	1.380	J	LR/1.25
LEDA 093974	08 Jan 2012	05:20	4×340	0.73	1.298	J	MR/1.313
ESO -374-G044	22 Jan 2012	01:59	6×180	0.98	1.823	J	LR/1.25
ESO -374-G044	22 Jan 2012	02:42	4×340	0.97	1.609	J	MR/1.318

TABLE 4.3. ISAAC/VLT observation log for the 25 sources observed. (1) Source name; (2) Date of observation; (3) Starting time of acquisition; (4) Number of acquisitions and exposure time for each acquisition; (5) seeing; (6) airmass; (7) Filter used during the observations; (8) Grating used during the observations. We used a 0.8″ ×120″ slit width, corresponding in a velocity resolution of Δv ∼430 km s^{-1} and Δv ∼60 km s^{-1} for LR and MR modes, respectively.

Continued on next page

4.4 XSHOOTER/VLT Observations

X-shooter is a single target spectrograph mounted to the Cassegrain focus of the VLT UT3, covering in a single exposure the spectral range from the UV to the K band. The spectral format is fixed. The instrument is designed to maximize the sensitivity in the spectral range by splitting the incident light in three arms with optimized optics, coatings, dispersive elements and detectors. It operates at intermediate resolutions, R=4000−18000, depending on wavelength and slit width. The three arms are fixed format cross-dispersed échelle spectrographs that operate in parallel. Each one has its own slit selection device.

- The UV-Blue (UVB) spectrograph cover the 300−550 nm wavelenght range with a resolving power of 5100 (for a $1''$ slit width);
- The Visible spectrograph (VIS) covers the 550−1000 nm with a resolving power of 7500 (for a $0.9''$ slith width);
- The near IR (NIR) spectrograph covers the range 1000−2500 nm with a resolving power of 5300 (for a $0.9''$ slit width) and it is fully cryogenic.

The UVB detector is a 2048×4102, 15μm pixel size CCD from E2V (type CCD44-82) of which only a 1800×3000 pixels window is used. The CCD cryostat is attached to the camera with the last optical element acting as a window. The operating temperature is 153K. The CCD control system is a standard ESO FIERA controller shared with the VIS CCD. The VIS detector is 2048×4096, 15μm pixel size CCD from MIT/LL (type CCID-20). Like for the UVB arm, the cryostat is attached to the camera with the last optical element acting as a window. The operating temperature is 135K. It shares its controller with the UVB detector and the same readout modes are available. The NIR detector is a Teledyne substrate-removed HgCdTe, 2k×2k, 18μm pixel size Hawaii 2RG from of which only 1k×2k is used. It is operated at 81K.

The UVB and VIS detectors offer several readout modes, among which we choose the 100k/1pt/hg/1×2, while in the NIR only one readout mode is available. The main detectors characteristics are:

- *Number of pixel*: 2048×3000 for UVB; 2048×4096 for VIS; 2048×2048 for NIR;

- *Pixel size*: 15μm for UVB and VIS; 18μm for NIR;
- *Gain*: 0.62 e$^-$/ADU fot UVB; 0.595 e$^-$/ADU for VIS; 2.12 e$^-$/ADU for NIR;
- *Readout noise (RON)*: 2.5 e$^-$ for UVB; 3.1 e$^-$ for VIS; ~25 for NIR.

We have observed 11 AGN from our selected *Swift* sample using the multi-wavelength (3000−25000 Å) medium resolution spectrograph Xshooter. The first set of observations (4 sources) have been carried out in visitor mode on February 2013 and for every AGN it has been taken 2 exposure of ~300 s each, using a $1.0'' \times 11''$ wide slit for the UVB arm and a $0.9'' \times 11''$ for the VIS and NIR arms, corresponding to a ~60km s^{-1} spectral resolution and the nodding technique for all arms. The second set of Xshooter observations, including 7 sources, have been performed in service mode in the framework of the ESO period P93 (in particolar the targets have been observed between April 2014 and June 2014). As in 2013 we used a $1.0'' \times 11''$ wide slit for the UVB arm and a $0.9'' \times 11''$for the VIS and NIR arms, corresponding to a ~60km s^{-1} velocity resolution, and applied the nodding technique for all arms. We realized 10 exposure of ~200 s for each arm and each target. Due to the short slit it was not possible to include also a telluric star in the same acquisition, but both telluric and bright standard stars were observed within 30 minutes from the scientific target acquisitions. The data reduction have been performed using the Xshooter pipeline. The characteristics of the target observations are shown in Table 4.4.

4.5 Data reduction

The NIR data reduction has been realized using both *IRAF (Image Reduction and Analysis Facility)* and *ESO/MIDAS (European Southern Observatory-Munich Image Data Analysis System)* softwares. In order to perform a reliable reduction of the raw spectra we first grouped all the calibration data on the basis of their typology, inserting in each header the decriptor *imagetype* with the IRAF task *ccdhedit*. Thus the scientific images have been classified as *object*, the flat field images as *flat* and the other calibration images, such as the lamps, as *other*. In order to correct every scientific images for the

Xshooter observing log
slit width: 1.0″×11″ for UVB and a 0.9″×11″ for VIS and NIR
velocity resolution of $\Delta v \sim$60 km s^{-1}

object name **(1)**	**date** **(2)**	**UT** [hh:mm] **(3)**	**exposure** [s] **(4)**	**seeing** [″] **(5)**	**airmass** **(6)**	ARM **(7)**
ESO -263-G013	11 Feb 2013	00:47	2×150	1.2	1.93	NIR
ESO -263-G013	11 Feb 2013	00:47	2×50	1.2	1.93	VIS
ESO -263-G013	11 Feb 2013	00:47	2×50	1.2	1.93	UVB
NGC 3783	11 Feb 2013	08:21	2×300	0.94	1.09	NIR
NGC 3783	11 Feb 2013	08:21	2×263	0.94	1.09	VIS
NGC 3783	11 Feb 2013	08:21	2×230	0.94	1.09	UVB
MCG -05-23-16	11 Feb 2013	01:10	2×200	0.85	1.556	NIR
MCG -05-23-16	11 Feb 2013	01:10	2×163	0.85	1.556	VIS
MCG -05-23-16	11 Feb 2013	01:10	2×130	0.85	1.556	UVB
LEDA 093974	11 Feb 2013	08:03	2×300	0.92	1.281	NIR
LEDA 093974	11 Feb 2013	08:03	2×250	0.92	1.281	VIS
LEDA 093974	11 Feb 2013	08:03	2×225	0.92	1.281	UVB
NGC 4945	23 Apr 2014	04:47	10×291	1.07	1.139	NIR
NGC 4945	23 Apr 2014	04:47	10×259	1.07	1.139	VIS
NGC 4945	23 Apr 2014	04:47	10×225	1.07	1.139	UVB
NGC 6221	24 Apr 2014	06:07	10×291	1.01	1.249	NIR
NGC 6221	24 Apr 2014	06:07	10×259	1.01	1.249	VIS
NGC 6221	24 Apr 2014	06:07	10×225	1.01	1.249	UVB
2MASX J1830+0928	05 Jun 2014	04:15	10×291	0.70	1.42	NIR
2MASX J1830+0928	05 Jun 2014	04:15	10×259	0.70	1.42	VIS
2MASX J1830+0928	05 Jun 2014	04:15	10×225	0.70	1.42	UVB
NGC 5643	20 Jun 2014	03:50	10×291	1.14	1.24	NIR
NGC 5643	20 Jun 2014	03:50	10×259	1.14	1.24	VIS
NGC 5643	20 Jun 2014	03:50	10×225	1.14	1.24	UVB
ESO -234-G050	25 Jun 2014	06:38	10×291	0.78	1.112	NIR
ESO -234-G050	25 Jun 2014	06:38	10×259	0.78	1.112	VIS
ESO -234-G050	25 Jun 2014	06:38	10×225	0.78	1.112	UVB
NGC 7314	25 Jun 2014	07:50	10×291	0.67	1.012	NIR
NGC 7314	25 Jun 2014	07:50	10×259	0.67	1.012	VIS
NGC 7314	25 Jun 2014	07:50	10×225	0.67	1.012	UVB
NGC4941	21 Jul 2014	22:54	10×291	0.84	1.294	NIR
NGC4941	21 Jul 2014	22:54	10×259	0.84	1.294	VIS
NGC4941	21 Jul 2014	22:54	10×225	0.84	1.294	UVB

TABLE 4.4. Xshooter observation log for the 11 sources observed. (1) Source name; (2) Date of observation; (3) Starting time of acquisition; (4) Number of acquisitions and exposure time for each acquisition; (5) seeing; (6) airmass; (7) Xshooter arm. We used a a 1.0″×11″ for the UVB arm and a 0.9″×11″ for the VIS and NIR arms slit width, corresponding in a velocity resolution of Δv=60 km s^{-1} .

non-uniform CCD response and for the different pixel efficiency, we combine the *flat* and *bias* images, producing a normalized, averaged image used for the scientific corrections. The cosmic rays contamination has been removed with the IRAF task *crmedian*, in which all the pixel with counts larger than 10σ or smaller than 3σ with respect to the median signal are erased. This task has been applied to the scientific spectra twice: first before the λ calibration and then after the sky lines corrections. The latter has been performed in order to delete possible artefacts introduced during the reduction steps.

4.5.1 Sky lines subtraction and λ calibration

In order to perform an accurate λ calibration we decided to use the OH lines. For this purpose we developed a MIDAS procedure in which a 1-D sky lines image was produced starting from an averaged image of the scientific data for each source. We produced a MIDAS table using the OH sky atlas from Rousselot et al. (2000), that contains the main NIR sky emission lines identifications. We then applied the following IRAF tasks:

- *identify*, to perform a first line identification of the OH lines in the sky image;
- *reidentifiy*, for mapping geometric and dispersion distortion of the 2-D spectra;
- *fitcoords*, in which a two dimensional mapping of the image coordinates is performed.

Finally the task *transform* converts the scientific spectra dispertion axis from pixel to λ coordinates, performing the spectral λ calibration.

As decribed in the previous Sections (4.2, 4.3 and 4.4), we observed all our targets using the nodding technique, in order to perform a reliable correction for the sky lines contamination in the scientific data. This particular technique is commonly used in NIR spectroscopy and consists in the acquisition of several images of the same object but observed in different positions along the slit (i.e. A and B, see Figure 4.3).

We have acquired a set of couples of A and B observations for each object. The λ calibrated scientific couples have to be reprocessed in order to remove

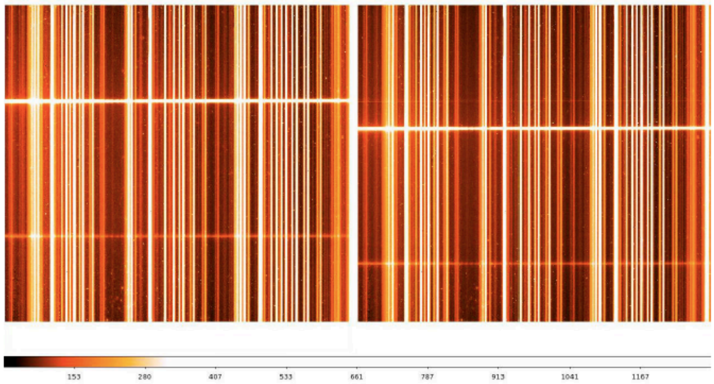

FIGURE 4.3. A LUCI target acquired with the nodding technique in the position A (left) and B (right). In this case also a telluric star has been included in the same observation.

from their spectra the sky emission lines, cleary visible in Figure 4.3. Thus, for each couple we have performed the operations $AB = A - B$ and $BA = B - A$, and, after an y-axis shift of the BA image, in order to have the target signals in the same position both in AB and in BA images, we obtained the final 2D scientific spectra from the operation $ABBA = AB + BA$ (see Figures 4.4 and 4.5).

These procedures have been performed using the IRAF tasks for the image operations, such as *imshift* and *imarith*, on each set of couple observations for every target. The overall 2D spectrum, λ calibrated and free from sky lines, of each source is then achieved combining togheter all the target's "ABBA" frames, previously created. We decided to use the IRAF task *imcombine*, in which is performed both an average of the imput images and a further cosmic rays correction. Figure 4.5 shows the final 2D spectra for 2MASX J0506+31 in which the sky emission lines are well removed. The same reduction procedures have been applied also for the telluric and standard star.

These standard reduction steps have been performed on all ISAAC and LUCI spectra, while for the Xshooter subsample we have used the Xshooter pipeline in the Esorex environment. In the following we will describe the spectra extraction and the flux calibration steps.

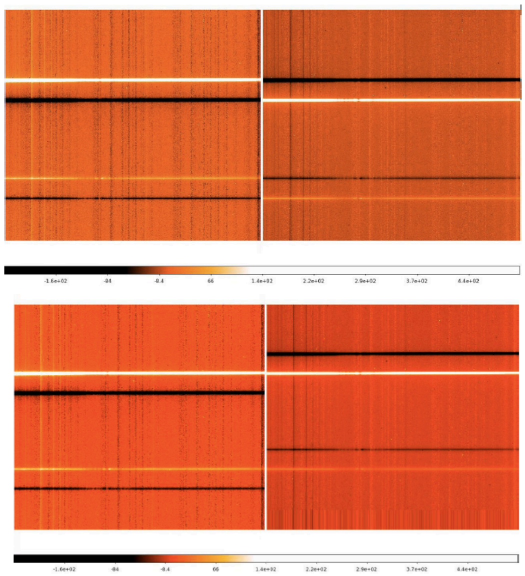

FIGURE 4.4. Up panel: a LUCI target acquired with the nodding technique after the operation AB (left) and BA (right). Bottom panel: the BA frame has been shifted in y-axis, in order to have the targhet signals in the same position both in AB and in BA images.

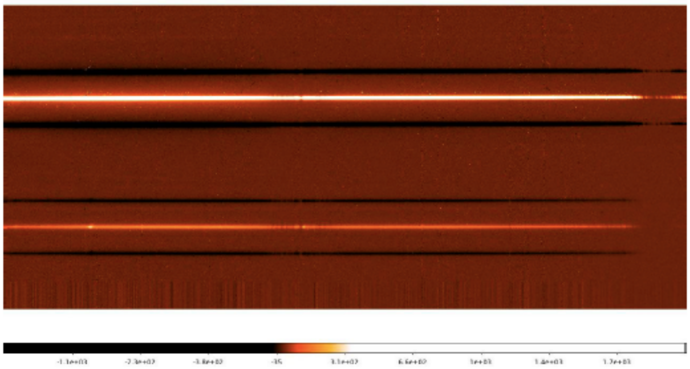

FIGURE 4.5. LUCI spectra of 2MASX J0506+31 resulting from the average of the all ABBA frames, after the nodding corrections.

4.5.2 Spectra extraction and flux calibration

At this point we have 2D scientific spectra, corrected for the flat field and cosmic rays, λ calibrated and polished by the OH emission lines contamination. From these images we have to derive the 1D spectra for both scientific and star (standard or telluric) frames in order to have all the ingredients for the flux

calibration step.
The spectra extraction has been performed using the IRAF task *apall*, a multi-step task that defines and extracts the data from the 2D CCD images. This task is rather complex and its operation strongly depends on several parameters:

- **Backgrounds parameters**: are used to determine how much the target signal emerges from the background. To this purpose the background has to be fitted with one among several functions available and it is possible to select the spectral region in which the background is estimated. In our extractions we choose a Chebyshev polynomial of order 3 for the background fit and the fitting region has been choosen interactively, paying attention to avoid damaged areas or the presence of cosmic rays.
- **Tracing parameters**: are used to traced the spectrum along the dispersion axis.
- **Extraction parameters**: these are used in order to optimize the spectrum extraction.

For the scientific spectra we have choosen the extraction aperture as narrow as possible in order to extract the very nuclear region of the AGN and not to lose too much flux. Instead, for the standard and telluric stars we have choosen a much broader extract aperture in order to take as much stellar flux as possible.

One of the main difficulties in conducting NIR ground-based spectroscopy is the presence of strong atmospheric absorptions highly variable in time. These features have to be corrected and in many cases satisfactory results can be achieved by dividing the target spectrum by the spectrum of a solar or type A star close to the object in the sky and observed closed in time. However when observing with high resolution spectrographs, the absorption features of the reference star are no longer diluited by the surrounding continuum and these can affect the target final spectrum, creating several pseudonoise absorptions. This noise can be minimized selecting reference stars with fewer features, such as O-B spectral type, but it could resuts in a unsatisfactory atmospheric correction in the final spectra, if the reference star is placed far from the target.

Thus, in order to perform an high quality atmospheric correction in our final spectra, all the observations have been carried out by rotating the slit in order include in the acquisition also a bright star (the telluric star), to be used in the flux calibration step for the OH absorptions corrections.
The flux calibration and the telluric correction steps have been realized following the method described by Vacca et al. (2003) for early spectral type star (A or B type), while we have followed the Maiolino et al. (1996) method in the cases of late type star (G or K). In both technique the flux calibration is performed using:

$$F_{cal}(\lambda) = F_{obs}(\lambda)\frac{F^{\star}_{mod}(\lambda)}{F^{\star}_{obs}(\lambda)/f}k \cdot 10^{-0.4(J^{\star}-J_0)} \tag{4.1}$$

in which $F_{cal}(\lambda)$ is the flux calibrated of the scientific target, $F_{obs}(\lambda)$ is the observed flux of the soruce, $F^{\star}_{mod}$ is a black body model for the spectral type of the reference star used which is normalized to unity in the observed band (e.g. at λ_c=1.25 μm for J spectra), $F^{\star}_{obs}(\lambda)$ is the observed reference star, f represents the fraction of stellar flux in the slit, $J^{\star}$ is the J magnitude (for K-band spectra we have used the star K magnitude) of the star and k is a constant that comes from the magnitude-flux conversion.

For LR spectra and early spectral type stars we have used the IDL procedure *xtellcor_general* (see Vacca et al. 2003) to apply the Equation 4.1 and thus obtain the final flux calibrated spectra. Instead, for higher resolution observations and in the cases of late spectral type reference star (G and K) we developed a MIDAS procedure that makes use of the Equation 4.1 and perform the flux calibrations of the scientific spectrum in input. The atmospheric and the Galactic extinction correction has been taken into account automatically during the flux calibration with the telluric standard star by using a non extincted stellar model.

Chapter 5

The new NIR virial relation to derive the AGN BH masses

5.1 Previous single epoch techniques

Nowadays there is robust evidence that almost every galaxy host a super massive black hole (BH; $M_{BH}=10^5$-10^9 $M_\odot$) and that many correlations exist between the BH mass and some of the host galaxy properties (e.g. bulge mass, luminosity and stellar dispersion; Ferrarese and Merritt, 2000; Gebhardt et al., 2000; Marconi and Hunt, 2003; Sani et al., 2011). Then, it has been argued that the existence of these scaling relationships implies a common evolutionary path between galaxies and the growth of SMBHs (the AGN/galaxy co-evolution scenario).

In the last decade, using virial based techniques in the optical band, it has been possible to measure the BH mass on large type 1 AGN (AGN1) samples and therefore derive the super massive BH mass function (Greene and Ho, 2007a; Kelly et al., 2009, 2010; Merloni et al., 2010; Bongiorno et al., 2014). These measures are based on the Single Epoch (SE) BH mass estimates. By combining the velocity of the Broad Line Region (BLR) clouds (assuming Keplerian orbits) along with their distance R it is possible to determine the total mass contained within the BLR (which is dominated by the BH) in a simple way using:

$$M_{BH} = \frac{f \Delta V^2 R}{G}, \tag{5.1}$$

where G is the gravitational constant and f is a factor that depends on the geometric and kinematic structure of the BLR (Kaspi et al., 2000). These techniques derive the AGN BH mass using single epoch (SE) spectra to measure ΔV from the full width at half maximum (FWHM) of some of the BLR lines (typically: Hβ or MgII2798Å or C IV 1459Å) and R from either the continuum or the line luminosities, L, which have been proved to be proportional to R^2 (i.e. $R \propto L^{0.5}$; Bentz et al., 2006). Therefore, the SE estimates are based on relations of the type:

$$\log M_{\rm BH} = \log(\mathrm{FWHM}^{\alpha} \cdot \mathrm{L}^{\beta}) + \gamma, \tag{5.2}$$

where $\alpha \sim 2$, $\beta \sim 0.5$ (e.g. Wandel et al., 1999; Vestergaard, 2002, 2004; Vestergaard and Osmer, 2009; McLure and Jarvis, 2002, but see also Dietrich and Hamann 2004). These relationships have typical spreads of ~0.5 dex.

However these measurements are affected by selection biases against those obscured or partially obscured sources where the AGN component does not dominate in the optical: type 2 AGN (AGN2), intermediate class AGN (AGN1.8 and AGN1.9) or even low mass BH ($M_{BH} \leq 10^6$ $M_{\odot}$) AGN1. Indeed, in these cases, in the (rest frame) optical band, either the broad line component is not visible or, in any case, the AGN continuum and line luminosities are affected by severe obscuration and galaxy contamination thus preventing a reliable estimate of the BH mass.

There are, in summary, indications that the SE techniques do not allow to obtain an un-biased estimate of the density of the low-luminosity and, therefore, lowest-mass BH ($M_{BH} \leq 10^6$ $M_{\odot}$) class of AGN. Such a bias could have strong implications on our understanding on the AGN/galaxy evolution.

Indeed, the density of low mass BHs in the local universe provide unique tests for studies of BH formation and growth, galaxy formation and evolution. In current models of galaxy evolution in a hierarchical cosmology, SMBHs must have been built up from accretion onto much smaller seeds, in conjuction with merging with other BHs. These models also predict that smaller scale structures form at later times (cosmic downsizing), and one might expect that seeds BHs in these smaller systems may not have had enough time to be fully grown. This means that low-mass BHs likely contain clues about the formation of the first black holes, thus the mass function of the present day low-mass black holes and their host galaxies properties can be used to discriminate between different models for seeds BHs and help shed light on the coevolution of BHs and galaxies (see Dong and De Robertis, 2006; Greene and Ho, 2007b; Dong et al., 2012; Greene, 2012).

In the last few years Landt et al. (2008, 2011, 2013) have studied quasi-simultaneous near-IR (NIR) and optical spectra of a sample of well-known broad-emission line AGN, whose BH masses were already determined from reverberation campaigns. These studies have allowed the calibration of a NIR relationship for estimating AGN BH masses based on the widths of the Paschen hydrogen broad emission lines and the total 1 μm continuum luminosity (Landt et al., 2011, 2013). However the virial relationship developed in Landt et al. (2011, 2013) makes use of the 1 μm continuum luminosity, which has to be derived by a Spectral Energy Distribution (SED) fitting method and can suffer from galaxy contamination especially for intrinsic low-luminosity AGNs.

We have then decided to calibrate new virial relationships based on the Paβ broad emission line FWHM combined with either the hard X-ray or the Paβ broad emission line luminosities (see also Kim et al., 2010, for similar SE methods based on the Paα and Paβ emission-line luminosities). Such relations are potentially able to be applied on both the low-luminosity and the optically more obscured AGN. The method has been tested over one of the lowest BH mass ($\sim 10^5 M_\odot$; see section 6.2.2) AGN, NGC 4395, which has been spectroscopically observed in the NIR at the Large Binocular Telescope (LBT) in the framework of a large programme aimed at measuring the BH mass of low-luminosity or type 2 AGN (Onori et al., in preparation), included in the 22 month Swift/Burst Alert Telescope (BAT) catalogue (Tueller et al., 2010).

Unless otherwise stated, all quoted errors are at the 68% confidence level. We assume $H_0 = 70$ km s^{-1}Mpc^{-1}, $\Omega_m = 0.3$ and $\Omega_\Lambda = 0.7$.

5.2 The calibration sample

As previously discussed, we are interested in deriving new BH mass virial relationships based on the measure of the width of the BLR component in the Paβ emission line. In order not to suffer from problems related to the galaxy contamination, we have replaced the 1μm continuum luminosity used by Landt et al. (2013) as the BLR size indicator, with either the hard X-ray 14-195 keV band luminosity, L_X, such as measured by Swift/BAT survey (Baumgartner et al., 2013), or the luminosity of the Paβ, $L_{Pa\beta}$, itself (see Kim et al. (2010), for a similar study based on the Paα and Paβ emission-line luminosities).

The calibration sample contains 20 AGNs and is quite the same of Landt et al. (2011, 2013), infact most of their sources are listed in the Swift/BAT catalogue (Baumgartner et al., 2013). When available, we have used the BH mass values listed in Grier et al. (2013) where the new estimate of the geometrical f-factor $f = 4.31$ was adopted. All the remaining BH masses, which were originally published using $f = 5.5$, have then been converted to $f = 4.31$. In Table 5.1 we present the main characteristics of our calibration sample, such as: redshift, optical spectroscopic classification, BH mass and the relative reference, 14-195 keV hard X-ray luminosity and the FWHM of the broad component of the Paβ.
The FWHMs have been corrected for instrumental resolution using the values reported in Landt et al. (2008, 2013). In particular the source 3C 120 has been observed with an average spectral resolution of FWHM $\sim$ 180 km s^{-1}, while Mrk 279, NGC 3516, NGC 4051 and PG 0844+349 spectra have a resolution of FWHM $\sim$ 400 km s^{-1} (Landt et al., 2013). The instrumental resolution for the remaining of the sources is FWHM $\sim$ 350 km s^{-1} (Landt et al., 2008).

5.2.1 Fit of the virial relationship using $\mathrm{L_X}$

We have performed a linear fit of the form

$$\log\left(\frac{\mathrm{M_{BH}}}{\mathrm{M_\odot}}\right) = a \cdot \log\left[\left(\frac{\mathrm{FWHM_{Pa\beta}}}{10^4\,\mathrm{km\,s^{-1}}}\right)^2 \left(\frac{\mathrm{L_X}}{10^{42}\ \mathrm{erg\,s^{-1}}}\right)^{0.5}\right] + b, \tag{5.3}$$

where $\mathrm{M_{BH}}$ is the BH mass, $\mathrm{FWHM_{Pa\beta}}$ is the measure of the width of the broad component of the Paβ emission line, corrected for instrumental broadening, and $\mathrm{L_X}$ is the 14-195 keV intrinsic luminosity.
The fit was carried out on a sample of 19 out of 20 AGN, as one galaxy misses the $\mathrm{L_X}$ measurement (see Table 5.1). We have solved the least-squares problem using the fitting routine FITEXY (Press et al., 2007) that can incorporate errors on both variables and allows us to account for intrinsic scatter. The uncertainties on $\mathrm{M_{BH}}$ are listed in Table 5.1, while the errors on the virial product (the x-axis) depend on the uncertainties on the measures of FWHM and $\mathrm{L_X}$. We have calculated the uncertainties on the hard X-ray luminosity $\mathrm{L_X}$

TABLE 5.1. Calibration Sample.

Object Name (1)	z (2)	class (3)	M_{BH} $[M_\odot]$ (4)	ref (5)	$\log L_X$ $[\mathrm{erg\,s^{-1}}]$ (6)	$\mathrm{FWHM}_{\mathrm{Pa}\beta}$ $[\mathrm{km\,s^{-1}}]$ (7)	$\log L_{\mathrm{Pa}\beta}$ $[\mathrm{erg\,s^{-1}}]$ (8)
3C 120	0.0330	S1.0	$5.26\pm0.52 \cdot 10^{7}$	G13	44.38	2727	...
3C 273	0.1583	S1.0	$6.94\pm1.47 \cdot 10^{8}$	P04	46.48	2895	43.64
Ark 120	0.0323	S1.0	$101^{+17}_{-25} \cdot 10^{6}$	G13	44.23	5102	42.12
Mrk 79	0.0222	S1.2	$8.28^{+1.9}_{-3.2} \cdot 10^{7}$	G13	43.72	3506	41.28
Mrk 110	0.0353	S1n	$2.24^{+0.56}_{-0.91} \cdot 10^{7}$	G13	44.22	1886	41.60
Mrk 279	0.0304	S1.0	$3.10\pm0.47 \cdot 10^{7}$	G13	43.92	3546	...
Mrk 290	0.0296	S1.5	$1.90\pm0.29 \cdot 10^{7}$	D10	43.67	4228	41.46
Mrk 335	0.0258	S1n	$1.11\pm0.29 \cdot 10^{7}$	P04	43.45	1825	41.37
Mrk 509	0.0344	S1.5	$9.57\pm0.43 \cdot 10^{7}$	G13	44.42	3057	42.12
Mrk 590	0.0264	S1.0	$3.15^{+0.52}_{-0.69} \cdot 10^{7}$	G13	43.42	3949	40.33
Mrk 817	0.0314	S1.5	$6.29^{+0.95}_{-1.08} \cdot 10^{7}$	G13	43.77	5519	41.47
Mrk 876	0.1290	S1.0	$2.19\pm1.01 \cdot 10^{8}$	P04	44.73	6010	42.50
NGC 3227	0.0039	S1.5	$2.24^{+0.86}_{-0.91} \cdot 10^{7}$	G13	42.56	2934	40.03
NGC 3516	0.0088	S1.5	$3.10^{+0.30}_{-0.26} \cdot 10^{7}$	G13	43.31	4451	...
NGC 4051	0.0023	S1.0	$2.2^{+0.2}_{-0.4} \cdot 10^{6}$	G13	41.67	1633	...
NGC 4151	0.0033	S1.5	$3.62^{+0.39}_{-0.22} \cdot 10^{7}$	G13	43.12	4654	40.43
NGC 4593	0.0090	S1.0	$9.1^{+1.7}_{-1.3} \cdot 10^{6}$	G13	43.20	3775	40.68
NGC 5548	0.0172	S1.5	$5.95^{+0.73}_{-0.86} \cdot 10^{7}$	G13	43.72	6516	41.37
NGC 7469	0.0163	S1.5	$2.70\pm0.60 \cdot 10^{7}$	G13	43.60	1758	40.98
PG 0844+349	0.0640	S1.0	$7.24\pm2.99 \cdot 10^{7}$	P04	...	2377	41.99

Notes: (1) AGN names; (2) redshift from Baumgartner et al. (2013); (3) source classification from Landt et al. (2008) or NED (where S1.0 = Seyfert 1, S1.2-S1.5 = intermediate Seyfert 1, S1n = narrow-line Seyfert 1); (4) BH mass (in solar masses) from reverberation mapping campaigns; (5) reference for the BH mass, where D10: Denney et al. (2010) but adopting f = 4.31, G11: Graham et al. (2011), G13: Grier et al. (2013), P04: **?** but adopting f = 4.31; (6) logarithm of the 14-195 keV intrinsic luminosity (from Baumgartner et al., 2013); (7) FWHM of the broad emission line component of Paβ (corrected for instrumental resolution) from Landt et al. (2008, 2013); (8) logarithm of the luminosity of the Paβ BLR component from Landt et al. (2008, 2013).

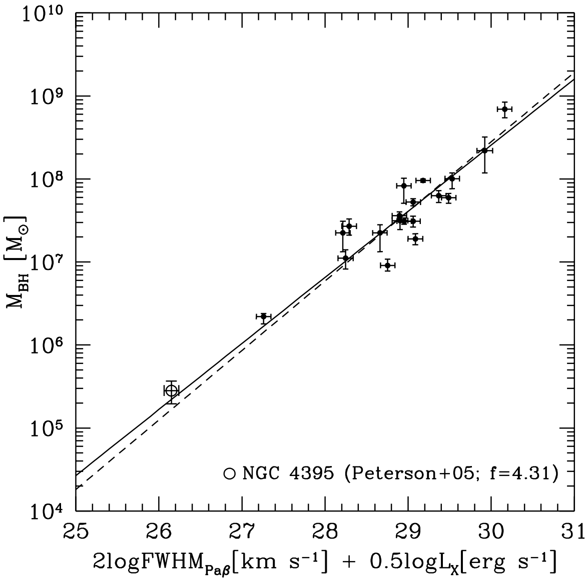

FIGURE 5.1. Black Hole masses determined from optical reverberation campaigns (adopting a geometrical f-factor $f = 4.31$) versus the virial product between the hard X-ray luminosity L_X in the 14-195 keV band and the FWHM of the broad component of the Paβ emission line. The dashed line shows our best fit using the calibration sample shown in Table 5.1, while the continuos line is our best fit (eq. 5.6) including also NGC 4395 as measured by Peterson et al. (2005), but adopting $f = 4.31$ instead of $f = 5.5$ (see next chapter for more details).

rescaling the 90% confidence level of the flux in the 14-195 keV band presented in the 70 month Swift/BAT catalogue (Baumgartner et al., 2013) to the 68% confidence level. As far as the FWHM measures are concerned, although in some cases the uncertainties are reported in literature, following the studies of Grupe et al. (2004); Vestergaard and Peterson (2006); Landt et al. (2008); Denney et al. (2009), we have preferred to assume a common uncertainty of 10%.

The best fit provided a slope $a = 0.837 \pm 0.040$ and a y-intercept $b = 7.609 \pm 0.023$ (see dashed line in Figure 5.1). The data have a correlation coefficient $r = 0.90$, which corresponds to a probability as low as $\sim 10^{-7}$ that the data are randomly extracted from an uncorrelated parent population. The resulting observed spread is 0.24 dex, while the intrinsic spread (i.e. once the contribution from the data uncertainties has been subtracted in quadrature) results to be 0.21 dex.

Following Graham and Scott (2013), we have also used the Tremaine et al.'s (2002) modified version of the routine FITEXY which minimizes the quantity

$$\chi^2 = \sum_{i=1}^{N} \frac{(y_i - ax_i - b)}{\sigma_{y_i}^2 + a^2\sigma_{x_i}^2 + \varepsilon^2}, \tag{5.4}$$

where the intrinsic scatter (in the y-direction) is denoted by the term ε, and the measurement errors on the N pairs of observables x_i and y_i, (i.e. the virial product $(2\log \mathrm{FWHM}_{\mathrm{Pa}\beta} + 0.5 \log \mathrm{L_X})$ and the BH masses, respectively) are denoted by σ_{x_i} and σ_{y_i}. It results, indeed, that the intrinsic scatter of 0.21 dex makes the reduced χ^2 (χ^2/ν) from equation 5.4 (where ν are the degrees of freedom) equal to $\sim$1.

5.2.2 Fit of the virial relationship using $\mathrm{L}_{\mathrm{Pa}\beta}$

In order to look for a virial relationship able to measure the BH masses using only NIR spectroscopic data, we have substituted $\mathrm{L_X}$ with $\mathrm{L}_{\mathrm{Pa}\beta}$ and then, in analogy with the previous section, have performed a linear fit of the form:

$$\log\left(\frac{\mathrm{M_{BH}}}{\mathrm{M}_\odot}\right) = a \cdot \log\left[\left(\frac{\mathrm{FWHM}_{\mathrm{Pa}\beta}}{10^4\,\mathrm{km\,s^{-1}}}\right)^2 \left(\frac{\mathrm{L}_{\mathrm{Pa}\beta}}{10^{40}\ \mathrm{erg\,s^{-1}}}\right)^{0.5}\right] + b. \tag{5.5}$$

In this case the fit was carried out on a sample of 16 AGN as four galaxies miss the $L_{Pa\beta}$ measurement (see Table 5.1). As discussed in the previous section, an uncertainty of 10% on $L_{Pa\beta}$ was used. The best fit provided a slope $a = 0.908 \pm 0.060$ and a y-intercept $b = 7.834 \pm 0.031$ (see dashed line in Figure 5.2). The data have a correlation coefficient $r = 0.80$, which has a probability as low as $\sim 10^{-4}$ that the data are randomly extracted from an uncorrelated parent population. The resulting observed spread is 0.31 dex, while the intrinsic spread results to be 0.28 dex. Although this relationship has an intrinsic scatter larger than measured in the previous relation using L_X, as already discussed, it has the big advantage that it just needs NIR spectroscopy of the Paβ emission line (without using X-ray observations) to derive the AGN BH mass.

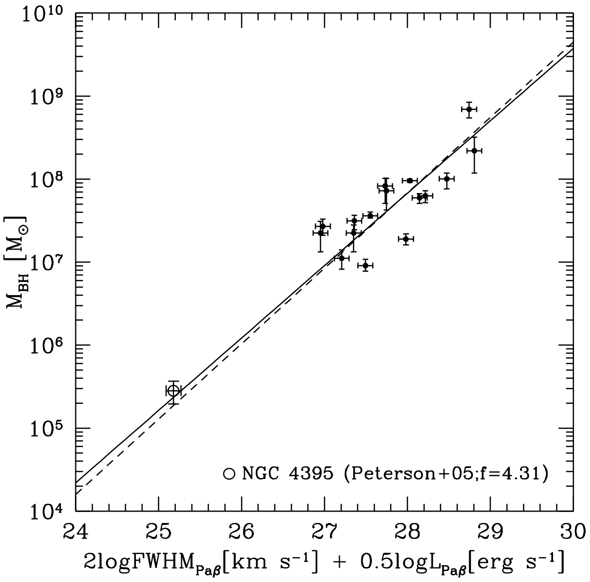

FIGURE 5.2. Black Hole masses determined from optical reverberation campaigns (adopting a geometrical f-factor $f = 4.31$) versus the virial product between the luminosity $L_{Pa\beta}$ and the FWHM of the broad component of the Paβ emission line. The dashed line shows our best fit using the calibration sample shown in Table 5.1, while the continuos line is our best fit (eq. 5.7) including also NGC 4395 as measured by Peterson et al. (2005), but adopting $f = 4.31$ instead of $f = 5.5$.

5.3 The BH Mass of NGC 4395

The two above virial relationships can be used to measure the BH mass of NGC 4395, whose line fitting procedure is desscribed in Section 6.2. Thanks to our NIR observations, it results $\mathrm{M_{BH}}$=1.7 $^{+1.3}_{-0.7}\times 10^5 M_\odot$ and $\mathrm{M_{BH}}$=1.9 $^{+2.2}_{-1.0}\times 10^5 M_\odot$, if the equation based on $\mathrm{L_X}$ (for NGC 4395 $\log\mathrm{L}_X$=40.79, with a 1σ uncertainty of 9%; Baumgartner et al., 2013) and $\mathrm{L_{Pa\beta}}$ are used, respectively. Because of the spreads of the previous fits, as expected, the mass derived using the X-ray luminosity dependent equation is more accurate than that measured using the relation dependent from the Paβ luminosity. The two estimates are in statistical agreement at less than 1σ confidence level, but are not independent from each other, as they both depend from the same $\mathrm{FWHM_{Pa\beta}}$ measurement. It is therefore not possible to use both of them to derive a weighted mean estimate of the NGC 4395 BH mass. We then consider the measure $\mathrm{M_{BH}}$=1.7 $^{+1.3}_{-0.7}\times 10^5 M_\odot$ (based on the more accurate relationship which uses $\mathrm{L_X}$, eq. 5.3) as our best estimate of the BH mass in NGC 4395.

As discussed in section 6.2.1, the BH mass of NGC 4395 has already been estimated by other authors (Peterson et al., 2005; Graham et al., 2011; Edri et al., 2012). Our measure agrees well within the uncertainties, with the above previous measures (once the same geometrical factor $f = 4.31$ is adopted). The BH mass measure by Graham et al. (2011) is based on the same reverberation mapping analysis of the C IV line by Peterson et al. (2005), then, once $f = 4.31$ is used, both are consistent with $\mathrm{M_{BH}}$=2.81 $^{+0.86}_{-0.66}\times 10^5 M_\odot$ (see Figures 5.1 and 5.2, where our Paβ measures and the SWIFT/BAT 14-195 keV luminosity have been used to plot the measure by Peterson et al. (2005)).

The BH mass by Edri et al. (2012) is based on the reverberation mapping analysis of the Hβ line and, once $f = 4.31$ is assumed, it corresponds to $\mathrm{M_{BH}} = (2.69 \pm 1.42) \times 10^5 M_\odot$. If, instead, our Pa$\beta$ emission-line measures are used together with the relation by Kim et al. (2010, their eq. 10. See discussion in the next section), a BH mass for NGC 4395 of $\mathrm{M_{BH}}$=1.8 $^{+1.5}_{-0.8}\times 10^5 M_\odot$ is obtained. A result very close to our measure.

5.4 Near Infrared SE BH mass relations including NGC 4395

As the previous independent BH mass estimate of NGC 4395 by Peterson et al. (2005) is compatible with our measure, we decided to include the measure by Peterson et al. (2005) in the calibration sample and rerun the fits in order to tie and extend the virial SE relationships at masses as low as $M_{BH} \sim 10^5 M_\odot$. This inclusion would not have been possible without our LUCI/LBT spectroscopic observations of the Paβ emission line.

The inclusion of NGC 4395 in the calibration sample does not significantly change the results of the fits. If the relationship based on L_X is used, the best fit provides (see Figure 5.1)

$$\log(M_{BH}/M_\odot) = 0.796(\pm0.031)\log\left[\left(\frac{FWHM_{Pa\beta}}{10^4\,km\,s^{-1}}\right)^2\left(\frac{L_{14-195keV}}{10^{42}\ erg\,s^{-1}}\right)^{0.5}\right] +7.611\ (\pm0.023)\quad(\pm0.20) \tag{5.6}$$

The resulting observed spread is 0.23 dex, while the intrinsic dispertion is 0.20 dex.

If the relationship based on $L_{Pa\beta}$ is used, the best fit provides (see Figure 5.2)

$$\log(M_{BH}/M_\odot) = 0.872(\pm0.040)\log\left[\left(\frac{FWHM_{Pa\beta}}{10^4\,km\,s^{-1}}\right)^2\left(\frac{L_{Pa\beta}}{10^{40}\ erg\,s^{-1}}\right)^{0.5}\right] +7.830(\pm0.030)\quad(\pm0.27) \tag{5.7}$$

The resulting observed spread is 0.30 dex, while the intrinsic spread results to be 0.27 dex.

The same kind of relationship has been previously measured by Kim et al. (2010) using similar data but covering a narrower BH mass range ($10^7 - 10^9$ $M_\odot$). In order to compare the two relations it is necessary to a) rescale the masses of Kim et al. (2010) to a $f = 4.31$ geometrical factor instead of the $f = 5.5$ used by them. b) Followig their analysis we have to correct the Paβ luminosities and FWHM measured by Landt et al. (2008, 2013) for 1.08 and 0.90 factors (respectively), in order to take into account the narrow line component effects in the line profile fits. Once these corrections are applied, the two relations result in fairly good agreement within the errors: they give the same results for $M_{BH} \sim 10^7$, while at $M_{BH} \sim 10^9$ and $M_{BH} \sim 10^5$ our estimates are ~0.2 dex smaller and larger, respectively.

5.5 Luminosity of the Paβ as a function of the 14-195 keV Luminosity

The two above discussed virial relationships (eqs. 5.6 and 5.7) imply that a significant correlation should exist between the Paβ emission line luminosity (the BLR component), $L_{Pa\beta}$, and the 14-195 keV luminosity, L_X. Similar kind of relationships have been already studied and derived by other authors. For example, Panessa et al. (2006) studied the correlation between the Hα luminosity and the 2-10 keV luminosity on a sample of 87 Seyfert galaxies and low-z QSOs, finding:

$$\log L_{2-10\mathrm{keV}} = 1.06(\pm 0.04) \cdot \log L_{\mathrm{H}\alpha} - 1.14\ (\pm 1.78). \tag{5.8}$$

Using our calibration sample (with NGC 4395 included) we performed a free slope fit of the relation

$$\log\left(\frac{L_{\mathrm{Pa}\beta}}{10^{42}\mathrm{erg\ s^{-1}}}\right) = \mathrm{a} \cdot \log\left(\frac{L_{14-195\mathrm{keV}}}{10^{44}\mathrm{erg\ s^{-1}}}\right) + \mathrm{b} \tag{5.9}$$

The data ($\log L_{\mathrm{Pa}\beta}$ and $\log L_{\mathrm{X}}$) have a correlation coefficient $r = 0.97$ which corresponds to a probability of $\sim 10^{-10}$ of being drawn from an un-correlated population, while the fit provides a slope $a = 0.963 \pm 0.011$ and a y-intercept $b = -0.500 \pm 0.013$ (dashed line in Figure 5.3), with an intrinsic spread of 0.26 dex. If a unitary slope is assumed, then our fit provides:

$$\log\left(\frac{L_{\mathrm{Pa}\beta}}{10^{42}\mathrm{erg\ s^{-1}}}\right) = \log\left(\frac{L_{14-195\mathrm{keV}}}{10^{44}\mathrm{erg\ s^{-1}}}\right) - 0.492(\pm 0.013) \pm 0.26 \tag{5.10}$$

(see the black continuous line in Figure 5.3). If we assume a photon index $\Gamma = 1.8$ and a ratio of $\log(\mathrm{Pa}\beta/\mathrm{H}\alpha) = -1.2$ (case B recombination), our fit is in partial agreement with eq. 5.8 (from Panessa et al., 2006): eq. 5.8 should be read $\log L_{\mathrm{Pa}\beta} = 0.943 \cdot \log L_{14-195\mathrm{keV}} - 0.5$ which predicts, in the range $42 \leq \log L_{14-195\mathrm{keV}} \leq 46$, BLR Pa$\beta$ luminosities ~0.4 dex lower than observed on average in our data. This discrepancy could be attributed to the

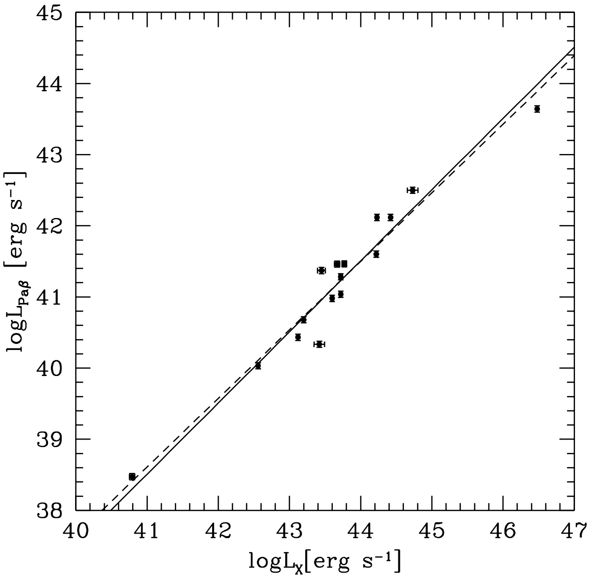

FIGURE 5.3. Luminosity of the BLR component of the Paβ as a function of the intrinsic 14-195 keV band luminosity, L_X. The dashed line is our best fit with free slope, while the black continuous line is our best fit with unitary slope (eq. 5.10).

assumption of a case B recombination ratio between the Paβ and Hα lines. There is indeed evidence that in AGN the Paschen line ratios rule out case B recombination (Soifer et al., 2004; Glikman et al., 2006).

Chapter 6

The broad component of BLR emission lines in AGN2

6.1 The FWHM of the emission line components.

In order to perform a reliable line fitting procedure, and thus to derive the FWHM of the emission lines of interest, we decided to use the software *XSPEC*. The uncertainties on each spectrum have been estimated using our own-made MIDAS routine, developed for this purpose. For each target we used 1) the galaxy's spectrum λ calibrated using the sky OH emission lines as a reference, 2) the sky image and 3) the final flux calibrated spectra.

The OH image was used to sample the contribution of the background. Toghether with the galaxy's spectrum and the instrumental properties (gain and number of scientific raw spectra involved in the reduction process), we calculated the noise as:

$$\left(\frac{S}{N}\right)_\lambda = \frac{\Phi_\lambda}{\sqrt{\Phi_\lambda + \Sigma_\lambda}}, \tag{6.1}$$

where Φ_λ is the spectrum flux, while Σ_λ is the sky contribution which has been calculated taking into account the extraction aperture. Furthermore, in order to obtain reliable S/N values, we requested that the noise fluctuations were compatible with those measured in a spectral control region, free from particular features, in the flux calibrated spectra.

Although the low redshift of our targets, the spectra have been converted to the rest frame wavelenght. After that, we performed the fit of the emission lines of interest, in order to derive their rest frame full width at half maximum, FWHM_{Rest}. Moreover due to the presence of sistematic errors on the FWHM estimates and following the studies of Grupe et al. (2004), Vestergaard and Peterson (2006), Landt et al. (2008), Denney et al. (2009), we have preferred to assume a common uncertainty of 10% for all the FWHM instead of the fit errors of σ_λ.

We found signatures of broad emission line component in Paα , Paβ , Paγ or He I (depending on the redshift of the source) in 13 out of 41 obscured AGNs of our randomly selected SWIFT70M sample. In the following sections we describe the past literature and the line fitting procedure of each of these sources, while a detailed explanation of target observations are reported in Section 4.2, for LUCI spectrograph, Section 4.3 for ISAAC and Section 4.4 for Xshooter instrument. The data reduction steps, including λ calibration, NIR sky lines sutraction and flux calibrations, are described in Section 4.5.

6.2 NGC 4395

6.2.1 NGC 4395 in the literature

NGC 4395 is a nearby (z=0.0013), surprisingly small bulgeless (Sd) galaxy, hosting one of the smallest active super massive BH ($10^4 - 10^5 M_\odot$) ever found. Contrary to objects of the same kind, the emission-line properties, the optical to X-ray variability pattern and the inferred accretion rate of NGC 4395 are those typical of the Seyfert class, of which this source is usually considered to represent the least luminous member.

The optical spectrum reveals very strong, narrow emission lines showing weak broad wings having full width zero intensity FWZI = 4000−8000 km s^{-1} in the permitted-line profiles. Based on the relative intensities of the narrow and broad components, Filippenko and Sargent (1989) originally classified the nucleusof NGC 4395 as a type 1.8 or type 1.9 Seyfert. Later, using higher resolution HST spectroscopy, the nucleus of NGC 4395 has been classified as a type 1 Seyfert (Filippenko et al., 1993). The Hβ and Hα broad lines are shown in Figure 6.2.1 left and right side, respectively, taken from Ho et al. (1995) spectra.

NGC 4395 is a hard-spectrum variable X-ray point source (Moran et al. (1999); Ho et al. (2001); Shih et al. (2003)) and it is a compact, high brightness temperature radio source, although it is formally a radio quiet AGN (Moran et al. (1999); Ho and Peng (2001)). Indeed, the stronger flux variability characterizing systematically the soft X-ray bands can be attributed to a complex, multi-zone warm absorber, whose properties have been discussed in detail in

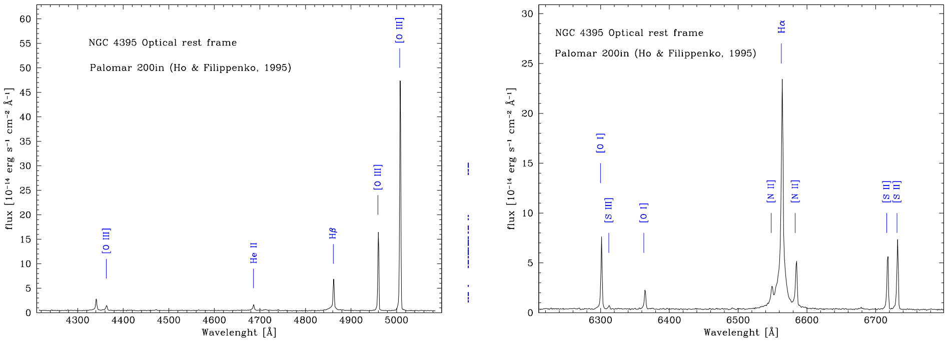

(a) NGC 4395 Hβ + [O III] (b) NGC 4395 Hα +[N II]

FIGURE 6.1. Optical spectra of NGC4395 from Ho et al. (1995).The broad components of Hβ (left) and Hα (right) are shown.

several works (Iwasawa et al. (2000); Shih et al. (2003)).

Different methods have been employed in the last years to derive the central BH mass of NGC 4395: the first estimate obtained through reverberation mapping of the C IV line is $M_{BH}=(3.6\pm1.1)\times10^5 M_\odot$ (Peterson et al., 2005), but it has been halved to $(1.8\pm0.6)\times10^5 M_\odot$ due to the updated virial f-factor in Graham et al. (2011). The last up to date broadband photometric reverberation, made by Edri et al. (2012) using the Hβ line, has found an even lower mass of $M_{BH}=(4.29\pm2.6)\times10^4 M_\odot$; this is essentially due to the much smaller geometrical f-factor used (f = 0.75 instead of f = 5.5 used by Peterson et al. (2005)). The lack in this galaxy of a significant bulge and the stringent upper limit of 30 km s^{-1} on its velocity dispersion confirm a value of the order of $10^4-10^5 M_\odot$ on its BH mass (Filippenko and Ho, 2003). Anyhow, the nucleous of NGC 4395 falls somewhere between the stellar-mass black holes found in Galactic X-ray binaries and the supermassive black holes residing inside AGN. Thus it can provide usefull information about the relationship between these two populations, it provides an opportunity to extend the mass range of the BH mass - bulge galaxy properties scaling relationships toward the low mass end and, in the framework of current models of galaxy evolution in a hierarchical cosmology, it can contains clues about the formation of the first black holes.

6.2.2 NGC 4395: LUCI observations and lines fit

We have observed NGC 4395 on December 5th, 2012, at the LBT with the NIR spectrograph LUCI in the zJ band using the grating 200 H+K in combination with the zJspec filter. We used a $1'' \times 2.8'$ wide slit, corresponding to a $\sim$ 220 km s^{-1} spectral resolution. The spectrum of NGC 4395 was extracted with an aperture of $1.5''$ and it was calibrated in flux using a telluric star. The final spectrum is shown in Figure 6.2, left side.

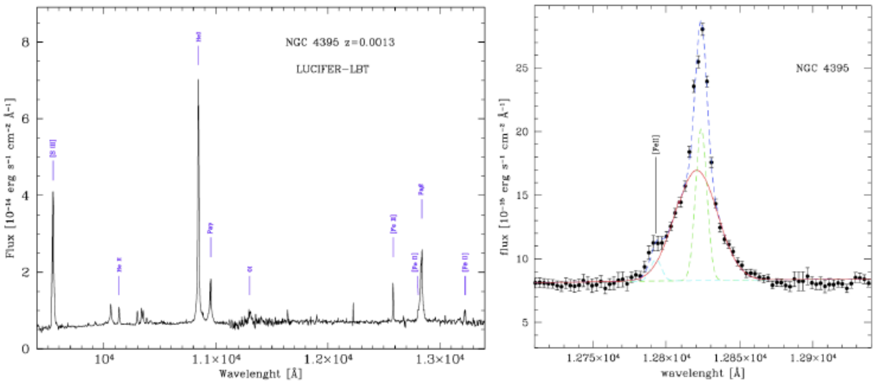

FIGURE 6.2. Left: flux calibrated LUCI/LBT NIR spectrum of NGC 4395. Right: rest frame, flux calibrated LUCI/LBT NIR spectrum of NGC 4395 in proximity of Paβ emission line. The green dashed line shows the narrow component of Paβ , the cyan dashed line shows the [Fe II] λ 12791 Å blended with the Paβ . The red solid line is the broad component of Paβ . The blue dashed line shows the complete fit.

The NGC 4395 LUCI/LBT NIR spectrum (Figure 6.2, left side) is rich of both forbidden and permitted emission lines. It clearly shows broad component in He I and Paγ , that are well separated, and in the Paβ lines. The presence of an intense narrow [Fe II] λ 12570 Å emission line allowed us to an accurate estimation of the NLR contribution to the Paβ line in the fitting procedure.
We fitted the Paβ profile paying attention to disentagle the broad emission from the narrow one. Although the redshift of NGC 4395 is quite low, the spectrum has been converted to the rest frame. The continuum has been estimated with a power law, while the contribution from the NLR has been modelled with a Gaussian model whose width has been fixed to that measured for the forbidden emission line [Fe II] λ 12570 Å (FWHM$_{Rest}$ = 211 km s^{-1}).

LUCI/LBT NGC 4395 Paβ line fit				
Component **(1)**	$\lambda_{\mathbf{c}}$ [Å] **(2)**	σ_λ [Å] **(3)**	**Norm**$_{Rest}$ [$\times 10^{-14}$] **(4)**	**FWHM**$_{Rest}$[a] [**km s**$^{-1}$] **(5)**
[Fe II]	12584.00±0.12	3.84 fixed	9.22±0.43	211
[Fe II] blend *	12806.80±0.14	3.84 fixed	1.45±0.78	211
Paβ Narrow *	12837.10±0.14	3.84 fixed	10.35±0.95	211
Paβ Broad	12834.00±0.40	14.29±0.13	27.88±1.48	755
Powerlaw: Γ = -2.09±0.92				
χ^2_ν= 0.99, ν=64				

TABLE 6.1. Paβ line fit parameters for the LUCI/LBT spectrum of NGC 4395. (1) Emission line component; (2) Central wavelenght of the emission line; (3) σ for the gaussian component; (4) Rest frame normalization; (5) Rest frame FWHM. *σ_λ fixed to [Fe II] line

---

[a] To consider unpredictable sistematic errors on the FWHM measures, we assume a common uncertainty of 10%

Then, following the NIR transitions listed in Landt et al. (2008) (see their Table 4), we added a Gaussian to measure the contamination of the [Fe II] λ12791 Å which is in blending with the Paβ (see Figure 6.2, right side). We added two Gaussians for the Paβ : a narrow, like the NLR, and one broad. The latter results to have FWHM$_{Rest}$= 786 km s^{-1} . After correction for the instrumental broadening it results a FWHM$_{Rest}$=755 km s^{-1} . We note that the broad component of the Paβ is blueshifted with respect to the narrow one of ~3 Å. The Fit parameters are shown in Table 6.1

6.3 2MASX J11+19

2MASX J11271632+1909198 is an optically classified Seyfert 1.8 galaxy (Véron-Cetty and Véron, 2010) at redshift z=0.1059, the higher of our sample. Its BH mass has been estimated using the stellar K-band from Two Micron All-Sky Survey (2MASS) photometry and it results to be log(M$_{BH}$)=9.00 M$_\odot$ (Winter et al., 2010).

6.3.1 2MASX J11+19: LUCI observations and lines fit

We observed 2MASX J11+19 on December 6, 2012, at the LBT with the LUCI NIR spectrograph in the zJ band using the grating 200 H+K and also in K band using the grating zJHK K filter. We used a $1''\times 2.8'$ wide slit corresponding to a $\sim$ 220 km s^{-1} spectral resolution for the zJ band and to a $\sim$ 87 km s^{-1} spectral resolution for th K band. The spectrum of 2MASX J11+19 was extracted with an aperture of $1.5''$ and the final J-band and K-band spectra are shown in Figure 6.3, left side, and 6.4, left side, respectively.

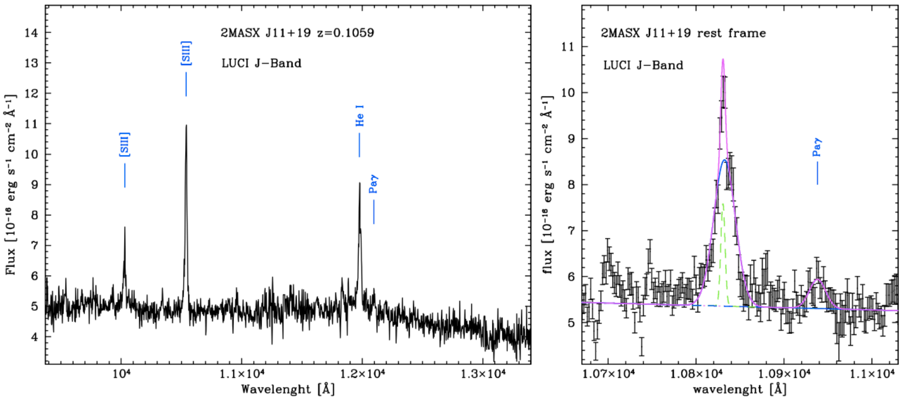

FIGURE 6.3. Left: Flux calibrated LUCI/LBT J-Band spectrum of 2MASX J11+19. Right: Rest frame, flux calibrated LUCI/LBT J-Band spectrum of 2MASX J11+19 in proximity of He I + Paγ emission lines. The green dashed line shows the narrow component of He I , the blue solid line is the broad component of He I . The magenta solid line shows the complete fit.

The LUCI/LBT J-band spectrum (Figure 6.3, left side) shows an intense He I emission line, well separated from a weaker Paγ line. The spectrum has been converted to the rest frame for the fitting procedure. We fitted the He I profile paying attention to disentagle the broad line from the narrow one. The continuum has been estimated with a power law, while the contribution from the NLR has been modelled with a Gaussian model that results to be center at λ_c= 11977.5 Åand a FWHM$_{Rest}$=145 km s^{-1} . We added a gaussians for the He I broad component, that results to have FWHM$_{Rest}$= 728 km s^{-1} at λ_c=11979.5 Å, redshifted of $\sim$2 Å respect the narrow line. We performed a line fit also for the Paγ , although it is very weak, we modelled it with one gaussian component of FWHM$_{Rest}$= 544 km s^{-1} and λ_c=12096.5 Å. We were

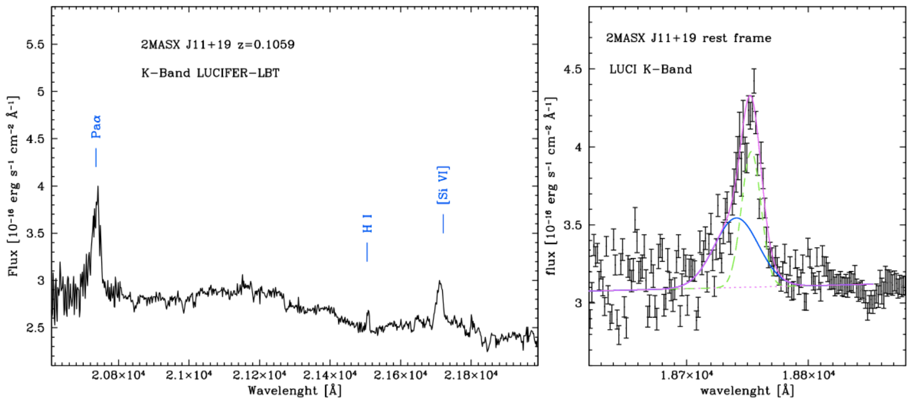

FIGURE 6.4. Left: Flux calibrated LUCI/LBT K-Band spectrum of 2MASX J11+19. Right: Rest frame, flux calibrated LUCI/LBT K-Band spectrum of 2MASX J11+19 in proximity of Paα emission line. The green dashed line shows the narrow component of Paα , the blue solid line is the broad component of Paα . The magenta solid line shows the complete fit.

not able to resolve the contribution of the NLR for the Paγ , but we noticed that its width is broader than the He I narrow line of ~400 km s^{-1} . The Fit

2MASX J11+19 He I +Paγ line fit

Component	$\lambda_{\mathbf{c}}$ [Å]	σ_λ [Å]	**Norm**$_{Rest}$ [$\times10^{-15}$]	**FWHM**$_{Rest}$^{a} [**km s**$^{-1}$]
(1)	**(2)**	**(3)**	**(4)**	**(5)**
He I Narrow	11977.5±0.4	2.7±0.6	1.3±0.6	145
He I Broad	11979.5±0.2	13.7±0.2	9.7±0.8	728
Paγ Broad	12096.5±2.0	10.3±0.3	1.4±0.5	544

Powerlaw: $\Gamma = 1.0\pm0.2$

$\chi^{\mathbf{2}}_{\nu}= 3.69$, ν=269

TABLE 6.2. He I +Paγ line fit parameters for the LUCI J-Band spectrum of 2MASX J11+19. (1) Emission line component; (2) Central wavelenght of the emission line; (3) σ for the gaussian component; (4) Rest frame normalization; (5) Rest frame FWHM.

---

[a] To consider unpredictable sistematic errors on the FWHM measures, we assume a common uncertainty of 10%

2MASX J11+19 Paα line fit				
Component (1)	$\lambda_{\mathbf{c}}$ [Å] (2)	σ_λ [Å] (3)	**Norm**$_{Rest}$ [$\times10^{-15}$] (4)	**FWHM**$_{Rest}$^{a} [**km s**$^{-1}$] (5)
Paα Narrow	20739.1±0.5	8.8±0.5	1.9±0.2	272
Paα Broad	20725.6±1.8	20.0±1.0	2.2±0.3	616
Powerlaw: Γ = -1.2±0.1				
$\chi^{\mathbf{2}}_\nu$= 2.28, ν=266				

Table 6.3. Paα line fit parameters for the LUCI K-Band spectrum of 2MASX J11+19. (1) Emission line component; (2) Central wavelenght of the emission line; (3) σ for the gaussian component; (4) Rest frame normalization; (5) Rest frame FWHM.

---

[a] To consider unpredictable sistematic errors on the FWHM measures, we assume a common uncertainty of 10%

parameters are shown in Table 6.2.

The LUCI/LBT K-band spectrum (Figure 6.4, left side) shows an intense Paα emission line. The spectrum has been converted to the rest frame for the fitting procedure. We fitted the Paα profile paying attention at disentagling the broad emission from the narrow one, though we did not have a reliable narrow forbidden line to use to constrain the NRL contribution. The continuum has been estimated with a power law, while the contribution from the Narrow Line Region (NLR) has been modelled with a Gaussian model that results to be center at λ_c= 20739.1 Å and with a FWHM$_{Rest}$=272 km s^{-1} . We have added a gaussian for the Paα broad component, that results to have FWHM$_{Rest}$= 616 km s^{-1} and center at λ_c=20725.6 Å, blueshifted of ~13 Å with respect to the narrow line. The Fit parameters are shown in Table 6.3.

6.4 MCG -05-23-16

6.4.1 MCG -05-23-16 in the literature

MCG -05-23-016 is an X-ray bright, nearby S0 galaxy (z=0.008486), optically classified as a Seyfert 1.9 galaxy (Veron et al., 1980). It is one of the the brightest Seyfert galaxies in the 2-10 keV band and it is also been detected in the hard X-ray above 20 keV with BeppoSAX/PDS (e.g Balestra et al. 2004), INTEGRAL/IBIS (Soldi et al., 2005) and Swift/BAT (Tueller et al. 2008, Tueller et al. 2010, Baumgartner et al. 2013). Its X-ray spectrum resembles a classical Compton-thin Seyfert 2 galaxy, with a column density $N_H \simeq 10^{22}\mathrm{cm}^{-2}$ (Balestra et al., 2004). The spectrum below 1 keV contains a combination of emission from scattered continuum photons and distant photoionized gas. Above 2 keV, the spectrum shows both the narrow and the broad iron Kα lines along with a strong Compton hump above 10 keV (Weaver et al. 1997, Mattson and Weaver 2004, Braito et al. 2006, Reeves et al. 2007).

This source hosts a comparably low-mass black hole, accreting at a high Eddington rate. The first estimate of the black hole mass of MCG -05-23-016 was made by Wandel and Mushotzky (1986) using the [O III] line width as a proxy for the stellar velocity dispertion in the relationship M$_{BH}$-σ, finding a black hole mass of M$_{BH}$=5×10^{7}M$_\odot$.

In a similar way Wang and Zhang (2007) obtained M$_{BH}$= 2×10^{6}M$_\odot$. They used the width of the [O III] line (Greene and Ho, 2005a) to obtain the black hole mass from the M$_{BH}$-σ relation (Tremaine et al., 2002) and give the error of the measurment with 0.7 dex. The low mass of the central black hole implies that the accretion onto the central engine take place at a high Eddington ratio ($L_{bol}/L_{Edd} \geq 0.4$). High accretion flows are the key element in order to understand the rapid growth of black holes in the early Universe and object like MCG -05-23-16 might indicate the early stages of supermassive black holes in which a strong accretion flow feeds the central engine (Beckmann et al., 2008).

6.4.2 MCG -05-23-16: ISAAC observations and lines fit

We have observed MCG -05-23-16 on January the 1th, 2012 at the VLT with the IR spectrograph ISAAC (mounted on the Nasmyth A focus of UT3 till the 12th December 2013) in the J band using both LR and MR instument modes. We used a 0.8" ×1.0" wide slit corresponding to a ∼ 430 km s^{-1} spectral resolution for the LR mode and to a ∼ 60 km s^{-1} spectral resolution for the MR modes. The spectrum of MCG -05-23-16 was extracted with an aperture of 0.6″ and in Figure 6.5 the LR and MR final spectra are shown.

The ISAAC/LR NIR spectrum of MCG -05-23-016 cleary shows broad components for Paβ and He I lines, even though the He I is blended with Paγ (see Figure 6.5, left side), there are no intense [Fe II] narrow emission lines. We observed the Paβ also with the MR mode to accurately perform the line fit, shown in Figure 6.5, right side. We fitted the Paβ profile paying attention to disentagle the broad component from the narrow one. Although the redshift of MCG -05-23-16 is quite low, the spectrum has been converted to the rest frame.
The continuum has been estimated with a power law, while the contribution from the NLR has been modelled with a Gaussian model, but it was not possible to fix its width to a NLR emission line, due to the lack of forbidden narrow emission lines in the spectrum. Following the NIR transitions listed in Landt et al. (2008) (see their Table 4), we have added a gaussian to measure the contamination of the [Fe II] λ12791Å which is in blending with the Paβ . We have added three gaussian for the Paβ : the narrow and two broad components. The narrow Paβ results to have a rest frame FWHM of 256 km s^{-1} and is centered at λ_c=12930.3 Å. The first broad component results to have a rest frame FWHM of 1049 km s^{-1} at λ_c= 12933.6 Å, redshifted of $\sim$ 3 Å with respect to the narrow one, while the second broad component have a rest frame FWHM of 3149 km s^{-1} and it is centered at λ_c=12921.8 $\AA$, blueshifted of $\sim$ 8 Å with respect to the narrow gaussian. In Table 6.4 the fit parameters are reported.

6.4.3 MCG -05-23-16: Xshooter observations and lines fit

We have observed MCG -05-23-16 on 11 February 2013 at the VLT with the multi-wavelength (3000−25000 Å) medium resolution spectrograph Xshooter (mounted on the UT3) that allowed us to obtain MCG -05-23-16 spectra in the UVB (3000−5595.0 Å), VIS (5595−10240 Å) and NIR (10240 −24800 Å) bands in a single observation. We used a 1.0”×11” wide slit for the UVB arm and a 0.9”×11” for the VIS and NIR arms, corresponding to a ∼60km s^{-1} spectral resolution. The spectrum of MCG -05-23-16 was extracted with an aperture of 1.5″. The UVB, VIS and NIR final spectra are shown in Figures 6.9, 6.8

ISAAC MCG -05-23-16 Paβ line fit				
Component	$\lambda_{\mathbf{c}}$ [**Å**]	σ_{λ} [**Å**]	**Norm**$_{Rest}$ [$\times 10^{-15}$]	**FWHM**$_{Rest}$[a] [**km s**$^{-1}$]
(1)	**(2)**	**(3)**	**(4)**	**(5)**
Paβ Narrow	12930.30±0.29	4.72±0.35	5.0±1.1	256
Paβ Broad	12933.60±0.59	19.36±10.70	38.6±4.0	1049
Paβ Broad	12921.8±1.1	58.08±1.83	74.9±3.9	3149
[Fe II] *	12901.5±1.2	7.08±0.94	2.49±1.28	385
[Fe II]	12784.0±1.2	7.01±0.94	1.70±0.56	385
Powerlaw: $\Gamma = 0.63\pm0.21$				
$\chi^{\mathbf{2}}_{\nu}$= 0.8, ν=333				

Table 6.4. Paβ line fit parameters for the ISAAC/MR spectrum of MCG -05-23-16. (1) Emission line component; (2) Central wavelenght of the emission line; (3) σ for the gaussian component; (4) Rest frame normalization; (5) Rest frame FWHM. *σ_{λ} fixed to [Fe II] line

---

[a] To consider unpredictable sistematic errors on the FWHM measures, we assume a common uncertainty of 10%

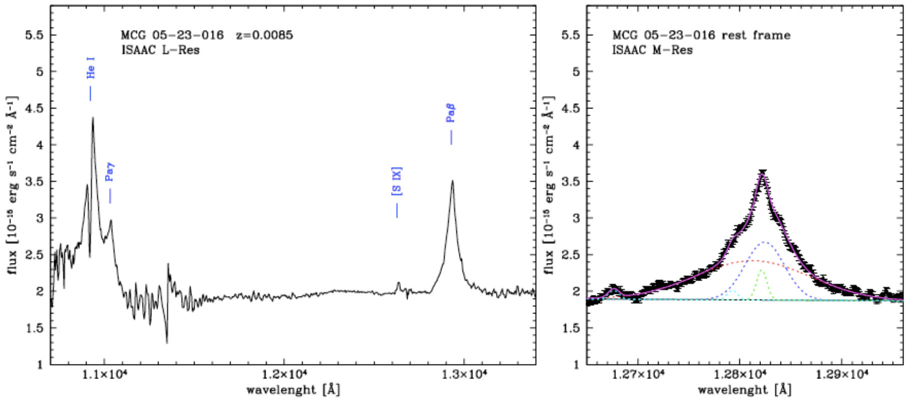

FIGURE 6.5. Left: low resolution NIR spectra of MCG -05-23-16 obtained with ISAAC/VLT. Right: medium resolution NIR ISAAC spectrum of MCG -05-23-16 and the fit of the Paβ emission line (magenta solid line). We identified three components for the Paβ: a narrow one (green dashed line), a broad component (blue dashed line) and another broad component (red dashed line). The cyano dashed line indicated the [Fe II] emission line in blend with the Paβ.

and 6.6, respectively.

The Xshooter NIR spectrum of MCG -05-23-016 shows broad components for Paβ and He I lines, but the He I is still blended with Paγ . In addiction there are also [S IX] and [Fe II] narrow lines (see Figure 6.6, left side).

We have fitted the Paβ profile disentagling the broad component from the narrow one. Although the redshift of MCG -05-23-16 is quite low, the spectrum has been converted to the rest frame. The continuum has been estimated with a power law, while the contribution from the NLR has been modelled as a Gaussian model with the line width fixed to the [S IX] narrow line. The Paβ line fit have been performed adding three gaussian components: the narrow Paβ results to have a rest frame FWHM=258 km s^{-1} and it is centered at λ_c=12927.9 Å, the first broad component results to have a rest frame FWHM=1496 km s^{-1} , centered at λ_c= 12925.6 Å, blueshifted of $\sim$ 2 Å with respect to the narrow one, while the second broad component have a rest frame FWHM=3976 km s^{-1} and it is centered λ_c=12901.2 *Å*, blueshifted of $\sim$ 27 Å with respect the narrow gaussian. Following the NIR transitions listed in Landt et al. (2008), Table 4, we have added a gaussian to measure the contamination of the [Fe II] λ12791Å which is known to be in blending with the Paβ , but its contribution to the line profile can be neglected. In Table

6.5 the fit parameters are shown.

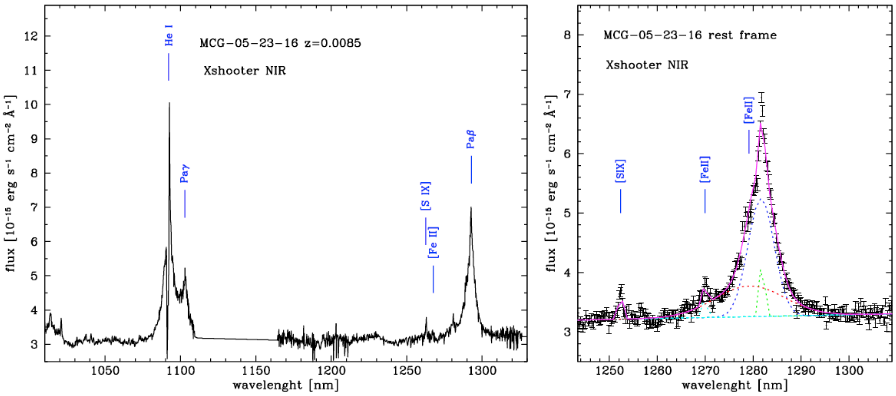

FIGURE 6.6. Left: NIR spectrum of MCG -05-23-16 obtained whith Xshooter at VLT. Right: Paβ line fit (solid magenta line). We identified three gaussian components for the Paβ : the narrow component is shown by the green dashed line, the first broad component is represented by the blue dashed line and the other broad component is the shown with the red dashed line.

Similary to the Paβ , we have been able to perfom the line fit also for He I and Paγ , shown in Figure 6.7. The continuum has been estimated with a powerlaw and the contribution from the NLR has been taken into account modelling the narrow components for both He I and Paγ with a gaussian profile whose width has been fixed to the [S IX] narrow line width. In this case we found only one broad component for each line.

The He I narrow line results in a FWHM$_{Rest}$=258 km s^{-1} and it is centered at λ_c=10927.5 Å, morever it shows an auto-absorption line, that we modelled with a gaussian of FWHM$_{Rest}$=258 km s^{-1} and λ_c=1091.50 Å. The broad component have a FWHM$_{rest}$ = 2341 km s^{-1} at λ_c=10922.1 Å, blueshifted of $\sim$ 5 Å with respect to the narrow emission line.

The Paγ narrow component shows a FWHM$_{Rest}$258 km s^{-1} , centered at λ_c = 11033.0 Å, while the broad one have a FWHM$_{Rest}$=1938 km s^{-1} at λ_c=11026.6 Å, blueshifted of ~6 Å with respect to the narrow one. In Table 6.6 the fitting parameters are shown.

Thanks to the capability of the multiwavelenght spectrograph Xshooter it has been possible to obtain also a medium resolution ($R = \frac{\lambda}{\Delta\lambda}$=7450) optical and UVB spectra of MCG -05-23-16 that allowed us to perform a line fit for the

Xshooter MCG -05-23-16 Paβ line fit				
Component	$\lambda_{\mathbf{c}}$ [**Å**]	σ_{λ} [**Å**]	**Norm**$_{Rest}$ [$\times 10^{-15}$]	**FWHM**$_{Rest}$^{a} [**km s**$^{-1}$]
(1)	**(2)**	**(3)**	**(4)**	**(5)**
Paβ Narrow *	12927.9±0.3	4.75±0.34	1.22±0.12	258
Paβ Broad	12925.6±0.6	27.60±0.82	12.79±0.59	1496
Paβ Broad	12901.2±4.5	73.24±4.53	8.85±0.66	3976
[S IX] *	12629.7±0.7	4.64±0.34	0.50±0.06	258
[Fe II] *	12673.6±2.1	4.65±0.34	0.16±0.05	258
[Fe II] *	12807.5±0.9	4.70±0.34	0.38±0.06	258
Powerlaw: Γ = -0.6±0.1				
$\chi^{\mathbf{2}}_{\nu}$= 1.4,ν=306				

TABLE 6.5. Paβ line fitting parameters for the Xshooter NIR spectrum of MCG -05-23-16. (1) Emission line component; (2) Central wavelenght of the emission line; (3) σ for the gaussian component; (4) Rest frame normalization; (5) Rest frame FWHM. *σ_{λ} fixed to [S IX] narrow line.

---

[a] To consider unpredictable sistematic errors on the FWHM measures, we assume a common uncertainty of 10%

Xshooter MCG -05-23-16 He I and Paγ line fit				
Component	$\lambda_{\mathbf{c}}$ [Å]	σ_λ [Å]	**Norm**$_{Rest}$ [$\times10^{-15}$]	**FWHM**$_{Rest}$^{a} [**km s**$^{-1}$]
(1)	**(2)**	**(3)**	**(4)**	**(5)**
He I Narrow *	10927.5±0.2	4.0±0.7	2.8±0.1	258
He I Abs *	10915.0±0.1	4.0±0.7	-2.99±0.07	258
He I Broad	10922.1 ±0.5	36.49±0.63	25.0±0.4	2341
Paγ Narrow*	11033.0±0.8	4.1±0.7	0.45±0.07	258
Paγ Broad	11026.6±1.0	30.52±1.14	10.4±0.4	1938
Powerlaw: Γ = 0.4±0.2				
$\chi^{\mathbf{2}}_\nu$ = 4.6, ν= 209				

TABLE 6.6. He I and Paγ line fit parameters for the Xshooter NIR spectrum of MCG -05-23-16. (1) Emission line component; (2) Central wavelenght of the emission line; (3) σ for the gaussian component; (4) Rest frame normalization; (5) Rest frame FWHM. *σ_λ fixed to [S IX] narrow line.

---

[a] To consider unpredictable sistematic errors on the FWHM measures, we assume a common uncertainty of 10%

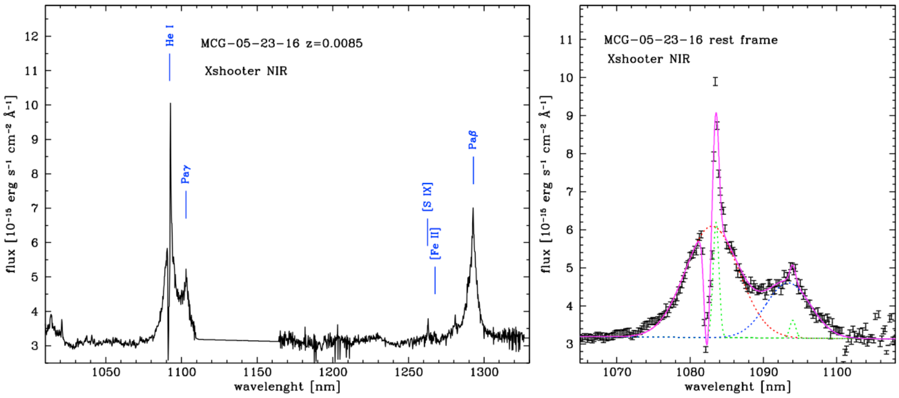

FIGURE 6.7. Left: NIR spectrum of MCG-05-23-16 obtained with Xshooter at VLT. Right: the line fit for He I and Paγ (magenta solid line). We identified two emission component for both lines: one narrow (green dashed lines), whose width is fixed to the [S IX] narrow line, and one broad (red dashed line and blue dashed line, respectively).

Hα and [N II] doublet emission lines, shown in Figure 6.8 and of the Hβ and [O III] doublet emission lines, shown in Figure 6.9.

In the optical spectrum we modeled the continuum with a power law and each [N II] lines with a narrow gaussian component with a FWHM$_{Rest}$=214 km s^{-1} centered at λ_c=6603.07 Å and λ_c=6638.69 Å, respectively. The Hα line has been modeled with two gaussian component: the narrow one, whose width has been fixed to the [N II] narrow line in order to take into account for the NLR contribution, results to be centered at λ_c= 6617.95 Å, while the broad component results to be centered at λ_c=6617.39 Å and has a FWHM$_{Rest}$ 2219 km s^{-1} , we noticed that it is blueshifted of $\sim$0.5 Å with respect to the narrow component. In Table 6.7 the fit parameters are shown.

The UVB spectrum does not show a broad Hβ . As we did for the optical spectrum, we modelled the continuum with a power law and we fitted the Hβ + [O III] doublet with a narrow gaussian component for each line. Tha width of all the narrow lines has been fixed to that of the [O III] , in order to carefully take into account for the NLR contibution. They result to have a FWHM$_{Rest}$=222 km s^{-1} , centered at λ_c= 4901.6 Å for Hβ , at λ_c=5000.3 Å and at λ_c= 5048.6 Å for the [O III] doublet. The fit parameters are shown in Table 6.8

Xshooter MCG -05-23-16 Hα and [N II] line fit				
Component	$\lambda_\mathbf{c}$ [Å]	σ_λ [Å]	**Norm**$_{Rest}$ [$\times 10^{-15}$]	**FWHM**$_{Rest}$[a] **[km s^{-1}]**
(1)	**(2)**	**(3)**	**(4)**	**(5)**
[N II]	6603.07±0.04	2.0±0.01	1.05±0.02	214
[N II] *	6638.69±0.01	2.0±0.01	3.45±0.02	214
Hα Narrow*	6617.95±0.01	2.0±0.01	4.02±0.02	214
Hα Broad	6617.39±0.02	20.96±0.13	7.27±0.02	2219
Powerlaw: Γ = -2.0±0.3				
χ^2_ν = 1.36, ν=889				

TABLE 6.7. Hα and [N II] line fit parameters for the Xshooter VIS spectrum of MCG -05-23-16.(1) Emission line component; (2) Central wavelenght of the emission line; (3) σ for the gaussian component; (4) Rest frame normalization; (5) Rest frame FWHM. *σ_λ fixed to [N II] narrow line.

---

[a] To consider unpredictable sistematic errors on the FWHM measures, we assume a common uncertainty of 10%

Xshooter MCG -05-23-16 Hβ and [O III] line fit				
Component	$\lambda_\mathbf{c}$ [Å]	σ_λ [Å]	**Norm**$_{Rest}$ [$\times 10^{-15}$]	**FWHM**$_{Rest}$[a] **[km s^{-1}]**
(1)	**(2)**	**(3)**	**(4)**	**(5)**
[O III]	5000.28±0.09	1.6±0.07	1.94±0.04	222
[O III] *	5048.56±0.08	1.6±0.07	5.58±0.05	222
Hβ Narrow*	4901.58±0.09	1.5±0.07	0.45±0.04	222
Powerlaw: Γ = -0.12 ±0.38				
χ^2_ν = 0.57, ν=990				

TABLE 6.8. Hβ and [O III] line fit parameters for the Xshooter UVB spectrum of MCG -05-23-16. (1) Emission line component; (2) Central wavelenght of the emission line; (3) σ for the gaussian component; (4) Rest frame normalization; (5) Rest frame FWHM. *σ_λ fixed to [O III] narrow line.

---

[a] To consider unpredictable sistematic errors on the FWHM measures, we assume a common uncertainty of 10%

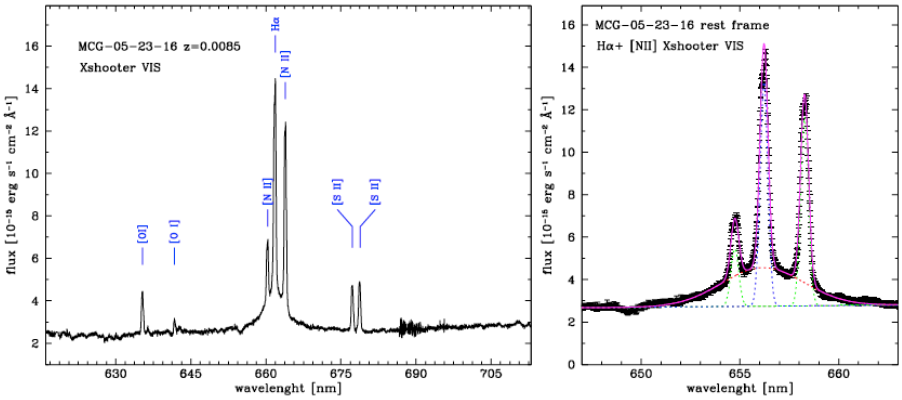

FIGURE 6.8. Left: Optical spectrum of MCG-05-23-16 obtained with Xshooter at VLT. Right: The Hα + [N II] line fit (magenta solid line). We fitted the Hα with two gaussian components: the narrow one represented by the green dashed line and the broad component (red dashed line).

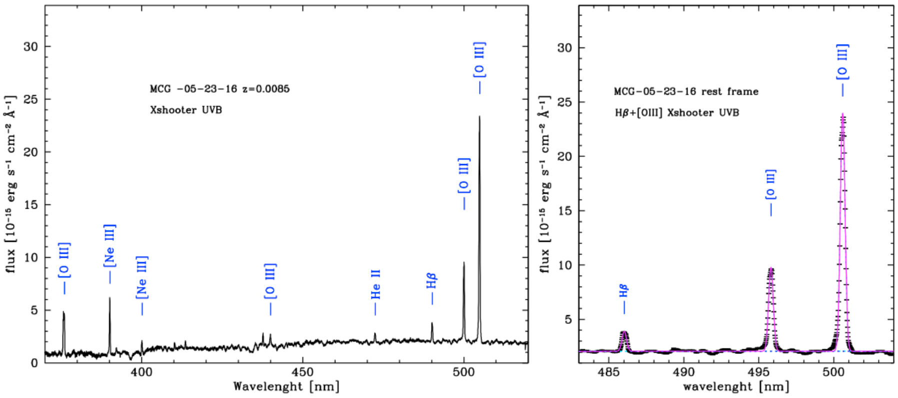

FIGURE 6.9. Left: UVB spectrum of MCG-05-23-26 obtained with Xshooter at VLT. Right: Fit of Hβ + [O III] lines (magenta solid line). No broad component has been obtained for the Hβ line and also for the [O III] doublet.

6.5 LEDA 093974

6.5.1 LEDA 093974 in the literature

LEDA 093974 is a nearby, FIR IRAS, S0 galaxy with a redshift z=0.0239, also classified like an emission-line spiral galaxy hosting a Seyfert 2 nucleous (Ho et al. 1993; Masetti et al. 2006 and references therein). This source is present in the 2nd IBIS survey (Bassani et al., 2005) and it is detected with fluxes of 2.9±07 mCrab and 5.9±1.1 mCrab in the 20-40 and 40-100 keV bands, respectively.

The optical spectrum of this galaxy shows a number of narrow emission features that can readily be identified with redshifted optical nebular lines. On the base of the presence of only narrow emission lines in the optical spectrum Masetti et al. (2006) suggested an activity typical of a NLR surrounding an obscured AGN, thus they optically confirmed the Sy2 classification. This was also supported by SUMSS radio detections andby the non detection in the soft x-ray band. Its X-ray luminosity in the 20-100 keV band of $L_{20-100keV}$=1.1×10^{44} erg s^{-1} places the source among the most luminous Type 2 Seyfert galaxies detected so far (Malizia et al., 1999).

6.5.2 LEDA 093974: Xshooter observations and lines fit

We have observed LEDA 093974 on April, 17th, 2013 at the VLT with Xshooter, thus we have obtained LEDA 093974 spectra in the UVB (3000−5595.0 Å), VIS (5595−10240 Å) and NIR (10240−24800 Å) bands in a single observation. The spectrum of LEDA 093974 was extracted with an aperture of 1.5″. The NIR, VIS and UVB final spectra are shown in Figures 6.10, 6.12 and 6.13, respectively.

The Xshooter NIR spectrum of LEDA 093974 shows an intense He i emission line, but it is on the edge of the telluric absorptions and the Paγ falls into this noisy band. Unfortunately, also the Paβ falls into the noise, thus it was very hard to perform a reliable fit on it. There are also two intense forbidden [Fe ii] emission lines, one of them is blended by the [S ix] line.

Despite its very noisy spectrum, we performed a fit for the Paβ . The continuum has been estimated with a power law, while the contribution from the NLR has been estimated from the gaussian narrow component of the intense [Fe ii] . It results to be centered at λ_c=1286.60 Å and it has a FWHM$_{Rest}$= 319 km s^{-1} . The [Fe ii] lines also show a broad component centered at λ_c=1285.97 Å and a FWHM$_{Rest}$=840 km s^{-1} . The [S ix] result to have only one narrow component centered at λ_c=1281.40 Å with a FWHM$_{Rest}$=319 km s^{-1} , fixed to the narrow [Fe ii] . We modelled the Paβ with a narrow gaussian, whose width has been tied to the narrow component of [Fe ii] , to take into account for the

NLR emission, the weak broad component result to be centered at λ_c=1309.73 Å and with a FWHM$_{Rest}$= 900 km s^{-1} but, since the [Fe II] λ12791 Å, in blending with Paβ , turned out to be at λ_c=1309.25 km s^{-1} , we think that this broad component came from the [Fe II] rather than hidrogen from the BLR. The fit parameters are shown in Table 6.9.

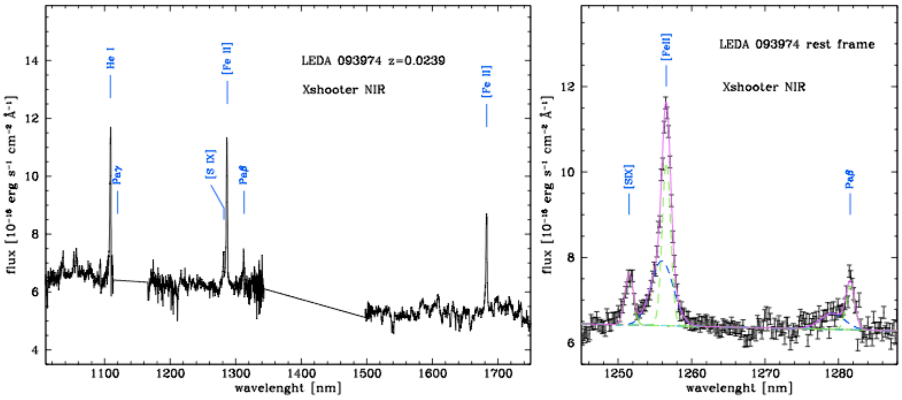

FIGURE 6.10. Left: Rest frame, flux calibrated Xshooter NIR spectrum of LEDA 093974. Right: Fit of Paβ + [Fe II] lines (magenta solid line). The green dashed lines show the narrow component of [Fe II] , [S IX] and Paβ lines, while the bue dashed line represent the broad components of both Paβ and [Fe II] .

The He I line is more intense than Paβ and it also shows a line broadening (see Figure 6.11). We modelled it with a narrow component with the width tied to the [Fe II] narrow line in order to accurately disentagle the broad emission from the narrow one. The narrow He I is centered at λ_c=1109.02 Å with a FWHM$_{Rest}$=319 km s^{-1} , while the broad component results to be centered at λ_c=1108.23 Å and has a FWHM$_{Rest}$=1107 km s^{-1} . The fit parameters are shown in Table 6.10.

The optical spectrum of LEDA 093974 shows an intense Hα + [N II] doublet, see Figure 6.12. In the fitting procedure the continuum has been modelled with a power law and we used the [N II] lines to estimate the NLR contribution to the line emission. Both the [N II] lines shows two components, the narrow ones are centered at λ_c= 6705.01 Å and λ_c=6741.18 Å, respectively, they have a FWHM$_{Rest}$=161 km s^{-1} . They also show two broad components centered at λ_c= 6702.37 Å and λ_c=6740.28, respectively, with a FWHM$_{Rest}$= 473 km s^{-1} . The Hα shows a symmetric, broad component in addiction to the narrow one.

Xshooter LEDA 093974 Paβ and [Fe II] line fit				
Component (1)	$\lambda_{\mathbf{c}}$ [Å] (2)	σ_λ [Å] (3)	**Norm**$_{Rest}$ [$\times 10^{-15}$] (4)	**FWHM**$_{Rest}$[a] [km s^{-1}] (5)
[S IX] *	1281.40±0.04	0.59±0.02	0.16±0.02	319
[Fe II] Narrow	1286.60±0.02	0.59±0.02	0.51±0.06	319
[Fe II] Broad	1285.97±0.09	1.54±0.08	0.54 ±0.07	840
[Fe II] *	1309.25±0.09	0.60±0.02	0.0±0.0	
Paβ Narrow*	1312.24±0.06	0.60±0.02	0.14±0.04	319
Paβ Broad	1309.73±0.4	1.7±0.6	0.14±0.06	900
Powerlaw: Γ = 0.75 ±0.18				
χ^2_ν = 1.52, ν=208				

Table 6.9. Paβ and [Fe II] line fit parameters for the Xshooter NIR spectrum of LEDA 093974. (1) Emission line component; (2) Central wavelenght of the emission line; (3) σ for the gaussian component; (4) Rest frame normalization; (5) Rest frame FWHM. *σ_λ fixed to [Fe II] narrow line.

---

[a] To consider unpredictable sistematic errors on the FWHM measures, we assume a common uncertainty of 10%

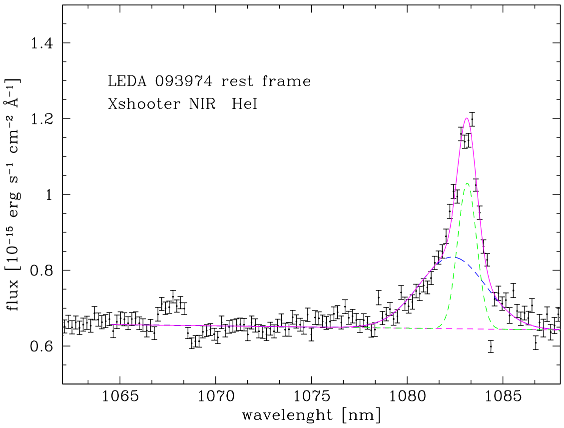

Figure 6.11. Fit of He i line (magenta solid line). The green dashed lines show the He i narrow component, while the bue dashed line represent the broad one.

The latter is centered at λ_c= 6719.85 Å and its width has been tied to the [N ii] narrow line, while the broad component has the center at λ_c=6720.20 Å and a FWHM$_{Rest}$=1742 km s^{-1} . The fit parameters are shown in Table 6.11.

The Xshoter UVB spectrum of LEDA 093974 shows an Hβ with no signature of a broad component, see Figure 6.13. Both the [O iii] lines have been

Xshooter LEDA 093974 He i line fit

Component	$\lambda_\mathbf{c}$ [Å]	σ_λ [Å]	**Norm**$_{Rest}$ [$\times 10^{-15}$]	**FWHM**$_{Rest}$[a] [**km s**$^{-1}$]
(1)	**(2)**	**(3)**	**(4)**	**(5)**
He i Narrow*	11090.2±0.2	5.1±0.2	0.45±0.03	319
He i Broad	11082.3±0.8	17.8±0.8	0.76±0.07	1107

Powerlaw: Γ = 1.00 ±0.56

χ^2_ν = 8.0, ν=97

Table 6.10. He i line fit parameters for the Xshooter NIR spectrum of LEDA 093974. (1) Emission line component; (2) Central wavelenght of the emission line; (3) σ for the gaussian component; (4) Rest frame normalization; (5) Rest frame FWHM. *σ_λ fixed to [Fe ii] narrow line.

---

[a] To consider unpredictable sistematic errors on the FWHM measures, we assume a common uncertainty of 10%

Xshooter LEDA 093974 Hα + [N II] line fit				
Component **(1)**	$\lambda_{\mathbf{c}}$ **[Å]** **(2)**	σ_λ **[Å]** **(3)**	**Norm**$_{Rest}$ $[\times 10^{-15}]$ **(4)**	**FWHM**$_{Rest}$[a] **[km s^{-1}]** **(5)**
[N II] Narrow	6705.01±0.03	1.56±0.01	0.26±0.01	161
[N II] Narrow*	6741.18±0.01	1.57±0.01	0.68±0.02	161
[N II] Broad	6702.37±0.1	4.59±0.04	0.29±0.02	473
[N II] Broad**	6740.28±0.05	4.62±0.04	1.69±0.03	473
Hα Narrow*	6719.85±0.01	1.57±0.01	0.53±0.01	161
Hα Broad	6720.20±0.01	16.96±0.01	2.79±0.05	1742
Powerlaw: $\Gamma = 3.80 \pm 0.14$				
$\chi^2_\nu = 3.4$, ν=834				

TABLE 6.11. Hα + [N II] line fit parameters for the Xshooter VIS spectrum of LEDA 093974. (1) Emission line component; (2) Central wavelenght of the emission line; (3) σ for the gaussian component; (4) Rest frame normalization; (5) Rest frame FWHM. *σ_λ fixed to [N II] narrow line; **σ_λ fixed to [N II] broad line.

---

[a] To consider unpredictable sistematic errors on the FWHM measures, we assume a common uncertainty of 10%

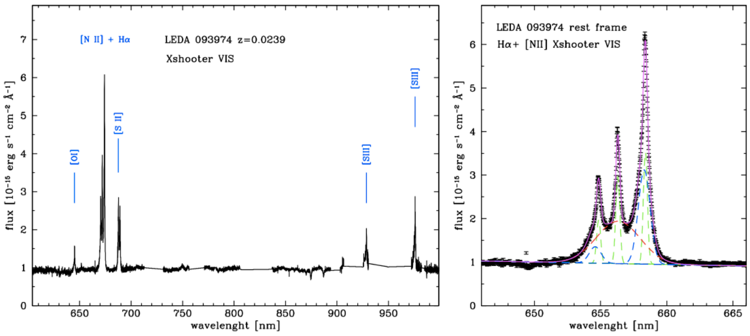

FIGURE 6.12. Left: Rest frame, flux calibrated Xshooter VIS spectrum of LEDA 093974. Right: Fit of Hα + [N II] lines (magenta solid line). The green dashed lines show the narrow component of Hα and [N II] doublet, the bue dashed line represent the broad components found in [N II] doublet, the red dashed line shows the broad Hα component.

modelled using two components. The narrow ones are centered at λ_c=5077.49 Å and λ_c=5126.43 Å with a FWHM$_{Rest}$= 162 km s^{-1} , in agreement with the FWHM found in the VIS spectrum for the NLR components of [N II] . The broad components are centered at λ_c=5074.28 Å and λ_c=512.357 Å , with a FWHM$_{Rest}$= 750 km s^{-1} . Confirming the intermediate classification of LEDA 093974, the Hβ does not show any broad component and it has been modelled with one narrow gaussian with the width fixed to the narrow [O III] and λ_c=4977.57 Å. The fit parameters are shown in Table 6.12.

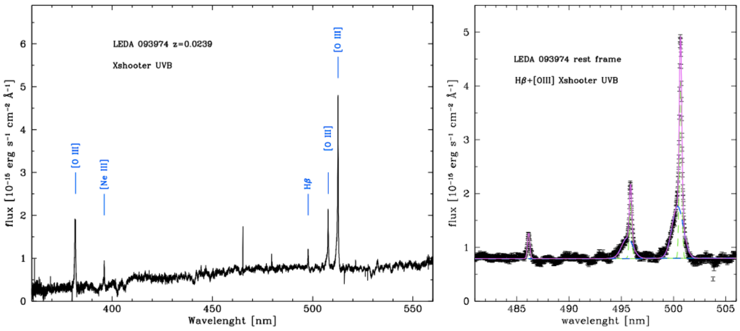

FIGURE 6.13. Left: rest frame, flux calibrated Xshooter UVB spectrum of LEDA 093974. Right: fit of Hβ + [O III] lines (magenta solid line). The green dashed lines show the narrow component of Hβ and [O III] doublet, the blue dashed line represent the broad components found in [O III] doublet.

Xshooter LEDA 093974 Hβ + [O III] line fit

Component	$\lambda_{\mathbf{c}}$	σ_λ	**Norm**$_{Rest}$	**FWHM**$_{Rest}$[a]
	[Å]	[Å]	[$\times 10^{-15}$]	[**km s**$^{-1}$]
(1)	**(2)**	**(3)**	**(4)**	**(5)**
[O III] Narrow	5077.49±0.007	1.193±0.007	0.188±0.006	162
[O III] Narrow*	5126.43±0.01	1.205±0.007	0.590±0.008	162
[O III] Broad	5074.28±0.13	5.51±0.05	0.32±0.02	750
[O III] Broad**	5123.57±0.06	5.57±0.05	0.80±0.02	750
Hβ Narrow*	4977.57±0.05	1.170±0.007	8.20±0.06	162

Powerlaw: Γ = -0.6 ±0.1

χ^2_ν = 2.18, ν=1236

TABLE 6.12. Hα + [N II] line fit parameters for the Xshooter UVB spectrum of LEDA 093974. (1) Emission line component; (2) Central wavelenght of the emission line; (3) σ for the gaussian component; (4) Rest frame normalization; (5) Rest frame FWHM. *σ_λ fixed to [O III] narrow line; *σ_λ fixed to [O III] broad line

---

[a] To consider unpredictable sistematic errors on the FWHM measures, we assume a common uncertainty of 10%

6.6 NGC 6221

6.6.1 NGC 6221 in the literature

NGC 6221 is a nearby, barred spiral SBc galaxy at redshift z=0.0050 located within a small galaxies group and it is known to exhibit clear signs of intense circumnuclear star formations (Boisson et al., 2002). Its peculiar morphology may be due to the interaction with NGC 6215. Koribalski and Dickey (2004) describe the presence of an HI gas bridge halfway between these two galaxies that may have fallen back to them. The unusual HI kinematics has been interpred by the authors as the result of a collision between NGC 6215 and the outer HI disc of NGC 6221 that is likely to have caused enhanced star formation in both galaxies and later, reaccreted HI gas with low angular momentum may sink towards the nuclear region, causing ongoing star formation in both galaxies and providing fuel for the active nucleus of NGC 6221. Moreover, the authors derive the dynamical mass of NGC 6221 and its SFR, that result to be $M_{tot}=8\times10^{10}$ $M_{\odot}$ and SFR=15 $M_{\odot}y^{-1}$, respectively.
NGC 6221 can be described as a X-ray-loud composite galaxy since its optical spectrum shows the typical feature of a sturbust galaxy and it has been classified as a Seyfert 2 galaxy on the base of [O III] /Hβ intensity ratio (Pence and Blackman (1984); Levenson et al. (2001)), while in the X-ray it appears similar to Seyfert 1 galaxies, exhbiting a power-law continuum, a broad Fe Kα line and continuum variability on timescales of days and years. An obscuring starburst, in which the interstellar gas and dust associated with the starburst conceal the active nucleous, can explain this peculiar features. Thus, it can be described in a Seyfert 2/starburst scenario, in which a faint AGN NLR is superposed on a dominant H II region powered by massive star. Moreover, in the optical nuclear spectrum the broad and blue component dominates the [OIII] profile, extending to more than 1000 Km/s, while in the Hβ the narrow component dominate (Levenson et al. (2001) and references therein). These optical features indicate that the intrinsic shape of the NLR is roughly conical, and its inclination allow us to see the object from the opening angle of a cone, that appears circular if projected onto the plane of the sky. This geometry implies that without the obscuring sturburst, NGC 6221 would be classified as a Syfert 1 galaxy (Levenson et al., 2001). The authors also presented HST images of the central region of NGC 6221 in the optical (F606W/WFPC2) and

in the NIR (F160W/NICMOS) and identified the bright central NIR source as the AGN (see Figure 6.14. At optical wavelengths, the nucleus is more diffuse and weaker than other bright knots, identified as star clusters, while in the NIR tha AGN nucleous arises. This make NGC 6221 an ideal candidate for our NIR analysis.

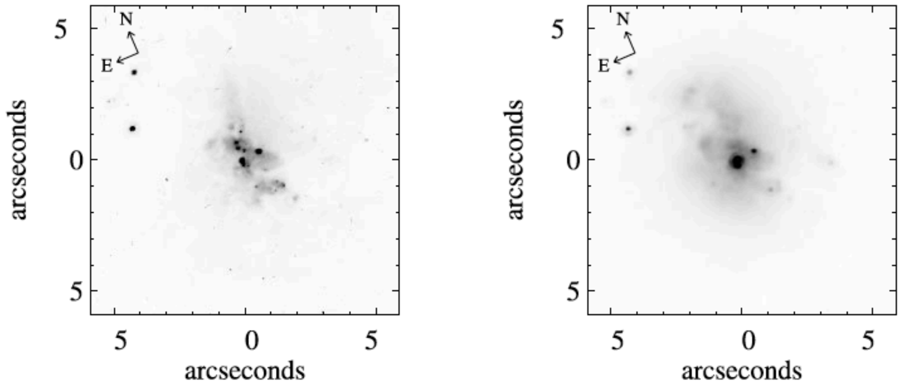

Figure 6.14. Images of NGC 6221 central region in the optical (left panel) and NIR (right panel). The brightest central source detected at 1.6 μm is the AGN and it is relatively week in the optical (Levenson et al., 2001).

6.6.2 NGC 6221: Xshooter observations and line fit

We have observed NGC 6221 on April, 24th, 2014 at the VLT with Xshooter. The final 2D spectrum was extracted with an aperture of 1.0$''$ and the NIR and VIS final spectra are shown in Figures 6.15 and 6.17, respectively.

The NIR spectrum of NGC 6221 shows a number of emission lines, like the intense forbidden [Fe II] , and several permitted emission lines (see Figure 6.15). In particular the He I is very intense and well separated from the Paγ , allowing us to perform the line fit on both the BLR lines. Moreover the Paγ has a very good S/N ratio and the presence of a clear [Fe II] narrow emission line allowed us to accurately model the NLR contribution for all the BLR emission lines.

To derive the [Fe II] profile we needed to add two gaussian components, the narrow one turns out to have its center at λ_c=12626.0 Å and a FWHM$_{Rest}$= 141 km s^{-1} and we use it as a constrain the narrow component of Paβ . The second component is broader than the first one, with a FWHM$_{Rest}$=481 km s^{-1} and it also is blueshifted of $\sim$ 6 Å with respect to the narrow one, having its center at λ_c=12619.8 Å. Surprisingly, also the Paβ line shows a similar profile, with a narrow component, tied in width to the [Fe II] ones and centered at λ_c= 12878.3 Å, and a broader gaussian centered at λ_c=12870.8 Å, thus blueshifted of $\sim$ 7 Å with respect to the narrow line. We have explained those two broad lines as a manifestation of a NLR outflow, thus we tied the width of Paβ outflows to the [Fe II] one. Finally, to accurately reproduce the complete Paβ profile we needed to add a third gaussian component that we can explain as a signature of the BLR gas under the gravitational influence of the nuclear BH. The latter has its center at λ_c=12877.6 Å and a FWHM$_{Rest}$=2257 km s^{-1} . We notice the it is redshifted of $\sim$7 Å with respect to the narrow component. We also add a gaussian component for the [S IX] and for the [Fe II] λ 12791 Å. See Figure 6.15, right side.

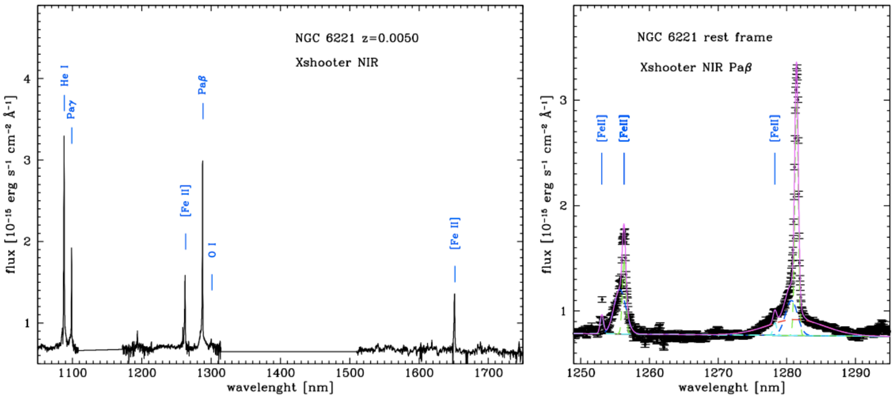

FIGURE 6.15. Left: flux calibrated NIR Xshooter spectrum of NGC 6221. Right: rest frame, flux calibrated NIR Xshooter spectrum of NGC 6221 in the proximity of Paβ and [Fe II] emission lines and the lines fit (magenta solid line). The narrow component of both line are shown with thw green dashed lines, the ouflow signatures with the blue dashed lines, while the broad component of Paβ is represented with the red dashed line.

We found a profile similar to the Paβ line also for the Paγ and He I emission lines (see Figure 6.16). Thus, the He I has been modelled adding three gaussian components: the narrow centered at λ_c=10881.2 Å, the outflow component with the center at λ_c= 10879.3 Å, blueshifted of $\sim$ 2 Å with respect to the previous component, and the broad one, centered at λ_c=10877.8 Å and with

Xshooter NGC 6221 Paβ and [Fe II] line fit

Component (1)	$\lambda_{\mathbf{c}}$ [Å] (2)	σ_λ [Å] (3)	**Norm**$_{Rest}$ [$\times 10^{-15}$] (4)	**FWHM**$_{Rest}$[a] [km s^{-1}] (5)
[S IX]	12593.5±0.9	2.5±0.02	0.09±0.01	140
[Fe II] Narrow	12626.00±0.05	2.54±0.02	0.41±0.02	141
[Fe II] Broad	12619.8±0.9	8.64±0.2	0.72 ±0.03	481
[Fe II] *	12846.6 ±0.3	2.58±0.02	0.07±0.01	141
Paβ Narrow*	12878.3±0.02	2.58±0.02	1.29±0.03	141
Paβ Broad**	12870.8±0.4	8.8±0.2	0.66±0.06	481
Paβ Broad	12877.6 ±1.1	41.4±1.7	1.4±0.1	2257

Powerlaw: $\Gamma = 0.98 \pm 0.18$

$\chi^2_\nu = 1.65$, ν=813

TABLE 6.13. Paβ and [Fe II] line fit parameters for the Xshooter NIR spectrum of NGC 6221. (1) Emission line component; (2) Central wavelenght of the emission line; (3) σ for the gaussian component; (4) Rest frame normalization; (5) Rest frame FWHM. *σ_λ fixed to [Fe II] narrow line; **σ_λ fixed to [Fe II] broad line.

---

[a] To consider unpredictable sistematic errors on the FWHM measures, we assume a common uncertainty of 10%

a FWHM$_{Rest}$= 1637 km s^{-1} . The narrow Paγ line is centered at λ_c=10989.6 Å, while the outflow one has the center at λ_c=10985.8 Å, blueshifted of $\sim$ 4 Å with respect to the narrow line. The widths of the two differents gaussians of each line, have been fixed each other to the corresponding components. Finally the BLR contribution to the Paγ results to be centered at λ_c=10976.0 Å and to have a a FWHM$_{Rest}$=1447 km s^{-1} . The fitting parameters are shown in Table 6.13, for the Paβ , and in Table 6.14 for He I and Paγ lines.
The optical spectrum shows a prominent and narrow Hα + [N II] doublet, comfirming the Seyfert 2 classification derived from previous optical spectroscopy observations. The VIS Xshooter spectrum is shown in Figure 6.17.

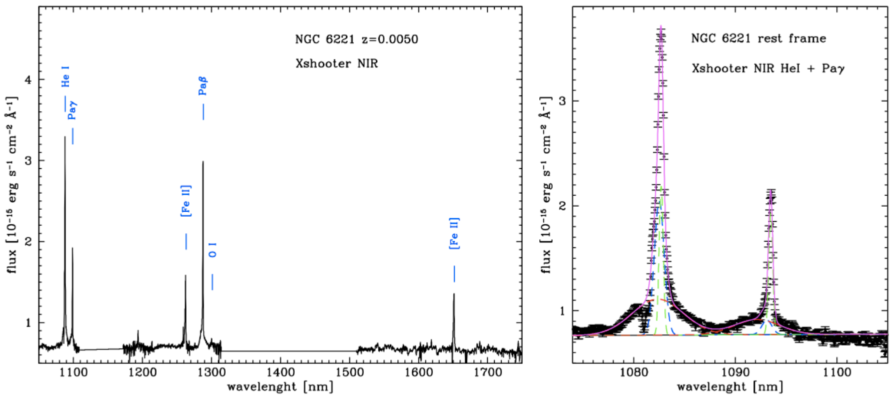

FIGURE 6.16. Left: flux calibrated NIR Xshooter spectrum of NGC 6221. Right: rest frame, flux calibrated NIR Xshooter spectrum of NGC 6221 in the proximity of Paγ and He I emission lines and the lines fit (magenta solid line). The narrow component of both line are shown with thw green dashed lines, the ouflow signatures with the blue dashed lines, while the broad components of Paγ and He I are represented with the red dashed lines.

6.7 NGC 7314

6.7.1 NGC 7314 in the literature

NGC 7314 is a barred spiral galaxy (SABb) at redshift z=0.0048, hosting a Seyfert 1.9 active nucleus (Zoghbi et al., 2013), confirmed by the the detection of a broad Hα in the HST spectrum. The X-ray behaviour of the source is extreme, with a strong variability on all observed timescales and it is thought

Xshooter NGC 6221 He I and Paγ line fit

Component (1)	$\lambda_{\mathbf{c}}$ [Å] (2)	σ_λ [Å] (3)	**Norm**$_{Rest}$ [$\times 10^{-15}$] (4)	**FWHM**$_{Rest}$[a] [**km s**$^{-1}$] (5)
He I Narrow	10881.2 ±0.03	2.05±0.03	0.65±0.05	132
He I Broad	10879.3±0.07	4.92±0.08	1.41±0.06	318
He I Broad	10877.8±0.4	25.33±0.55	1.95±0.07	1637
Paγ Narrow*	10989.6±0.03	2.07±0.03	0.54±0.03	132
Paγ Broad**	10985.8±0.8	4.98±0.08	0.15±0.04	318
Paγ Broad	10976.0 ±0.9	25.6±1.0	0.73±0.06	1447

Powerlaw: Γ = -0.63 ±0.14

χ^2_ν = 2.77, ν=648

Table 6.14. He I and Paγ line fit parameters for the Xshooter NIR spectrum of NGC 6221. (1) Emission line component; (2) Central wavelenght of the emission line; (3) σ for the gaussian component; (4) Rest frame normalization; (5) Rest frame FWHM. *σ_λ fixed to He I narrow line; **σ_λ fixed to He I broad line.

---

[a] To consider unpredictable sistematic errors on the FWHM measures, we assume a common uncertainty of 10%

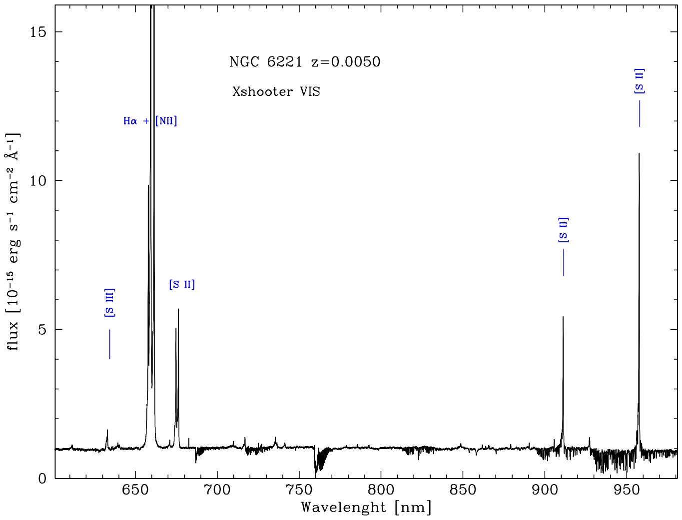

FIGURE 6.17. Flux calibrated VIS Xshooter spectrum of NGC 6221.

to be a type-2 counterpart to the NLS1 class (Dewangan and Griffiths, 2005). ASCA, Chandra and XMM observations showed that the iron Kα line at 6.4 keV may present both narrow and broad components that do not respond to the rapid variations of the continuum in the same way, in particular the narrow one respond slower respect to its wings, suggesting a different origins of the corresponding gas (Ebrero et al., 2011). In addiction, Zoghbi et al. (2013) report the discovery of X-ray reverberation for this galaxy, in particular the authors found a link between the iron K band an the emission in the Fe Kα band, likely due to a reflection process. Finally, Middleton et al. (2008) derived the BH mass using the stellar velocity dispersion resulting log(M_{BH})= 6.03 ±0.48 $M_\odot$.

6.7.2 NGC 7314 Xshooter observations and line fit

We have observed NGC 7314 on June, 25th 2014 at the VLT with Xshooter, in Section 4.4. The final 2D spectrum was extracted with an aperture of 1.0”. The NIR and VIS final spectra are shown in Figures 6.18 and 6.19, respectively.

The NGC 7314 NIR spectrum shows intense permitted emission lines, in particular He I and Paγ are prominent but in blending, thus we did not perform

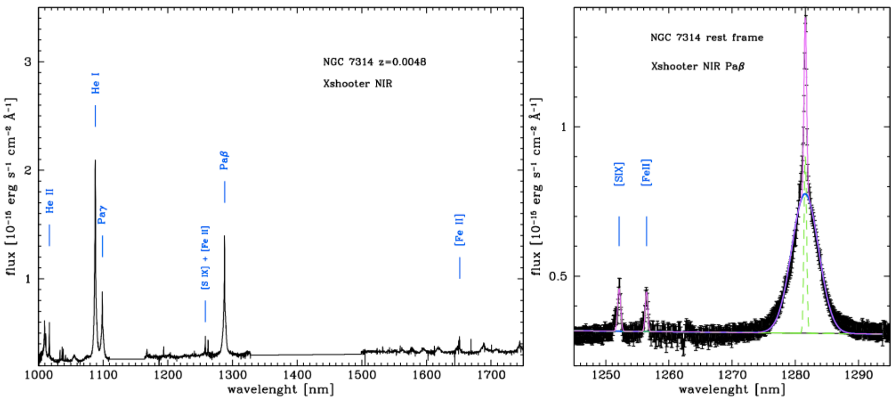

Figure 6.18. Left: flux calibrated Xshooter NIR spectrum of NGC 7314. Right: rest frame flux calibrated Xshooter NIR spectrum of NGC 7314 in proximity of Paβ line. The solid magenta line shows the total line fit. Green dashed lines represent the narrow components of Paβ , [Fe ii] and [S ix] lines, while the Paβ broad component is shown by the solid blue line.

the line fit althought they show signature of a broad component. The Paβ is at high S/N ratio and it is clearly shows a broad emission line superimposed the narrow one. The forbidden lines [S ix] and [Fe ii] are weak but it was possible to use the [Fe ii] line fit to constrain the NLR emission contamination of the Paβ .

We modelled the continuum with a power law and we fitted the [Fe ii] and [S ix] lines with only one narrow gaussian component. The [S ix] results to be centered at λ_c=12581.4 Å with a FWHM$_{Rest}$=136 km s^{-1} , while the [Fe ii] is centered at λ_c=12624.8 Å and has a FWHM$_{Rest}$=114 km s^{-1} . The latter is used to tie the narrow gaussian of the Paβ , tha results to be centered at at λ_c=12877.5 Å. Finally, we complete the Paβ line fitting adding the second broad gaussian component, that results to have the center at λ_c=12877.2 Å and a FWHM$_{Rest}$=1165 km s^{-1} .

6.8 NGC 2992

6.8.1 NGC 2992 in the literature

NGC 2992 is a nearby Sa galaxy at redshift z = 0.0077; it is highly inclined by about 70° to our line of sight and shows a broad disturbed lane of dust

Xshooter NGC 7314 Paβ line fit				
Component	$\lambda_{\mathbf{c}}$	σ_λ	**Norm**$_{Rest}$	**FWHM**$_{Rest}$[a]
	[Å]	**[Å]**	$[\times 10^{-15}]$	**[km s^{-1}]**
(1)	**(2)**	**(3)**	**(4)**	**(5)**
[S IX]	12581.4±0.2	2.43±0.25	0.08±0.01	136
[Fe II] Narrow	12624.8 ±0.2	2.04±0.05	0.07±0.01	114
Paβ Narrow*	12877.5±0.6	2.08±0.05	0.30±0.02	136
Paβ Broad	12877.2±0.2	21.3±0.3	2.46±0.06	1165
Powerlaw: Γ = 0.9 ±0.2				
χ^2_ν = 0.93, ν=986				

TABLE 6.15. Paβ line fit parameters for the Xshooter NIR spectrum of NGC 7314. (1) Emission line component; (2) Central wavelenght of the emission line; (3) σ for the gaussian component; (4) Rest frame normalization; (5) Rest frame FWHM. *σ_λ fixed to [Fe II] narrow line.

---

[a] To consider unpredictable sistematic errors on the FWHM measures, we assume a common uncertainty of 10%

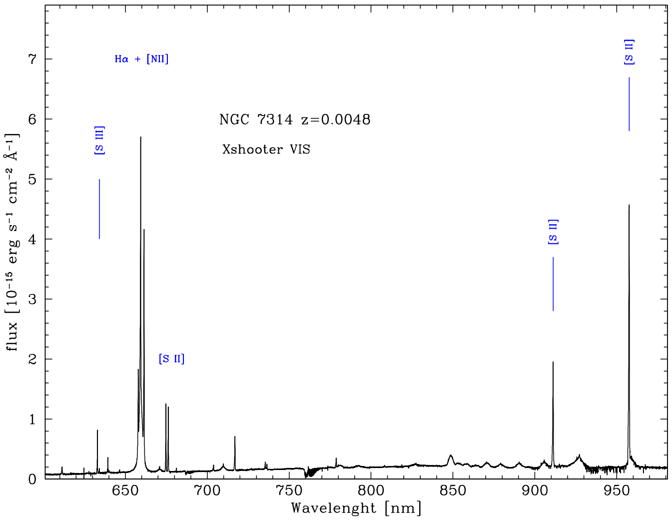

FIGURE 6.19. Flux calibrated VIS Xshooter spectrum of NGC 6221.

in its equatorial plane. Glass (1997) suggested that it is a hybrid between an intermediate Seyfert and a starburst galaxy, induced by the interaction with

NGC 2993 to the south. Both galaxies are connected by a tidal tail with a projected length of 2.9′. At a wavelength of 6 cm NGC 2992 shows prominent loop to the northwest and southeast of size of about 8”, designated as a *figure of 8.* From IR observations Chapman et al. (2000) concluded that this loops can be explained as an expanding gas bubbles, probably driven by the AGN, as pointed out from X-ray observations.
This object has been well studied in all wavelength regimes. It is optically classified as Seyfert 1.9, but its type classification has been observed to vary conspicously in the past, leading to classifications ranging to Seyfert 2 to Seyfert 1.9 on the basis of a broad Hα with no corresponding Hβ component in its nuclear spectrum (Ward et al., 1980), suggesting the existence of an obscured BLR. This was confirmed later also in the infrared (Rix et al. 1990, Goodrich et al. 1994, Veilleux et al. 1997).
Long-slit observations have demonstrated the complex kinematics of the ionized gas in its circumnuclear region (Heckman et al. 1981, Colina et al. 1987, Marquez et al. 1998). The double peaked line profiles and asymetries observed in [O III] and Hα lines from (Marquez et al., 1998), can be accounted for an outflow within a biconical envelope on kilo-parsec scales, probably driven by the AGN, rather than the starburst (Friedrich et al., 2010). Allen et al. (1999) found that one component of the double peaked lines follows the galactic rotation curve, while the other is identified as a wind that is expanding out of the plane of the galaxy with a velocity up to 200km s^{-1} . Moreover, Gilli et al. (2000) correlated the presence (or the absence) of the broad component of Hα with the galaxy’s X-ray flux and postulated that the observed optical spectra variations were due to different phases of rebuilding of the central accretion disk (Trippe et al., 2008). He reported the broad component Hα varing from FWHM $\simeq$2600 Km/s to FWHM $\simeq$ 2000 Km/s (see Figure: 6.20). A recent optical spectrum, taken also by Jones et al. (2009) in 2009 is shown in Figure 6.21, here the Hβ does not show a clear broad component, while the Hα is similar to that reported in Gilli et al. (2000) work.

The X-ray flux and spectrum were observe to vary along 16 years of observations, performed with different satellites. The 2-10 keV flux was observed to decrease by a factor of ~20 from the HEAO-1 observations in the 1978 to the ASCA observations in the 1994, were it reach its minimum value. A similar decrease was also observed in the soft X-ray. These spectral variations

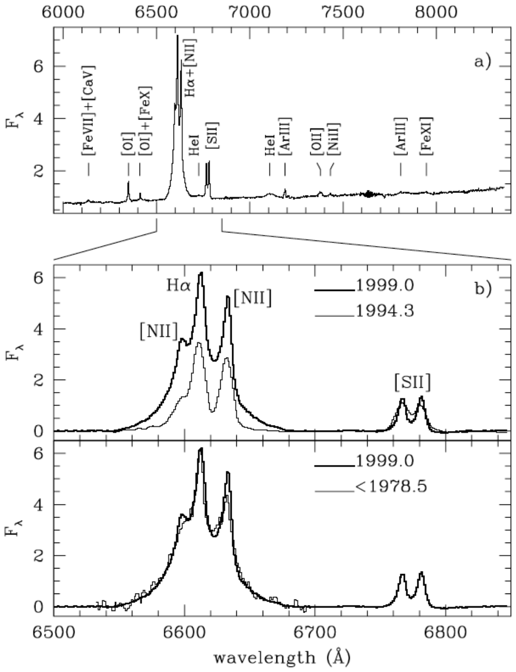

FIGURE 6.20. Top: optical spectrum of NGC2992 obtained by Gilli et al. (2000) in 1999. Middle: comparison between Gilli et al. (2000) spectrum and that obtained by Allen et al. (1999) in 1994, i.e. at the minimum of X-ray activity. Bottom: comparison with the spectrum obtained by Veron et al. (1980) prior to 1978, i.e. when the nucleous was in an high X-ray state.

were interpreted as an evidence for for radiation reprocessed by the molecular, obscurbing torus (Gilli et al. (2000) and references therein). Moreover, Glass (1997) reported infrared flux variability and remarked the fading of the central source in the time range 1978-1996. All these evidences suggest that the AGN in the center of NGC 2992 was turning off. However, BeppoSAX observations in 1997 shown that the AGN was come back to the previous high level of activity observed in the 1978, given the indications of a revieved AGN (Gilli et al., 2000).

6.8.2 NGC 2992 ISAAC observations and line fit.

We have observed NGC 2992 on January 7th, 2012 with ISAAC at VLT. The spectrum of NGC 2992 was extracted with an aperture of 0.9″ and the final, flux calibrated LR and MR spectra are shown in Figure 6.22.

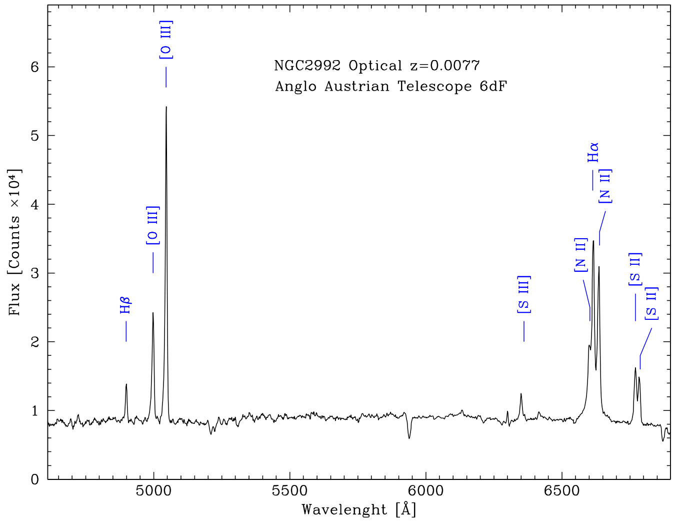

FIGURE 6.21. Optical spectrum of NGC2992 from Jones et al. (2009)

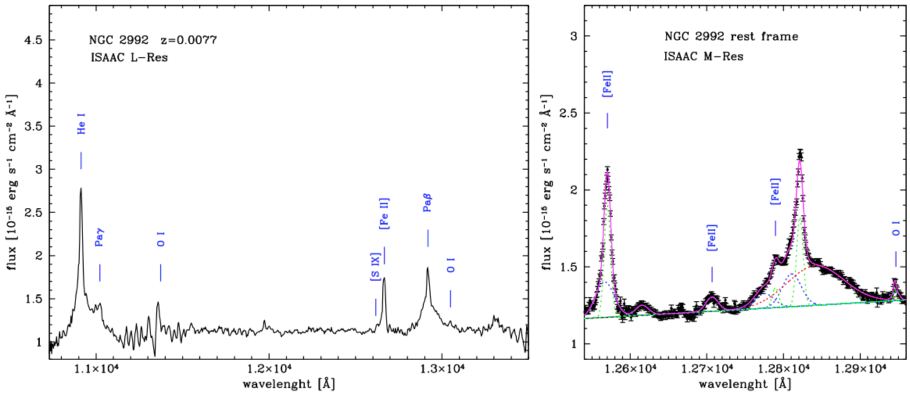

FIGURE 6.22. Left: flux calibrated, low resolution NIR spectra of NGC 2992 obtained with ISAAC/VLT. Right: flux calibrated medium resolution NIR ISAAC spectrum of NGC 2992 and the fit of the Paβ + [Fe II] emission line (magenta solid line). We identified two component for the [Fe II] λ12570 Å: a narrow emission line (green dashed line) and an outflow signature (blue dashed line). The same two component are found also in the [Fe II] λ12791 Åin blend with the Paβ : the narrow (green dashed line) and the broad one (blue dashed line). The Paβ line shows three component: the narrow one (green dashed line) , the outflow (blue dashed line) and the broad component (red dashed line).

The ISAAC/LR NIR spectrum of NGC2992 cleary shows broad components both in He I + Paγ lines (even thought they are not well resolved) and

in the Paβ line (Figure: 6.22, left side), it also shows a prominent [Fe II] narrow line. We observe the Paβ also in the MR mode to acurately perform the line fit, shown in Figure 6.22, right side. Although the redshift of NGC 2992 is quite low, the spectrum has been converted to the rest frame. The continuum as been estimated with a power law, while the NLR contribution has been modelled whith a gaussian component from the [Fe II] line fit. In this case the [Fe II] shows two different components: a narrow one centered at λ_c= 12667.0 Å with a rest frame FWHM= 236 km s^{-1} , that we identified as a NLR contribution, and a broad one at center λ_c=12663.5, blueshifted of 3.5 Å respect to the narrow line, with the rest frame FWHM=679 km s^{-1} . We interpreted the latter as an indication of the NLR ouflow, that has been well studied in the literature of NCG 2992 (Friedrich et al. (2010) and references therein).
Following the the NIR transitions listed in Landt et al. (2008) Table 4, we have added a gaussian model to take into account for the [Fe II] λ12791 Å in blending with the Paβ . It turned out to have an second broad component that we intetpred again as the NLR ouflow signature. Thus we fitted it using a narrow gaussian centered at λ_c=12888.0 Å with a rest frame FWHM= 236 km s^{-1} , tied to the narrow [Fe II] λ12570 Å width. The ouflow component result to be centered at λ_c= 12873.70 Å and to have a rest frame FWHM=679 km s^{-1} , tied to the width of the [Fe II] λ12570 Å outflow component. We notice that it is redshifted of $\sim$ 14 Å with respect to the narrow line.
The NLR outflow signature is also observed in the Paβ line, but we have been able to accurately separate it both from the narrow and the broad components. Therefore we performed the line fit using three gaussian models: the narrow one, that results to have its center at λ_c= 12920.10 Å and a FWHM=236 km s^{-1} , tied to the [Fe II] narrow component width. The ouflows signature is centered at λ_c=12909.40 Åand it has a rest frame FWHM=679 km s^{-1} , blueshifted of $\sim$10 Å with respect to the narrow line and it has been tied to the [Fe II] outflow width. Finally, the broad component of Paβ results to have its center at λ_c=12940.50 Å with a rest frame FWHM=2019 km s^{-1} and it is blueshifted of $\sim$20 Å with respect to the narrow line. In Table 6.16 we show the fit parameters.
Despite the presence of the spectroscopic signatures of the well known outflow in our NGC 2992 NIR spectra, we explain the Paβ broad component as an evidence for the BLR gas under the influence of the central BH. Indeed

this third component is not present in the [Fe II] λ12570 Å, while the ouflows signatures are seen in almost all emission lines and they are also blushifted respect to their narrow lines. Moreover we extracted all our nuclear spectra at $\sim$1.0$''$ that correspond to the very central region of the AGN, as shown from the velocity field maps of Friedrich et al. (2010), in Figure 6.23.

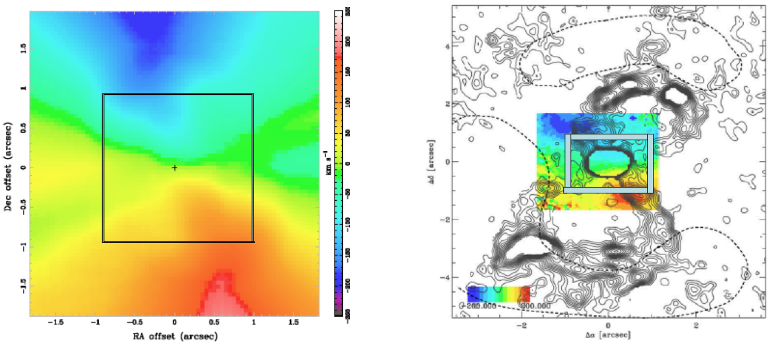

FIGURE 6.23. Left: calculated velocity field in the central region of NGC 2992 resulting from two inclined disks and conical outflows. Right: Velocity map of H2 with the contours of radio flux at 8.46 GHz. (Friedrich et al., 2010). In both figures the cyano squares indicate the 1 acrsec square of our measurements. Nord is up, east to the left.

ISAAC/MR NGC 2992 Paβ line fit				
Component	$\lambda_{\mathbf{c}}$ [Å]	σ_λ [Å]	**Norm**$_{Rest}$ [$\times 10^{-15}$]	**FWHM**$_{Rest}$^{a} [**km s**$^{-1}$]
(1)	**(2)**	**(3)**	**(4)**	**(5)**
[Fe II] Narrow	12667.00±0.07	4.26±0.07	7.4±0.4	236
[Fe II] Broad	12663.50±0.40	12.27±0.07	6.8±0.5	679
[Fe II] Narrow	12804.60±0.54	8.06±0.60	1.8±0.3	442
[Fe II] Bl Narrow *	12888.00±0.40	4.34±0.07	1.3±0.2	236
[Fe II] Bl Broad **	12873.70±1.03	12.47±0.07	2.8±0.7	679
Paβ Narrow *	12920.10±0.09	4.34±0.07	6.0±0.4	236
Paβ Broad**	12909.40±0.80	12.50±0.07	6.4±1.2	679
Paβ Broad	12940.50±1.90	37.26±1.38	23.1±2.4	2019
O I	13046.50±1.30	4.22±1.31	0.6±0.3	227
Powerlaw: Γ = -3.0 fixed				
χ^2_ν= 1.24,ν= 397				

TABLE 6.16. Paβ and [Fe II] line fitting parameters for our ISAAC/MR spectrum of NGC 2992. (1) Emission line component; (2) Central wavelenght of the emission line; (3) σ for the gaussian component; (4) Rest frame normalization; (5) Rest frame FWHM. *σ_λ fixed to [Fe II] narrow line; **σ_λ fixed to [Fe II] broad component.

---

[a] To consider unpredictable sistematic errors on the FWHM measures, we assume a common uncertainty of 10%

6.9 NGC 1365

6.9.1 NGC 1365 in the literature

NGC 1365 is a nearby (z=0.0055) and very well studied SB Seyfert 1.9 galaxy (Trippe et al., 2010), hosting a $\simeq 2\times10^6 M\odot$ BH (see Kaspi et al. 2005, Schulz et al. 1999) which displays a large amount of X-ray spectral variability on time-scales of hours to years and evidence for a relativistically broadened iron line (Risaliti et al. 2009, Walton et al. 2010, Brenneman et al. 2013) indicative of a rapidly rotating black hole, confermed also by (Risaliti et al., 2013). It has been studied exstensively in the X-ray band and it has been observed to display complex and variable absorption, with rapid variations in column density (N_H ranging from $\sim$ (10-27) $\times 10^{22}$cm^{-2} (Risaliti et al. 2005, Risaliti et al. 2007, Maiolino et al. 2010) attributed to an occultation event originated in the BLR clouds. These variations have been interpreted as the spectrum changing from being transmission dominated, in which the absorbing material is Compton thin, to reflection dominated, in which the absorbing material is compton thick.
It shows a large number of absorption and emission lines, such as a strong Fe fluorescence emission line and Fe absorpion lines between 6.7 and 8.3 keV, attributed to Fe XXV , Fe XXVI , Kα and Kβ transitions. The measured velocities of these lines have been explained as an indication of an highly ionized, high velocity ouflow from NGC 1365 (Risaliti et al., 2005). Connolly et al. (2014) performed a long term Swift X-ray observations of NGC 1365 over a period of six years finding a large amount of spectral variability, explained in terms of a wind model in which the launch radius varies as a function of ionizing flux and disc temperature and therefore moves out with increasing accretion rate, i.e. increasing X-ray luminosity. Thus, depending on the inclination angle of the disc relative to the observer, the absorbing column may decrease as the accretion rate goes up. Moreover, from time-resolved spectroscopy performed on the NuSTAR and XMM-Newton observations, Risaliti et al. (2013) found a good correlation between the strength of the relativistic iron line and the Compton reflection hump relative to the intrinsic continuum. These observations allow the authors to confirm that NGC 1365 hosts a rapidly rotating BH.

In the optical spectra of NGC 1365 there is some evidence of variability: Veron et al. (1980) classified it as a Seyfert 1.5 on the basis of a strong Hα detected in its nucleo. Moreover, from medium resolution long slit optical spectroscopy of NGC 1365, Schulz et al. (1994) comments on the conspicuous broad component of Hα observed in 1988 October, and in Schulz et al. (1999) the authors shows an Hβ with a substantial broad component (Figure 6.24), with a FWHM= 1895 km s^{-1} . However, Trippe et al. (2010) found an extremely faint broad-line component in Hα in their spectra, obtained in the 2009 (Figure 6.25 and Figure 6.26 from Jones et al. (2009)) and they also found a narrow Hβ that appears to be enhanced with respect to the [O III] lines, indicating a very strong starburst emission component. Thus they classified NGC 1365 as a Seyfert 1.9 plus a starburst component.

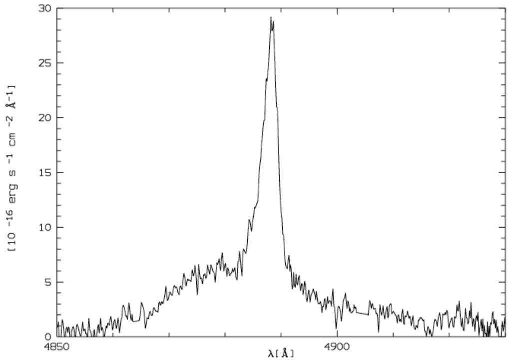

FIGURE 6.24. Hβ from the nucleus of NGC1365 obtained by Schulz et al. (1999).

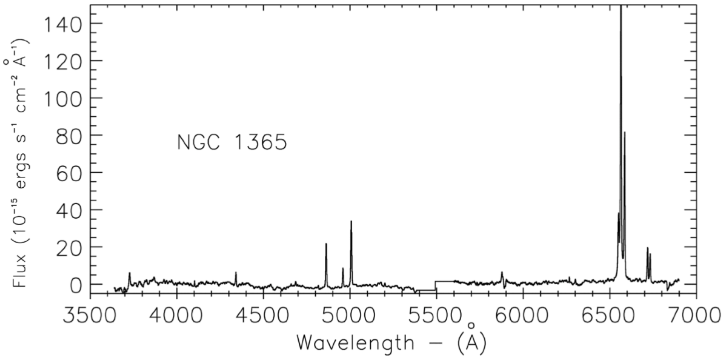

FIGURE 6.25. Optical spectrum of NGC1365 from Trippe et al. (2010).

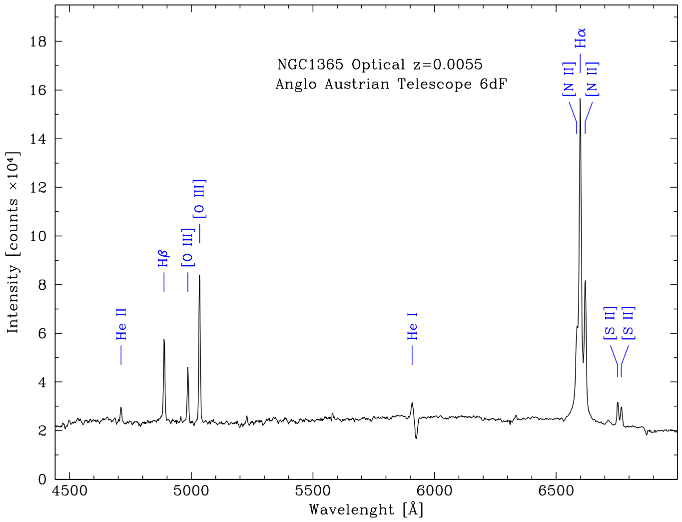

FIGURE 6.26. Optical spectrum of NGC1365 from Jones et al. (2009)

6.9.2 NGC 1365 ISAAC observations and line fit.

We have observed NGC 1365 on October 13th, 2011 with ISAAC at VLT. The spectrum of NGC 1365 was extracted with an aperture of 0.6″ and the final, flux calibrated LR and MR spectra are shown in Figure 6.27, left and right side respectively.

The ISAAC/LR NIR spectrum of NGC1365 appears rich of permitted emission lines, in particular there are intense He I , Paγ (well separated) and Paβ lines but there is no evidence of the [Fe II] λ12570 Å (Figure: 6.27, left side).
We have observed the Paβ also in the MR mode to accurately perform the line fit, shown in Figure 6.27, right side. Although the redshift of NGC 1365 is quite low, the spectrum has been converted to the rest frame. The continuum as been estimated with a power law, while there are no NLR emission lines to be used to constrain the model for this component. We identified in the Paβ lines three components. The narrow line has been modelled with a gaussian profile centered at λ_c=12889.2 Å and having a FWHM$_{Rest}$=422 km s^{-1} . The first broad component results to be centered at λ_c=12883.7 Å and to have a FWHM$_{Rest}$=1056 km s^{-1} , it is blueshifted of $\sim$ 5 Å with respect to the narrow line. The second broad component has its center at λ_c= 12895.9 Å and a FWHM$_{Rest}$=3248 km s^{-1} , we notice that it is redshifted of $\sim$ 12 Å with

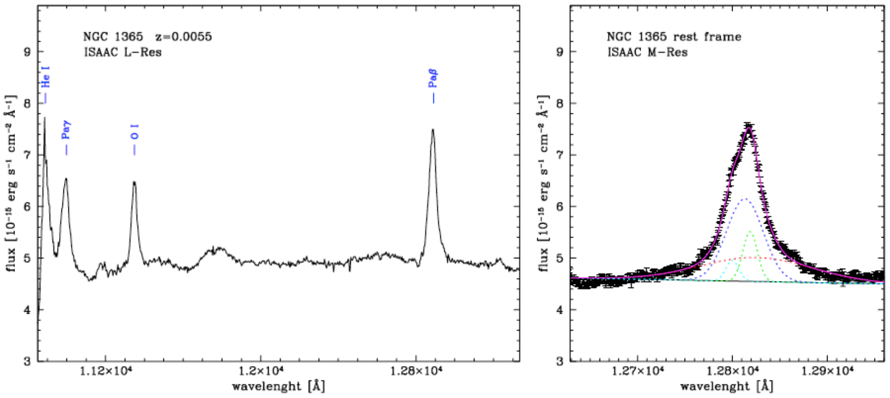

FIGURE 6.27. Left: flux calibrated, LR NIR spectra of NGC 1365 obtained with ISAAC/VLT. Right: flux calibrated MR NIR ISAAC spectrum of NGC 1365 and the fit of the Paβ emission line (magenta solid line). The Paβ line has been modelled with three gaussian component: the narrow one is shown with the green dashed line, the first broad component with the blue dashed line and the second broad component is shown with the red dashed line. The [Fe II] λ12791 in blend with Paβ has been also take into account (green dashed line).

respect to the narrow line. Following the the NIR transitions listed in Landt et al. (2008) Table 4, we have added a gaussian model to take into account for the [Fe II] λ12791 Å in blending with the Paβ and it turned out to be centered at λ_c=12870.4 Å and to have a FWHM$_{Rest}$=370 km s^{-1} , in agrrement with the value found for the narrow component of Paβ . The fit parameters of NGC 1365 are shown in Table 6.17.

6.10 Mrk 1210 - Phoenix galaxy

6.10.1 Mrk 1210 in the literature

Mrk 1210, also known as Phoenix Galaxy, is a nearby (z=0.0135) Sa galaxy. It is an outstanding Seyfert 2 because it shows signatures of recent circumnuclear star formation and an high level of X-ray activity. Moreover it shows warm far infrared color and a spectral energy distribution peaking near 60 μm. The latter characteristics made it a member of the sample of galaxies called 60 μm peakers (60PKs, Heisler and De Robertis 1999) and many evidences have been accumulated over the years, indicating that these properties can be attributed

ISAAC/MR NGC 1365 Paβ line fit				
Component (1)	$\lambda_{\mathbf{c}}$ [Å] **(2)**	σ_λ [Å] **(3)**	**Norm**$_{Rest}$ [$\times 10^{-15}$] **(4)**	**FWHM**$_{Rest}$^{a} [**km s**$^{-1}$] **(5)**
[Fe II]	12870.4 ±0.8	6.78±0.83	6.7±4.2	370
Paβ Narrow	12889.2±0.4	7.74±0.57	18.4±7.6	422
Paβ Broad	12883.7 ±0.3	19.36±12.6	76.5±8.8	1056
Paβ Broad	12895.9±1.6	59.6±1.9	68.4±3.9	3248
Powerlaw: Γ = 1.00 ±0.06				
χ^2_ν= 1.72, ν= 675				

Table 6.17. Paβ line fitting parameters for our ISAAC/MR spectrum of NGC 1365. (1) Emission line component; (2) Central wavelenght of the emission line; (3) σ for the gaussian component; (4) Rest frame normalization; (5) Rest frame FWHM.

---

[a] To consider unpredictable sistematic errors on the FWHM measures, we assume a common uncertainty of 10%

to a dust obscured active galactic nucleus (Keel et al. 1994, Hes et al. 1995). Mrk 1210 has been extensively studied in the optical region, not only because of the Wolf-Rayet features found within the central 200 pc (Storchi-Bergmann et al., 1998), indicating the presence of a circumnuclear starburst, but also for the detection of broad Hα and Hβ components in polarized light (Tran et al. 1992, Tran 1995) with FWHM$\simeq$2380 km s^{-1} . Moreover, in the near infrared, the degree of polarization of Mrk 1210 rises toward longer wavelengths (Watanabe et al., 2003) and observational evidence suggests that this polarization is due to dichroic absorption by aligned grains.

Near infrared spectra reported by Veilleux et al. (1997) show a Paβ profile characterized by a strong narrow component on top of a broad base with FWHM $\simeq$ 1600 km s^{-1} , suggesting the presence of a hidden broad-line region (BLR). However, Mazzalay and Rodríguez-Ardila (2007) performed a spectrosopical study both on Optical and NIR spectra. The authors fonud broad components of similar shape both in permitted (Hβ and Paβ) and in forbidden ([O III] and [Fe II]) emission lines. Moreover, a comparison with the [Fe II] λ=12570 Å profile, indicates that at least a part of the broad emission is also present in the

forbidden [Fe ii] line, suggesting that the broad permitted line is not produced in a genuine high-density BLR. In Figure 6.10.1 the optical spectra taken by Mazzalay and Rodríguez-Ardila (2007) are shown.
In X-rays band Mrk 1210 is one of the very few cases of an AGN in transition between a Compton thick, reflection dominated state, and a Compton thin state (Guainazzi et al., 2002). The transition, derived after a comparison between XMM-Newton and ASCA data, obtained six years earlier, is attributed to either a change in the properties of the absorbers or a switching-off of the nucleus during the ASCA observations. The former scenario may indicate a clumpy or patchy structure of the torus to which the absorbers are associated, while the latter may provide clues to the duty-cycle of the AGNs phenomenon.

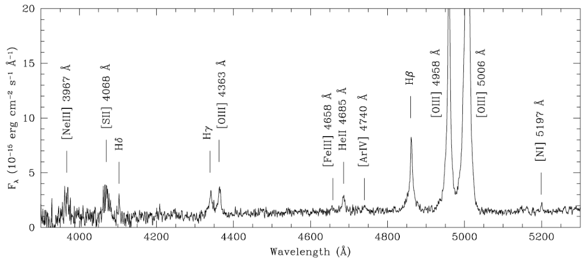

(a) Mrk 1210 Hβ + [O iii]

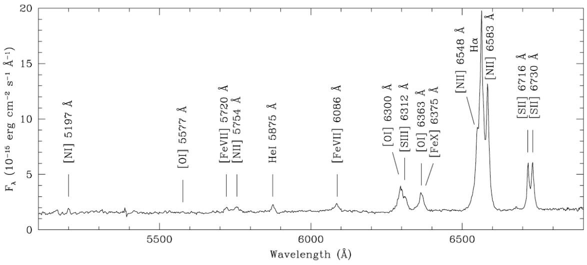

(b) Mrk 1210 Hα +[N ii]

Figure 6.28. Optical spectra of Mrk 1210 from Mazzalay and Rodríguez-Ardila (2007).

6.10.2 Mrk 1210: ISAAC observations and line fit.

We have observed Mrk 1210 on December 19th, 2011 with ISAAC at VLT in the J band using both LR and MR instrument modes. We used a 0.8″ × 1.0″ wide slit, corresponding to a spectral resolution of ∼430 km s^{-1} and

$\sim$ 60 km s^{-1} for LR and MR modes, respectively. The LR spectrum of Mrk 1210 was extracted with an aperture of 0.9$''$, while the MR spectrum with an aperture of 0.6$''$. The LR and MR spectra are shown in Figure 6.29, left and right side respectively.

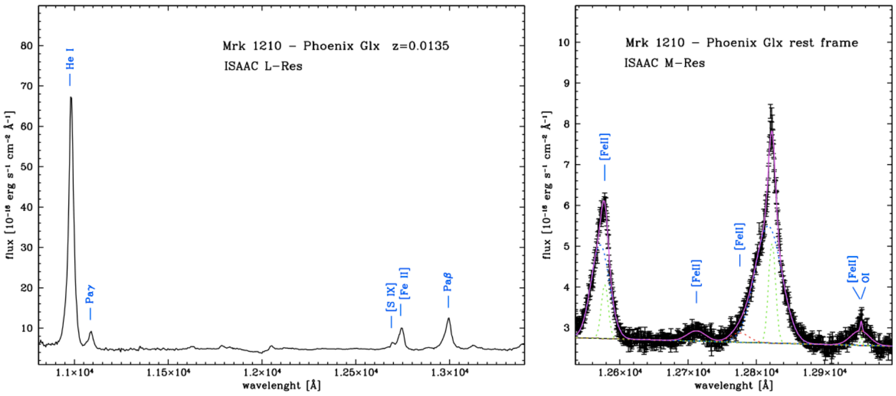

FIGURE 6.29. Left: flux calibrated ISAAC LR NIR spectrum of Mrk 1210. Right: rest frame, flux calibrated ISAAC MR NIR spectrum of Mrk 1210 and the fit of the Paβ emission line (solid magenta line). The green dashed line shows the narrow component of both Paβ and [Fe II] , the blue dashed line shows the broad componts of Paβ and [Fe II] , while the red dashed line represent the [Fe II] λ 12791 Å blended with the Paβ . NB.broad da discutere

The ISAAC/LR NIR spectrum of Mrk 1210 shows permitted and forbidden emission lines: in particular there is an intense He I well separated from the Paγ . There are also the Paβ and the [Fe II] λ12570 Ålines (Figure: 6.27, left side). As pointed out by Mazzalay and Rodríguez-Ardila (2007) in their optical spectra, all these feature show some kind of broadening.

The MR spectrum contains [Fe II] and Paβ lines as shown in Figure 6.27, right side. As usual we converted the spectrum to the rest frame wavelenght. We estimated the continuum with a power law and we identified two components both in the Paβ and the [Fe II] , that we modelled with gaussian profiles. The narrow line of the [Fe II] results to have its center at λ_c=12747.3 Åand a FWHM$_{Rest}$=291 km s^{-1} , while the second broader component has the center at λ_c=12740.4 Åand a FWHM$_{Rest}$=789 km s^{-1} . We notice that the latter is blueshifted of $\sim$7 Å with respect to the narrow line. Similar profile has been identified also in the Paβ line. It results to have a narrow gaussian component,

ISAAC/MR Mrk 1210 Paβ line fit				
Component	$\lambda_{\mathbf{c}}$ [Å]	σ_λ [Å]	**Norm**$_{Rest}$ [$\times 10^{-15}$]	**FWHM**$_{Rest}$[a] [**km s**$^{-1}$]
(1)	**(2)**	**(3)**	(4)	**(5)**
[Fe II] Narrow	12747.3±0.2	5.32±0.17	1.9±0.3	291
[Fe II] Broad	12740.4±0.3	14.42±0.74	7.6±0.3	789
Paβ Narrow*	12996.2 ±0.1	5.43±0.17	3.2±0.4	291
Paβ Broad	12991.4±0.6	19.37±8.9	13.6±0.5	1039
[Fe II] **	12953.1±1.3	14.66±0.74	1.3±0.5	789
[Fe II] **	12883.6±1.5	14.58±0.74	1.3±0.5	789
[Fe II] **	13125.7±1.3	14.85±0.74	1.2±0.3	789
O I	13128.3±0.7	3.15±0.8	2.3±0.1	167
Powerlaw: $\Gamma = 2.2 \pm 0.2$				
χ^2_ν= 0.85, ν= 810				

TABLE 6.18. Paβ line fitting parameters for our ISAAC/MR spectrum of Mrk 1210. (1) Emission line component; (2) Central wavelenght of the emission line; (3) σ for the gaussian component; (4) Rest frame normalization; (5) Rest frame FWHM. *σ_λ fixed to [Fe II] narrow line; **σ_λ fixed to [Fe II] broad component.

---

[a] To consider unpredictable sistematic errors on the FWHM measures, we assume a common uncertainty of 10%

whose width has been tied to the narrow [Fe II] one, and the broad component is centered at λ_c=12991.4 Åand has a FWHM$_{Rest}$=1039 km s^{-1} , it is also blueshifted of ~5 Å with respect the narrow component. The latter result to be centered at λ_c=12996.2 Å. Again, following the the NIR transitions listed in Landt et al. (2008) Table 4, we have added a gaussian model to take into account for the [Fe II] λ12791 Å in blending with the Paβ . In addiction, following Mazzalay and Rodríguez-Ardila (2007), we also modelled [Fe II] λ12712.3 Åand [Fe II] λ12952 Å. The fit parameters of Mrk 1210 are shown in Table 6.18.

6.11 MCG -01-24-012

6.11.1 MCG -24-012 in the literature

MCG -01-24-012 is a nearby spiral galaxy at redshift of z=0.0196, which hosts a Seyfert 2 nucleous (de Grijp et al., 1992). In the X-ray it was detected for the first time by Malizia et al. (2002), that performed a multiyear observations of some Pacinotti sample sources with BeppoSAX/PDS telescope. They measured the X-ray 2− 10 keV flux that results to be $\sim 1\times10^{11}$erg s^{-1} cm^{-2} . The 2−10 keV spectrum shows also the presence of the iron line Kα emission togheter with an absorbtions feature at ∼8.7 keV which cannot be explained by the presence of warm material around the source. Moreover, it turned out to be Compton-thin with $N_H \sim 7\times12^{22}$ athoms cm^{-2}. It belong to the 70-month SWIFT/BAT AGN sample and the [O III] image show an emission extended for 1".15×2".3 with the major axis along PA=75°, interpreted as an extended NLR (Schmitt et al., 2003). MCG -01-24-12 has also been observed by *Spitzer*/IRS. The corresponding low resolution staring-mode spectrum exhibits deep silicate absorption at 10μm and weak PAH emission (Mullaney et al., 2011). In the WISE images, the object appears elliptically extended along the galaxy major axis. Using K-band stellar luminosity of the bulge of MCG -01-24-012 Winter et al. (2009) derive its black hole mass: logM$_{BH}$= 7.16M$_\odot$. The optical spectrum, shown in Figure 6.30, was obtained by Jones et al. (2009) and it show narrow Hβ an Hα emission line.

6.11.2 MCG -01-24-012: ISAAC observations and line fit.

We have observed MCG -01-24-012 on January 7th, 2012 with ISAAC at VLT in LR an MR modes. We used a 0.8″ × 1.0″ wide slit, corresponding to a spectral resolution of ∼430 km s^{-1} and ∼ 60 km s^{-1} for LR and MR modes, respectively. Both the LR and MR spectra were extracted with an aperture of 0.9″. The flux calibrated LR and MR final spectra are shown in Figure 6.31, left and right side respectively.

The ISAAC/LR NIR spectrum of MCG -01-24-012 shows permitted and forbidden emission lines, in particular there are an intense He I well separated

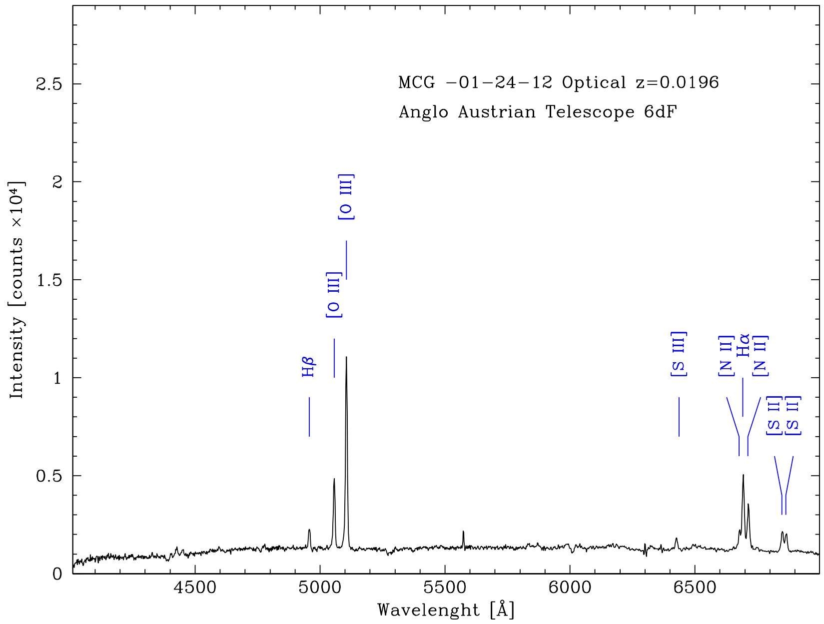

FIGURE 6.30. Optical spectrum of MCG -01-24-12 from Jones et al. (2009). There are no indications of broad components both in Hβ and Hα emission lines.

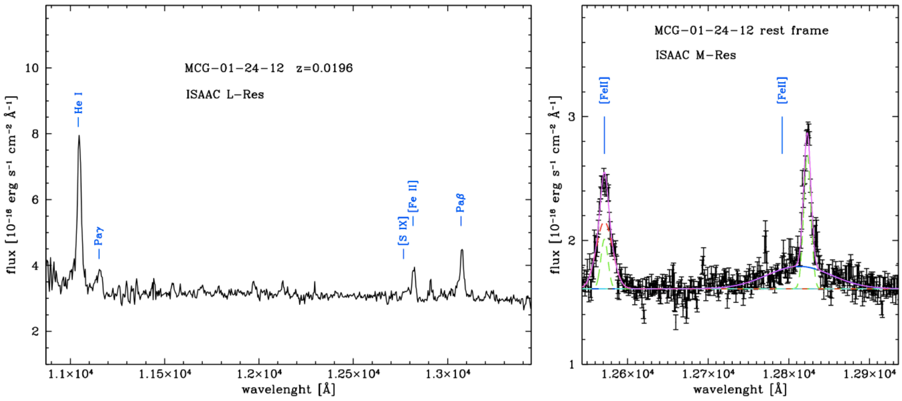

FIGURE 6.31. Left: flux calibrated ISAAC LR NIR spectrum of MCG -01-24-012. Right: rest frame, flux calibrated ISAAC MR NIR spectrum of MCG -01-24-012 and the fit of the Paβ line (magenta solid line). The green dashed line shows the narrow component, while the blue solid line shows the broad component. In cyano dashed line the [Fe II] λ12791 Åin blend with Paβ is shown.

from the Paγ , the Paβ and a weak [Fe II] λ12570 Å blended by the [S IX] forbidden lines (Figure: **??**, left side).

ISAAC/MR MCG -01-24-012 Paβ + [Fe II] line fit				
Component	$\lambda_\mathbf{c}$ [Å]	σ_λ [Å]	**Norm**$_{Rest}$ [$\times10^{-15}$]	**FWHM**$_{Rest}$[a] [**km s**$^{-1}$]
(1)	(2)	(3)	(4)	(5)
[Fe II] Narrow	12817.0 ±0.4	4.5±0.2	0.6±0.2	244
[Fe II] Broad	12818.8±0.6	10.3±0.1	1.9±0.2	557
Paβ Narrow*	13074.4 ±0.1	4.6±0.2	1.68±0.08	244
Paβ Broad	13064.1±2.6	40.9±3.4	2.5±0.5	2169
Powerlaw: Γ = 0.006 ±0.3				
$\chi^{\mathbf{2}}_\nu$= 1.48, ν= 381				

Table 6.19. Paβ line fitting parameters for our ISAAC/MR spectrum of MCG -01-24-012. (1) Emission line component; (2) Central wavelenght of the emission line; (3) σ for the gaussian component; (4) Rest frame normalization; (5) Rest frame FWHM. *σ_λ fixed to [Fe II] narrow line.

---

[a] To consider unpredictable sistematic errors on the FWHM measures, we assume a common uncertainty of 10%

The MR spectrum contains the [Fe II] and the Paβ lines and it is shown in Figure 6.31, right side. As usual we converted this spectrum to the rest frame wavelenght for the fitting procedure. We modelled the [Fe II] using two components of different widths: a narrow one that results to have the center at λ_c=12817.0 Å and the FWHM$_{Rest}$= 244 km s^{-1} . We used it to estimate the NLR contribute to the Paβ . The broader component has the center at λ_c= 12818.8 and a FWHM$_{Rest}$= 557 km s^{-1} , it is redshifted of ~2 Å with respect to the narrow line. Following the the NIR transitions listed in Landt et al. (2008) Table 4, we have added a gaussian model to take into account for the [Fe II] λ12791 Å in blending with the Paβ , but its contribution is neglectable. The Paβ has been modelled with two gaussian components, the narrow one has the center at λ_c=13074.4 and its width has been tied to the narrow [Fe II] line to carefully disentangle the NLR contribution from the BLR one. The broad emission component is weak but visible, and it results to have the center at λ_c= 13064.1 Å and a FWHM$_{Rest}$= 2169 km s^{-1} . We identified the latter as a result of the BLR gas under the gravitational potential of the central black hole. The fit parameters of MCG -01-24-012 are shown in Table 6.19.

6.12 CGCG -420-015

6.12.1 CGCG -420-015 in the literature

CGCG -420-015 is a nearby early type galaxy at redshift z=0.0294, optically classified as a Seyfert 2 (Strauss et al., 1992). It is a member of the Updated Zwicky Cathalog (UZC; Falco et al. 1999), the optical spectrum, shown in Figure 6.32, does not show any broad line signature in Hβ and Hα . No clear signs of starburst activity for this galaxy have been detected from the empirical multi-wavelenght analysis performed by Cid Fernandes et al. (2001). It was proposed as a new Compton-thick AGN candidate through the diagnostic diagram described in Severgnini et al. (2010) and this was confirmed from the broad band X-ray (0.4-100 keV) spectral analysis performed by Severgnini et al. (2011) using Suzaku and SWIFT/BAT observations. They found a N_H =1.3-1.5$\times$10^{24}cm^{-2} and a L$_{2-10keV}$=5-7$\times$10^{43} erg s^{-1} , in agreement with that predicted for the torus by Fraquelli et al. (2003). These authors after estimating the rate of the ionizing photons emitted by the AGN, assumed an opening angle of $\sim$30° for the ionization cones. Using K-band stellar luminosity of the bulge of CGCG 420-015, Winter et al. (2009) derive its black hole mass: log(M$_{BH}$)= 8.46M$_{\odot}$. The optical spectrum, shown in Figure 6.32, was obtained by Falco et al. (1999) and it show narrow Hβ an Hα emission line.

6.12.2 CGCG -420-015: ISAAC observations and line fit.

We have observed CGCG -420-015 on December 19th, 2011 at VLT with ISAAC in LR and MR modes. We used a 0.8$''$ $\times$ 1.0$''$ wide slit, correspondint to a spectral resolution of $\sim$430 km s^{-1} and $\sim$ 60 km s^{-1} for LR and MR modes, respectively. The spectrum of CGCG -420-015 was extracted with an aperture of 0.6$''$ and the final, flux calibrated LR and MR spectra are shown in Figure 6.33.

The ISAAC/LR NIR spectrum of CGCG -420-015 shows an intense He I ,

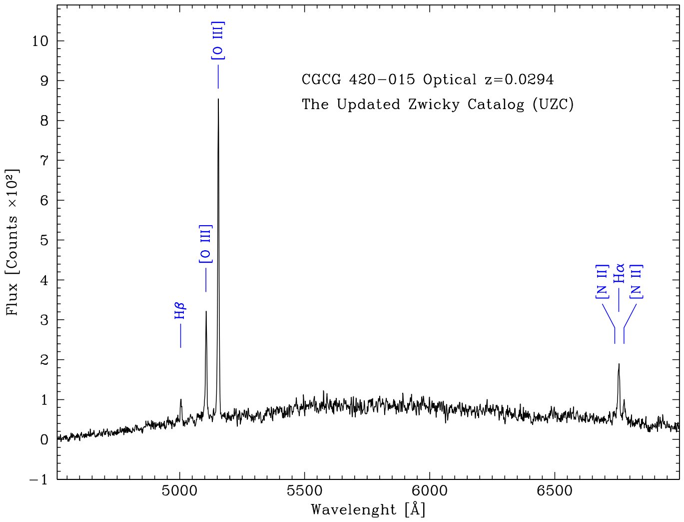

FIGURE 6.32. Optical spectrum of CGCG 420-015 from Falco et al. (1999)

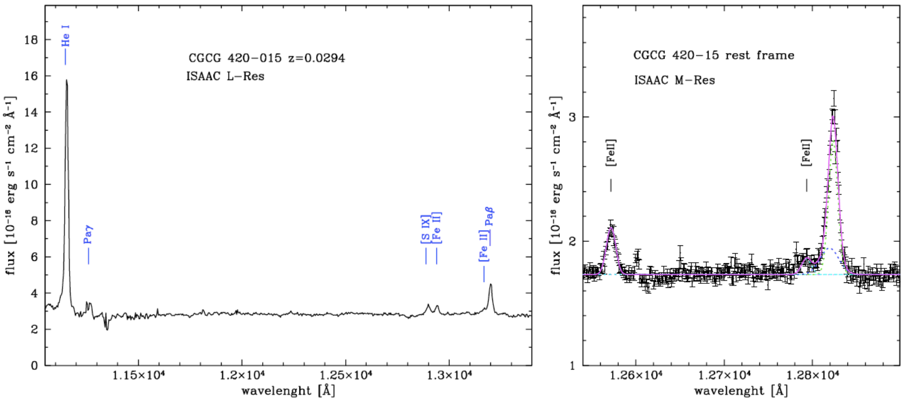

FIGURE 6.33. Left: flux calibrated ISAAC LR NIR spectrum of CGCG -420-015. Right: rest frame, flux calibrated ISAAC MR NIR spectrum of CGCG -420-015 and the fit of the Paβ + [Fe II] lines (magenta solid line). The green dashed line shows the narrow component both in [Fe II] and Paβ lines, while the blue dashed line shows the Paβ broad component. In cyano dashed line the [Fe II] λ12791 Å in blend with Paβ is shown.

well separated from the weaker Paγ . The Paβ shows evidence for a faint broad component at the base of a intense narrow line. The forbidden narrow lines [Fe II] λ12570 Å and [S IX] are in blending, but cleary visible (Figure: 6.33, left side).

ISAAC/MR CGCG -420-015 Paβ + [Fe II] line fit				
Component	$\lambda_{\mathbf{c}}$ **[Å]**	σ_{λ} **[Å]**	**Norm**$_{Rest}$ $[\times10^{-15}]$	**FWHM**$_{Rest}{}^{a}$ **[km s^{-1}]**
(1)	**(2)**	**(3)**	**(4)**	**(5)**
[Fe II] Narrow	12941.5 ±0.2	5.4±0.2	0.47±0.04	287
[Fe II] *	13169.3±0.2	5.5±0.2	0.17±0.04	287
Paβ Narrow*	13200.7 fixed	5.5±0.2	1.4±0.2	287
Paβ Broad	13194.4±2.3	10.0±0.2	0.5±0.2	522
Powerlaw: Γ = -1.6 ±0.2				
$\chi^{\mathbf{2}}_{\nu}$= 1.41, ν= 327				

Table 6.20. Paβ line fitting parameters for our ISAAC/MR spectrum of CGCG -420-015. (1) Emission line component; (2) Central wavelenght of the emission line; (3) σ for the gaussian component; (4) Rest frame normalization; (5) Rest frame FWHM. *σ_{λ} fixed to [Fe II] narrow line.

---

[a] To consider unpredictable sistematic errors on the FWHM measures, we assume a common uncertainty of 10%

The MR spectrum contains [Fe II] and Paβ lines and it is shown in Figure 6.33, right side. As usual we converted this spectrum to the rest frame wavelenght for the fitting procedure. We modelled the [Fe II] using one gaussian component centered at λ_c=12941.5 Å with a FWHM$_{Rest}$= 287 km s^{-1} and we used it to estimate the NLR contamination to the Paβ . Following the the NIR transitions listed in Landt et al. (2008) Table 4, we have added a gaussian model to take into account for the [Fe II] λ12791 Å in blending with the Paβ . We modelled the Paβ using two gaussian components. The narrow one has been fixed at λ_c=13200.7 Å and its width has been linked to the [Fe II] ones. The broad Paβ line has been modelled with a gaussian centered at λ_c=13194.4 Å with a FWHM$_{Rest}$= 522 km s^{-1} . We noticed that it is blueshifted of ~6 Å with respect to the narrow line. The fit parameters of CGCG -420-015 are shown in Table 6.20.

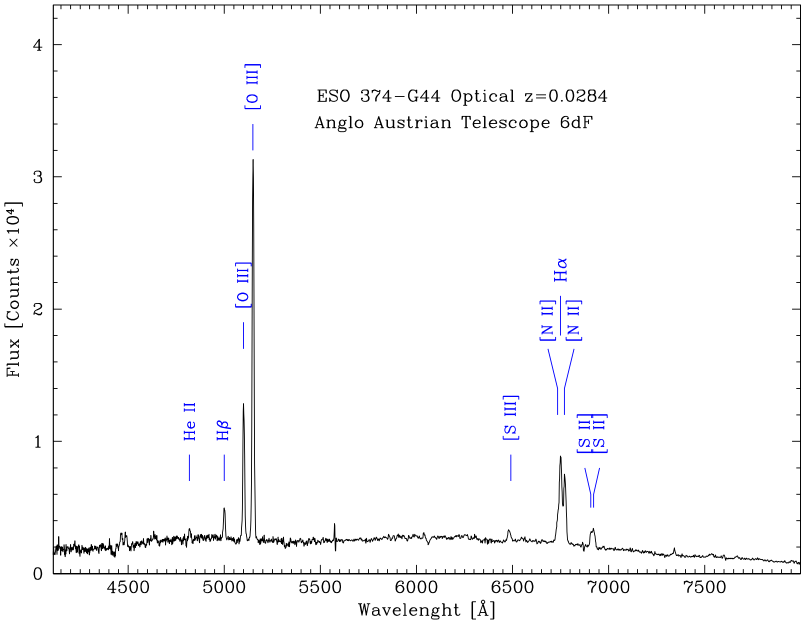

FIGURE 6.34. Optical spectrum of ESO -374-G44 from Jones et al. (2009)

6.13 ESO 374-G044

6.13.1 ESO 374-G044 in the literature

ESO 374 -G044 is a nearby SBa galaxy at redshift z=0.0284 hosting a Seyfert 2 nucleus. It was observed in the hard X-ray 22-month SWIFT/BAT survey that cover the hard x-ray band of 14-195 keV. Combining the hard X-ray luminosity from SWIFT/BAT 22M and the 18μm flux from AKARI infrared database, Matsuta et al. (2012) use this source, among other 158 AGNs, to derive an infrared and hard X-ray diagnostics of AGN identifcations. It optical spectrum is shown in Figure 6.34 and has been taken by Jones et al. (2009), it does not have indications for broad component in the Hβ and Hα emission lines.

6.13.2 ESO 374-G044: ISAAC observations and line fit.

We have observed ESO 374-G044 on January 22th, 2012 at VLT with ISAAC. The observations have been carried on in the J band using LR and MR instrument modes. We used a 0.8″ × 1.0″ wide slit, correspondint to a spectral resolution of ∼430 km s^{-1} and ∼ 60 km s^{-1} for LR and MR modes, respectively. The spectra of ESO 374-G044 were extracted with an aperture of 0.6″ and the final, flux calibrated LR and MR spectra are shown in Figure 6.35.

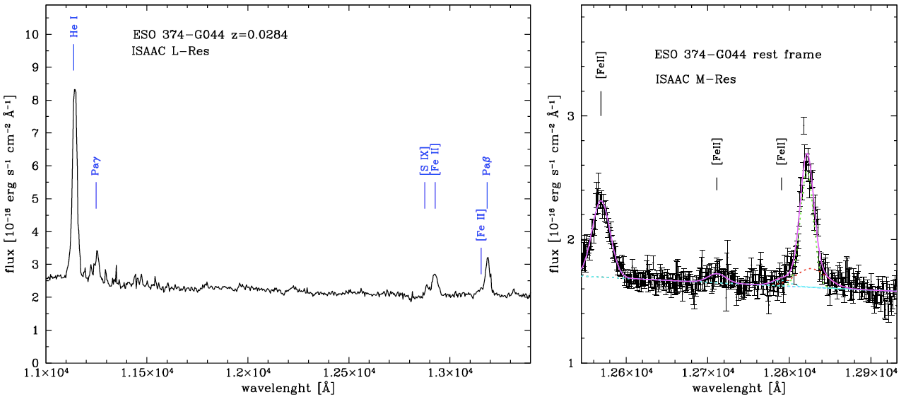

Figure 6.35. Left: Flux calibrated ISAAC LR NIR spectrum of ESO 374-G044. Right: Rest frame, flux calibrated ISAAC MR NIR spectrum of ESO 374-G044 and the fit of the Paβ + [Fe ii] lines (magenta solid line). The green dashed line shows the narrow component both in [Fe ii] and Paβ lines, while the red dashed line shows the Paβ broad component. In cyano dashed line the [Fe ii] λ12791 Å in blend with Paβ is shown.

The ISAAC/LR NIR spectrum of ESO 374-G044 shows an intense He i , well separated from a weak Paγ . In the Paβ there is and indication for a faint broad component at the base of a more intense narrow line. The forbidden narrow lines [Fe ii] λ12570 Å and [S ix] are in blending, but cleary visible (Figure: 6.35, left side).

The MR spectrum contains both [Fe ii] and Paβ lines and it is shown in Figure 6.35, right side. As usual we converted this spectrum to the rest frame wavelenght for the fitting procedure. We modelled the [Fe ii] using one gaussian component with the center at λ_c=12926.1 Å and a FWHM$_{Rest}$= 607 km s^{-1} but we did not used it to estimate the NLR contamination to the Paβ because of its blend with the [S ix] line. Following the the NIR transitions listed in Landt et al. (2008) Table 4, we have added a gaussian model to take into account for the [Fe ii] λ12791 Å in blending with the Paβ . We modelled the Paβ using two gaussian components. The narrow one results to be centered at λ_c=13185.8 Å and it has a FWHM$_{Rest}$= 427 km s^{-1} . The

ISAAC/MR ESO 374-G044 Paβ + [Fe II] line fit				
Component	$\lambda_\mathbf{c}$ [Å]	σ_λ [Å]	**Norm**$_{Rest}$ [$\times10^{-15}$]	**FWHM**$_{Rest}$^{a} [**km s**$^{-1}$]
(1)	**(2)**	**(3)**	**(4)**	**(5)**
[Fe II] Narrow	12926.1 ±0.4	11.42±0.07	1.6±0.08	607
[Fe II] *	13072.5±0.4	11.55±0.07	0.19±0.08	607
[Fe II] *	13153.7±0.4	11.62±0.07	0.11±0.11	607
Paβ Narrow	13185.8±0.3	8.2±0.5	1.8±0.4	287
Paβ Broad	13191.0±5.4	20.0±1.0	0.8±0.5	1041
Powerlaw: Γ = 2.5 ±0.3				
χ^2_ν= 0.93, ν= 418				

TABLE 6.21. Paβ line fitting parameters for our ISAAC/MR spectrum of ESO 374-G044. (1) Emission line component; (2) Central wavelenght of the emission line; (3) σ for the gaussian component; (4) Rest frame normalization; (5) Rest frame FWHM.

---

[a] To consider unpredictable sistematic errors on the FWHM measures, we assume a common uncertainty of 10%

broad Paβ line has been modelled with a gaussian centered at λ_c=13191.0 Å with a FWHM$_{Rest}$= 1041 km s^{-1} . It is redshifted of ~5 Å with respect to the narrow line. The fit parameters of ESO 374-G044 are shown in Table 6.21.

6.14 NGC 3081

6.14.1 NGC 3081 in the literature

NGC 3081 is a well known Seyfert 2, low inclination barred spiral galaxy at redshift z=0.008. It represents one of the best exemples of a resonance ring barred galaxy in the sky, with one of the most distinctive multiring morphologies among the general galaxy population, and it is an especially good candidate for studies of star formation in rings (Buta and Purcell 1998, Byrd et al. 2006).

Thanks to the extremely high angular resolution FIR (70−500μm) images obtained with the *Herschel Space Observatory* instruments PACS and SPIRE,

Ramos Almeida et al. (2011) resolved the nuclear dust distribution of NGC 3081, finding indications for a clumpy torus models for the AGN.
Moran et al. (2000) report spectacular type 1 features in NCG 3081 optical spectrum in polarized light , with prominent broad components of Hα , Hβ and also in He I λ5876 Å, shown in Figures 6.36. The authors report a FWZI=7000 km s^{-1} for polarized Hα , despite its pure type 2 optical spectrum, suggesting that NGC 3081 could hosts an hidden BLR .
Bian and Gu (2007) used the stellar velocity dispertions and the extinction-corrected [O III] luminosity to derive the SMBH mass and the Eddington luminosity for a sample of 90 AGN2 with spectropolarimetric signatures of hidden broad line region. Thus they derived a black hole mass for the NCG 3081 nucleous of log(M$_{BH}$)= 7.4±0.3 M$_{\odot}$ ad an Eddington ratio of λ~0.26.

Fewer X-ray observations have been performed on this source. It was first detected in X-rays by the Einstein imaging instruments and then it was also detected the ROSAT All-Sky Survey. BeppoSAX observed NGC 3081 in a lower state with a flux of F$_{2-10keV}$ =1.3×10^{-12} erg s^{-1} cm^{-2} explained with a Compton thin transmission model by Maiolino et al. (1998).
From *Suzaku* follow up observations Eguchi et al. (2011) derived a model for the nuclear region in which it appears to have a torus with very small opening angles (~15°), observed in a face on geometry. Its spectra is also characterized by an heavy absorption with N_H ~10^{24} cm^{-2}. The AGN is very compact in radio band and posseses a biconical NLR extending for ~4" along PA ~ 160°. In the *Spitzer*/IRAC images the nucleous is still very compact and is embedded within week lenticular host emission (north-south direction) and surrounded by a large scale ring.

6.14.2 NGC 3081: ISAAC observations and line fit.

We have observed NGC 3081 on January 6th, 2012 at VLT with ISAAC in the J band using both LR and MR instrument modes. We used a 0.8″ × 1.0″ wide slit, correspondint to a spectral resolution of ~430 km s^{-1} and ~ 60 km s^{-1} for LR and MR modes, respectively. The LR spectrum of NGC 3081 was extracted with an aperture of 0.9″, while the MR spectrum was extracted with a narrower aperture of 0.4″. The LR and MR spectra are shown in Figure

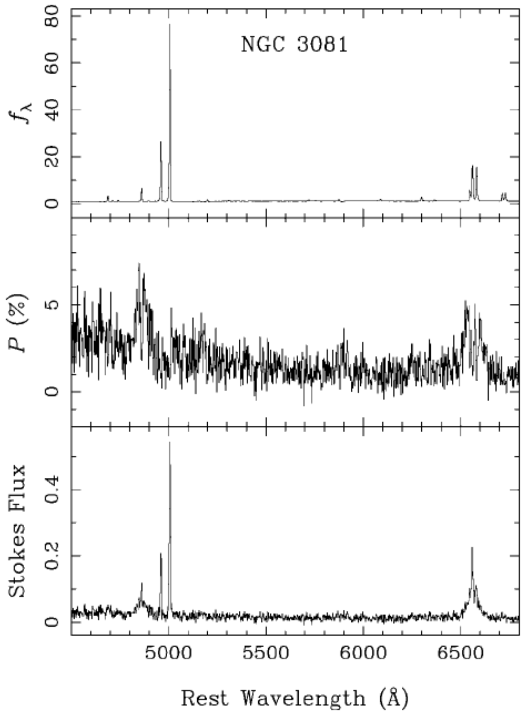

FIGURE 6.36. Optical spectropolarimetry for NGC 3081 from Moran et al. (2000)

6.37, left and right side respectively.

In the ISAAC/LR NIR spectrum NCG 3081 shows an intense He I emission line, well separated from the Paγ , and the Paβ . There are also weak [Fe II] λ12570 Å and [S IX] forbidden lines (Figure: 6.37, left side). Unfortunatly in the 2D spectra there is a prominent signature of galaxy rotation in the Paβ (see Figure 6.38), which complicated the interpretation of the line components during the line fitting procedures. Thus we decided to extract the MR spectrum with an aperture as narrow as possible ($\sim 0.4''$) in order to reduce this contamination in the best way.

The MR spectrum Paβ shows a narrow line with a weak broad component arising from the background (Figure 6.37, right side.) We converted the spectrum to the rest frame wavelenght and estimated the continuum with a power law. We tried to model the Paβ line with two gaussian components and we included also the [Fe II] λ12791 Å in blending with Paβ . From our fit the narrow

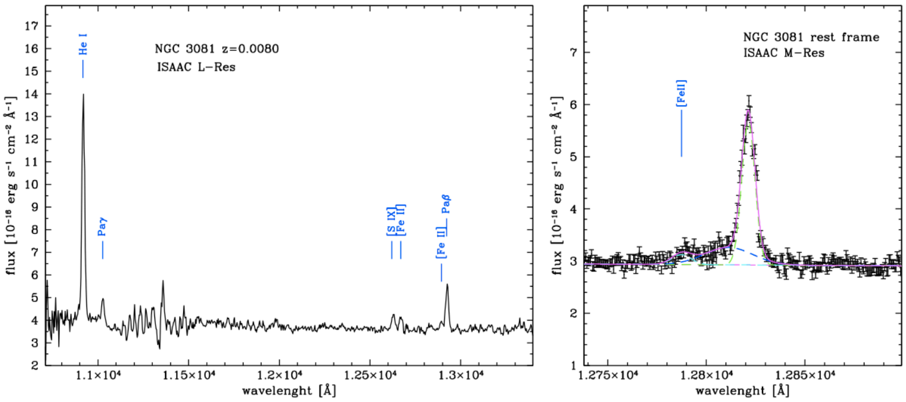

FIGURE 6.37. Left: flux calibrated ISAAC LR NIR spectrum of NGC 3081. Right: rest frame, flux calibrated ISAAC MR NIR spectrum of NGC 3081 and the fit of the Paβ line (magenta solid line). The green dashed line shows the narrow component, while the blue dashed line shows the broad component. In cyano dashed line the [Fe II] λ12791 Åin blend with Paβ is shown.

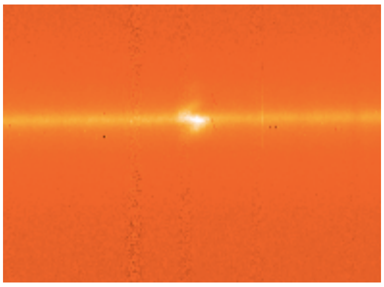

FIGURE 6.38. NGC 3081 2D spectra. There is a clear signature of galaxy rotation in the Paβ line (λ=12923.9 Å).

Paβ results to be centered at λ_c=12923.9 Å and to have a FWHM$_{Rest}$=173 km s^{-1} , while the weak broad component results to be centered at λ_c=12916.3 Å and has a FWHM$_{Rest}$=619 km s^{-1} . Moreover it is blueshifted of ~7 Å with respect to the narrow line. The fit parameters of NGC 3081 are shown in Table 6.22.

Due to the contamination of the galaxy's rotation we could not accurately identify the BLR component of the Paβ , thus we did not use it for the BH mass estimation.

ISAAC/MR NGC 3081 Paβ line fit				
Component	$\lambda_{\mathbf{c}}$ [Å]	σ_λ [Å]	**Norm**$_{Rest}$ [$\times 10^{-15}$]	**FWHM**$_{Rest}$[a] [km s^{-1}]
(1)	**(2)**	**(3)**	**(4)**	**(5)**
Paβ Narrow	12923.90 ±0.07	3.2±1.3	2.19±0.08	173
Paβ Broad	12916.3±0.9	11.4±0.1	1.11±0.02	619
[Fe II]	12891.9±0.5	3.2±1.3	0.22±0.05	173
Powerlaw: $\Gamma = 0.99 \pm 0.42$				
$\chi^{\mathbf{2}}_{\nu}= 1.7$, $\nu = 289$				

TABLE 6.22. Paβ line fitting parameters for our ISAAC/MR spectrum of Mrk 1210. (1) Emission line component; (2) Central wavelenght of the emission line; (3) σ for the gaussian component; (4) Rest frame normalization; (5) Rest frame FWHM.

---

[a] To consider unpredictable sistematic errors on the FWHM measures, we assume a common uncertainty of 10%

Chapter 7

The virial measure of the AGN2 BH masses

As previously discussed in Chapter 5, following the work of Landt et al. (2008, 2011, 2013), we have derived two new NIR virial relationships based on the FWHM of the broad component of Paβ emission line and the hard X-ray luminosity in the 14-195 keV band, or the Paβ luminosity itself. These relations are less affected by dust obscuration and the galaxy contamination problems. Thus, they are able to reliably measure the BH mass also on those obscured or low luminosity AGN where the nuclear component is less visible and/or contaminated by the hosting galaxy. Thanks to our near infrared observations, performed using ISAAC and Xshooter at VLT and LUCI at LBT, we are now able to derive, for the very first time, the BH masses in AGN2 and intermediate AGN (type 1.8 and 1.9) using the NIR virial relation (see Chapter 5). Moreover, since the BLR emission lines Paα , Paβ and He I are well correlated with the Balmer broad lines (Landt et al., 2008), see Figure 7, we can derive a virial BH mass measurments also for the AGN of our sample that have shown in their IR spectra, not only the broad component of Paβ line, but also the Paα and He I ones, allowing us to span the redshift range 0$\leq z \lesssim$ 0.1.

In the following we will present our estimation for the BH masses of the obscured and intermediate AGN of our SWIFT70M sample, whose infrared spectra have shown broad components of BLR emission lines.

7.1 The BH mass measurement

We found broad components of BLR emission lines in 13 obscured AGN (AGN2, AGN1.8 and AGN1.9) from our sample of 41 AGN randomly selected from the hard X-ray survey SWIFT/BAT 70 Month. Since these sources are obscured, we decided to derive their black hole masses using only our Paβ -

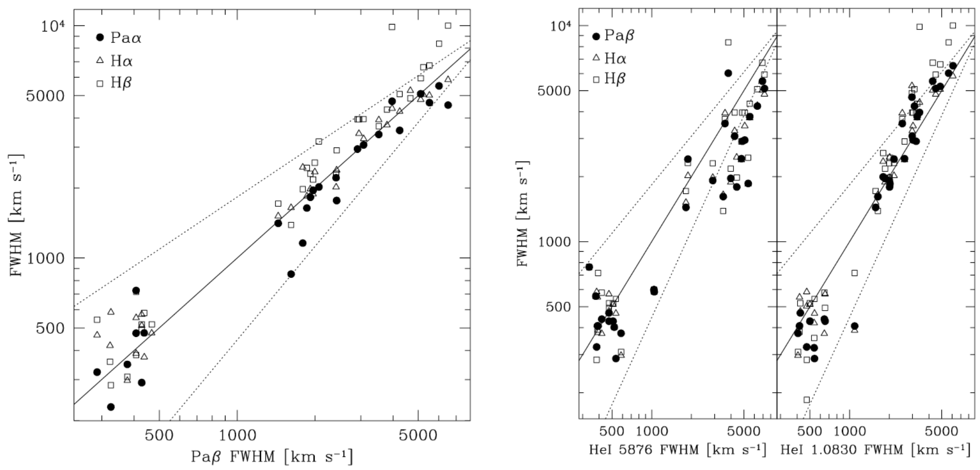

FIGURE 7.1. Left: Comparison between the FWHM of broad and narrow lines (upper right and lower left symbol, respectively) of Paβ vs. Paα (filled circles), Hα (open triangles) and Hβ (open squares). Right: Comparison between the FWHM of broad and narrow lines (upper right and lower left symbol, respectively) of He I vs. Paβ , Hα and Hβ . In both cases the compared emission lines have similar widths (solid line) whithin the error range (dotted lines) (Landt et al., 2008).

L_X NIR virial relation, see Equation 5.6 in Chapter 5, in order to have a more accurate BH mass estimation. In Table 7.1 we report: the FWHM values resulting from the line fit procedures (described in Chapter 6) for the AGN with broad component of BLR emission lines, their hard X-ray luminosities in the 14-195 keV band, taken from Baumgartner et al. (2013), their redshifts and the Swift classifications.

After performing the fitting procedures, we applied the resulting rest frame FWHM and the corresponding source hard X-ray luminosity to the Equation 5.6, that allowed us to derive the BH mass measure for all 13 objects. We choose to use the rest frame FWHM of the broad component of Paβ every time it is present in the source spectrum; when this was not possible we used the FWHM of broad component of Paα or, otherwise, the He I . In particular, 2MSXJ11+19 has an high redshift (z=0.1509, the highest redshift of our subsample), thus its Paβ line falls into a IR telluric absorption band. However, both Paα and He I are present in its spectrum and we decided to use the hidrogen paschen line Paα for the BH mass estimation due to its good correlation with Paβ (see Figure 7).

FWHM measured from the line fits of our 13 AGN showing broad component in the BLR NIR emission line

object name **(1)**	**z** **(2)**	**cl** **(3)**	**logL$_X$** [erg/s] **(4)**	**Paα** N/B **(5)**	**Paβ** N/B **(6)**	**Paγ** N/B **(7)**	**HeI** N/B **(8)**	**[FeII]** N/B **(9)**
2MSXJ11+19	0.1059	1.8	44.65	272/616	–	–/544	145/728	–
CGCG -420-015	0.0294	2	43.75	–	287/522	–	–	287/–
ESO 374-G044	0.0284	2	43.57	–	287/1041	–	–	607/–
LEDA 093974	0.0239	2	43.68	–	319/900	–	319/1107	319/840
MCG-01-24-12	0.0196	2	43.55	–	244/2169	–	–	244/557
MCG -05-23-16 (IS)	0.0085	2	43.51	–	256/1049/3149	–	–	385/–
MCG -05-23-16 (Xsh)	0.0085	2	43.51	–	258/1496/3976	258/1938	258/2341	258/–
Mrk 1210	0.0135	2	43.35	–	291/1039	–	–	291/789
NGC1365	0.0055	1.8	42.63	–	421/1056/3248	–	–	370
NGC2992	0.0077	2	42.55	–	236/679/2019	–	–	236/679
NGC4395	0.0013	1	40.79	–	211/755	–	–	211/–
NGC6221	0.0050	2	42.17	–	141/481/2257.2	132/318/1447	132/318/1637.2	141/481
NGC7314	0.0048	1.9	42.42	–	136/1165	–	–	114/–
NGC7465*	0.0066	2	42.14	390/–	120/2300	220/–	–/1060	200/–

TABLE 7.1. The FWHM results from the line fit procedures. We found broad components of NIR permitted lines in 13 of 41 AGN of our SWIFT70M sample. (1) The source name; (2) the source redshift from Baumgartner et al. (2013); (3) Source classifications (Baumgartner et al., 2013); (4) X-ray luminosity in the 14-195 keV band (Baumgartner et al., 2013); (5) FWHM of Paα narrow (N) and broad (B) components in km s^{-1} ; (6) FWHM of Paβ narrow (N) and broad (B) components in km s^{-1} ; (7) FWHM of Paγ narrow (N) and broad (B) components in km s^{-1} ; (8) FWHM of He I narrow (N) and broad (B) components in km s^{-1} ; (9) FWHM of [Fe II] narrow (N) and broad (B) components in km s^{-1} . The uncertainties on the FWHM are estimated to be at 10%. *data taken from Ramos Almeida et al. (2009)

The LEDA 093974 Xshooter NIR spectrum shows an intense He I line and a noisy Paβ lines, due to the proximity of an absorption telluric band. Since it was hard to perform a reliable fit of the Paβ , we decided to use the rest frame FWHM resulting from the He I line fit (see Section 6.5).
As descibed in Section 6.4, we have fitted both the ISAAC MR and the Xshooter spectra of MCG -05-23-16 and we found two broad Paβ components. We used the broader ones from both spectra to derive the BH mass, finding that the two estimates are compatible in the uncertainties range. Thus we calculate an average value from the two indipendent measurements.
The source NGC 7465 has been analyzed by Ramos Almeida et al. (2009), who found broad components of BLR lines in its IR spectrum. We used the FWHM reported by the authors.

All the 14-195 keV X-ray luminosities are taken from the SWIFT/BAT 70 Month (Baumgartner et al., 2013), but for NGC 6221 the corresponding X-ray flux results to be contaminated by nearby galaxies. Thus we decided to use the $L_{20-100keV}$ from the INTEGRAL observations of Beckmann et al. (2009), we converted it into $L_{14-195keV}$:

$$log(L_{14-195}) = log(L_{20-100}) - log(100^{0.3} - 20^{0.3}) + log(195^{0.3} - 14^{0.3}), \quad (7.1)$$

and we found $log(L_{14-195})$=42.17$\pm$0.34 erg s^{-1} .
The BH mass measure uncertainties depend on both the FWHM measurements and the X-ray luminosities. Due to unpredictable sistematic errors on the FWHM estimate and following the studies of Grupe et al. (2004); Vestergaard and Peterson (2006); Landt et al. (2008); Denney et al. (2009), we have preferred to assume a common uncertainty of 10%. While, starting from the SWIFT X-ray flux errors reported in Baumgartner et al. (2013)[a], we calculated the the error on the $log(L_X)$ using the Equation:

$$\sigma_{\log L_{X,i}} = \delta(\log e \ln L_{Xi}) = \log e \frac{\sigma_{L_{X,i}}}{L_{X,i}} = \log e \frac{\sigma_{F_i}}{F_i}. \quad (7.2)$$

where σ_{F_i} represent the flux uncertainty F_i in the 14-195 keV for the $i-$th source.

---

[a] The authors report a 90% of confidence level that we have converted to the 68% dividing by a factor of 1.64

Thus, the overall uncertainty on the Virial product ($XVir = 2\log FWHM_{Pa_\beta} + 0.5\log L_X$) is derived applying the error popagations theory:

$$\sigma_{XVir} = \sqrt{(2\log e 0.1)^2 + \left(0.5\log e \frac{\sigma L_{X,i}}{L_{X,i}}^2\right)} \tag{7.3}$$

Finally the overall errors on the BH mass estimates are calculated using:

$$\sigma_{M_{BH}} = \sqrt{\sigma_b^2 + \sigma_a^2 XVir^2 + a^2\sigma_{XVir}^2 + 0.21^2}, \tag{7.4}$$

where a, b, σ_a and σ_b are the parameters obtained from the fit of the virial relation and their uncertainties, respectively (see Section 5.2.1, Equation 5.3), and 0.21 is the relation spread.

In Table 7.1 we report the rest frame FWHM of the broad components used in the Equation 5.6, the SWIFT70M 14-195 keV hard X-ray luminosities, taken from Baumgartner et al. (2013) and the BH masses resulting from our virial relation. For some sources we also report previous BH mass measure available in literature. In Figure 7.2 we show the hard X-ray luminosity distribution for the observed AGN2 (blue) and for the AGN2 with virial BH mass estimates (magenta), we notice that there are no particular trends with luminosity.

As shown in Table 7.1 the majority of the BH masses result to be lower than 10^7M$_\odot$.

We notice that there is an high discrepance between the BH mass of 2MSXJ11+19 derived using the Paβ $-L_X$ relation and the value found by Winter et al. (2010). The authors reported a BH mass of log(M_{BH})=9.00 M$\odot$ derived using stellar K-band photometry from Two Micron All-Sky Survey (2MASS). Our value is considerably lower and yield to a super Eddington value for λ_{Edd}. Since the NIR BLR lines used by us are seen in noisy regions of the AGN spectrum, we consider our BH mass as a tentative of estimation.

In Figure 7.3 the L$_X-$M$_{BH}$ plane for our 13 AGN2 with virial BH mass estimates (red filled dots) is shown. For comparison we also represent the distribution of a sample of $\sim$30 AGN1 (blue empty squares) whose BH mass estimates have been derived using reverberation mapping techniques or M$_{BH}-$L bulge scaling relations and have been taken from several authors. For MCG -01-23-16 we reported the average BH mass value, obtained from ISAAC and Xshooter observations.

AGN Black Hole masses from our virial relations

object name **(1)**	**z** **(2)**	**cl** **(3)**	**logL$_X$** [erg/s] **(4)**	**FWHM$_{rest}$** [km/s] **(5)**	**logM$_{BH}$** [M$_\odot$] **(6)**	**logM$_{BH}$lit.** [M$_\odot$] **(7)**
2MSXJ11+19	0.1059	1.8	44.65	616	6.70±0.24	9.00 W10
CGCG 420-15	0.0294	2	43.75	522	6.19±0.25	
ESO 374G44	0.0284	2	43.57	1041	6.63±0.24	
LEDA 093974	0.0239	2	43.68	1107	6.72±0.24	
MCG -01-24-12	0.0196	2	43.55	2169	7.16±0.24	7.16 W10
MCG -05-23-16 (IS)	0.0085	2	43.51	3149	7.42±0.24	6.3±0.5 B09
MCG -05-23-16 (Xsh)	0.0085	2	43.51	3976	7.60±0.24	6.3±0.5 B09
MCG -05-23-16 (Ave)[a]	0.0085	2	43.51	3563	7.50±0.24	6.3±0.5 B09
Mrk 1210	0.0135	2	43.35	1039	6.53±0.24	
NGC1365	0.0055	1.8	42.63	1056	6.24±0.25	7.7±0.3 B09
NGC2992	0.0077	2	42.55	2019	6.68±0.24	7.7±0.3 B09
NGC4395	0.0013	1.9	40.79	786	5.24±0.26	5.4±0.2 E12
NGC6221	0.0050	2	42.17**	2257	6.62±0.24	
NGC7314	0.0048	1.9	42.42	1165	6.22±0.25	6.0±0.5 B09
NGC7465*	0.0066	2	42.14	2300	6.60±0.24	

TABLE 7.2. AGN2 BH mass measurments using our NIR virial relation (Equation 5.6). (1) Source name; (2) Source redshift from Baumgartner et al. (2013); (3) SWIFT classification; (4) X-ray luminosity in the 14-195 keV band from Baumgartner et al. (2013); (5) Rest frame FWHM of broad permitted lines used in the virial relation; (6) BH mass estimated using the NIR virial relation (Equation 5.6); (7) BH masses estimate from literature (B09=Beckmann et al. (2009); E12=Edri et al. (2012); W10=Winter et al. (2010).* Data taken from Ramos Almeida et al. (2009); **L_{14-195} derived from INTEGRAL L_{20-200} (Beckmann et al., 2009).

---

[a] Average values calulated from the Xshooter and ISAAC measurements.

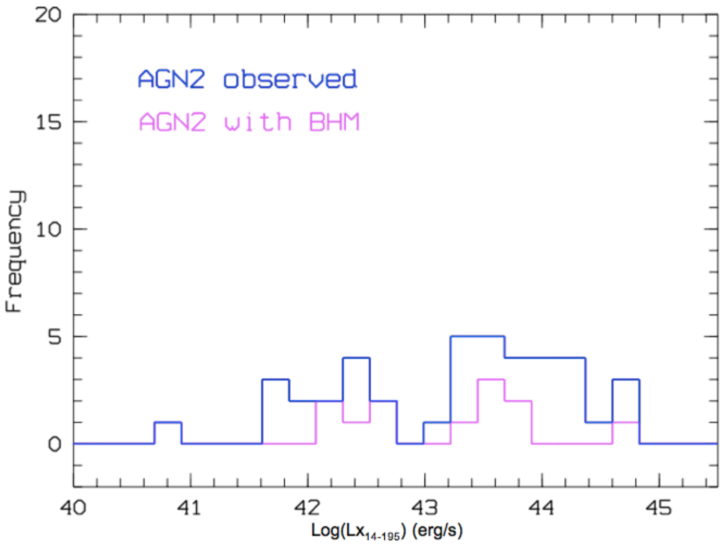

FIGURE 7.2. The hard X-ray luminosity distribution for the observed AGN2 *Swift* subsample (blue) and for the AGN2 with virial BH mass estimates (magenta). There is no particular luminosity trand in our selection.

Our sample of 13 AGN2 results to have on average BH masses 0.8 dex smaller than AGN1 having the same intrinsic hard X-ray luminosity. Indeed in the luminosity range 43.2<log$L_{14-195keV}$ <44 erg s^{-1} , AGN1 shows an average BH mass of logM_{BH}=7.60±0.1 $M_{\odot}$, while our AGN2 show an average BH mass of logM_{BH}=6.80±0.2 $M_{\odot}$. Therefore AGN2 result to have higher Eddington ratios (some of them are super-Eddington) with respect to the AGN1 population of the same luminosity, as shown in the L_{bol}−L_{Edd} plane in Figure 7.4.

The Eddington luminosity (L_{Edd}) for our 13 AGN has been derived starting from the corresponding virial BH mass measurments, using Equation 3.2, while to derive the bolometric luminosity L_{bol} we follow the method described in Shankar et al. (2013), in which the authors developed an analytical approximation for an X-ray bolometric correction K_{bol} as a function of the Eddington ratio (λ_{Edd}) (see also Vasudevan and Fabian 2007). In particular, they use a well-defined relationship between the bolometric correction and the Eddington ratio with a transitional region at λ_{Edd} ∼0.1:

$$K_{bol}(\lambda_{Edd}) = \begin{cases} 18 & \lambda_{Edd} \leq 0.105 \\ 54.85 + 26.78 \log L_X & \\ -11.11(\log L_X)^2 & 0.105 \leq \lambda_{Edd} \leq 1. \end{cases}$$

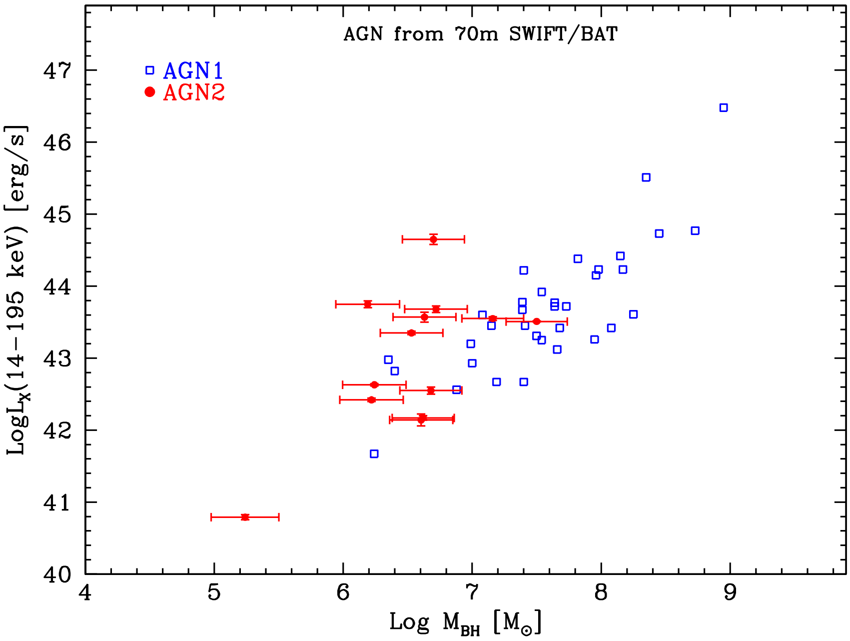

FIGURE 7.3. The L_X−M_{BH} plane for our 13 AGN2 with virial estimations of BH mass (red solid dots). For comparison we also show ∼ 30 AGN1 (blue open squares) with BH masses derived from reverberation mapping techniques or or the M_{BH}− L Bulge scaling relation. AGN2 shows BH masses on average lower than AGN1 of the same luminosity.

The resulting values for L_{Edd}, L_{bol} and M_{BH} and their conresponding uncertanties are shown in Table 7.3.

Eddington and bolometric luminosities for our 13 AGN with virial BH masses

object name (1)	**logL_X** **[erg/s]** (2)	**logM_{BH}** [$M_\odot$] (3)	logL_{Edd} **[erg/s]** (4)	logL_{bol} **[erg/s]** (5)
2MSXJ11+19	44.65	6.70±0.24	44.71±0.24	46.50±0.12
CGCG 420-15	43.75	6.19±0.25	44.29±0.25	45.58±0.11
ESO 374G44	43.57	6.63±0.24	44.73±0.24	45.32±0.12
LEDA 093974	43.68	6.72±0.24	44.82±0.24	45.43±0.11
MCG -01-24-12	43.55	7.16±0.24	45.26±0.24	44.80±0.10
MCG -05-23-16 (IS)	43.51	7.42±0.24	45.52±0.24	45.29±0.10
MCG -05-23-16 (Xsh)	43.51	7.60±0.24	45.69±0.24	44.77±0.10
MCG -05-23-16 (Ave)[a]	43.51	7.50±0.24	45.60±0.24	44.77±0.10
Mrk 1210	43.35	6.53±0.24	44.63±0.24	45.07±0.10
NGC1365	42.63	6.24±0.25	44.34±0.25	43.89±0.10
NGC2992	42.55	6.68±0.24	44.78±0.24	43.81±0.11
NGC4395	40.79	5.24±0.26	43.34±0.26	42.05±0.10
NGC6221	42.17	6.62±0.24	44.65±0.24	43.43±0.10
NGC7314	42.42	6.22±0.25	44.32±0.25	43.68±0.10
NGC7465*	42.14	6.60±0.24	44.79±0.24	43.39±0.13

TABLE 7.3. Eddington and bolometric luminosities for our subsample of 13 AGN2 with virial mass estimates. (1) Source name; (2) X-ray luminosity in the 14-195 keV band; (3) Virial Black hole mass; (4) Eddington luminosity; (5) Bolometric luminosity.

---

[a] Average values calulated from the Xshooter and ISAAC measurements.

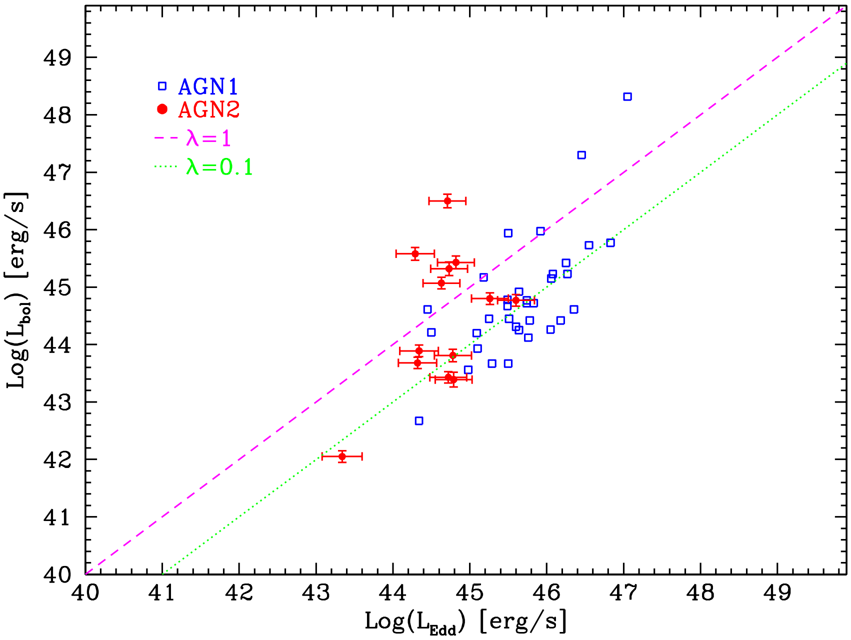

FIGURE 7.4. The L_{Edd}–L_{bol} plane for our 13 AGN2 with virial estimations of BH mass (red solid dots). For comparison we also show ∼ 30 AGN1 (blue open squares) with BH masses derived from reverberation mapping techniques or or the $M_B H-$ L Bulge scaling relation. The magenta dashed line indicates the Eddington luminosity value (λ_{Edd}=1); the green dotted line represent on Eddington ratio of λ_{Edd}=0.1. AGN2 result to have larger Eddington ratios (some of them are super-Eddington) with respect to the AGN1 population of the same luminosity.

Chapter 8

Conclusions and future prospectives

In order to have a complete sample of obscured and intermediate AGN (AGN2, AGN1.9 and AGN1.8) with hard X-ray (14-195 keV band) luminosity measurments, we randomly selected 41 sources from the *Swift*/BAT 70 month hard X-ray catalog. We performed deep NIR spectroscopic observations both in south and north emispheres using the spectrographs ISAAC and Xshooter at VLT and LUCI at LBT, finding broad components in NIR permitted emission lines in 13 out of 41 obscured AGNs.

As discussed in Chapter 5, the measure of local, low mass, BHs, such as NGC 4395, is of great importance as these BHs give important informations on the AGN/galaxy formation and evolution. NGC 4395 hosts one of the local, smallest, BH of AGN origin ever found. Previous measures (if f=4.31 is used) obtained M_{BH}=2.81 $^{+0.86}_{-0.66}\times 10^5 M_\odot$ from a reverberation mapping analysis of the CIV emission line (Peterson et al., 2005) and $M_{BH} = (2.69 \pm 1.42) \times 10^5 M_\odot$ from a reverberation mapping analysis of the Hβ emission line (Edri et al., 2012).

In order to overcome the dust obscuration and galaxy contamination problems, we have derived two new SE BH mass relationships based on the FWHM and luminosity of the BLR component of the Paβ emission line and on the hard X-ray luminosity in the 14-195 keV band. These relationships have been initially calibrated in the $10^7 - 10^9$ $M_\odot$ mass range and have then been used to obtain a new independent BH mass measure of NGC 4395. We obtained M_{BH}=1.7 $^{+1.3}_{-0.7}\times 10^5 M_\odot$, which resulted in agreement (<1 σ) with the two previous existing estimates, therefore confirming the very small mass of its BH. Moreover, thanks to our new measure of the Paβ line and mass of NGC 4395 we were able to extend in the $10^5 - 10^9$ $M_\odot$ mass range our SE relationships. These relations are able to reliably measure the BH mass on those obscured or low luminosity AGN where the nuclear component is less visible and/or contaminated by the hosting galaxy.

Our first results confirm that the new derived NIR and hard X-ray based SE relationships do work properly in measuring the AGN BH masses. We can then conclude that our new derived NIR and hard X-ray based SE relationships could be of great help in measuring the BH mass in low luminosity and absorbed AGN and therefore better measuring the complete (AGN1+AGN2) super massive BH mass function up to $z \sim 2.5$.

Thus we have applyed the SE Paβ $-L_{14-195keV}$ relation to the 13 AGN with broad permitted emission line identification ad we have derived for the first time a virial BH mass estimate for all these sources. We have found that they have on average BH masses 0.8 dex smaller than AGN1 having the same intrinsic hard X-ray luminosity (in the range 43.2< $\log L_{14-195keV}$ <44 erg s^{-1}), in particular AGN1 shows an average BH mass of logM$_{BH}$=7.60±0.1 M$_{\odot}$, while our AGN2 show an average BH mass of logM_{BH}=6.80±0.2 M$_{\odot}$. Moreover, in the $L_{bol} - L_{Edd}$ plane, the AGN2 show higher Eddington ratios with respect to the AGN1 population of the same luminosity and some of them result to be super-Eddington. These results suggest that AGN2 populate a different region in the $M_{BH} - L$ plane with respect the AGN1 population, sampling lower BH masses and luminosities and for this reason they should be properly taken into account to derive the SMBHMF.

8.0.1 Future applications

A reliable virial BH mass estimator able to work also with AGN2 and low luminosity AGN is an useful tools to accurately investigate the characteristics of the obscured AGN population. In the following we will describe some of the applications of our methods that we wish to carry out in the future.

The local density of low mass BH. Different studies have shown that AGN2 are representative of a population of AGN with low intrinsic X-ray luminosity and low BH masses (Tueller et al., 2010) that likely contains clues about the formation of the first BHs. Thus, the measure of the their local density can be used to discriminate between different models for seeds BH.

The AGN2 $L_{bol} - L_{Edd}$ plane. As, on average, we have found smaller BH masses and larger Eddington ratios in AGN2, we are also interested in observing those objects having the highest luminosities, which have been not observed so far, and which are therefore likely to have the largest Eddington ratios. Therefore, we have asked observing time at Xshooter/VLT to measure the BH masses of the most luminous ($\log L_X$= 44−45 erg s^{-1}) AGN2 in our *Swift* sample and thus to complete the coverage of the luminosity range (3 dex).

The AGN2 scaling relationships. In order to verify the validity of the BH−bulge galaxy properties also for AGN2, we are actually performing 2D bulge−disc decompositions of Spitzer/IRAC 3.6 μm images of our sources with virial BH mass estimates. This method will allow us to obtain an accurate estimate of the hosting galaxy bulge L$_K$ for the 13 AGN2 and thus to derive their $M_{BH} - L_K$ scaling relation to be compare with the one found for AGN1 populations. Similarly, following the work of Riffel et al. (2013), we will use the emission line profile of the NIR [Fe ii] λ12570 Å as an indicator of the stellar velocity dispertion ($\sigma_\star$) in order to derive the $M_{BH} - \sigma_\star$ for the subsample of 13 AGN2 with virial M_{BH} and will also compare it with the one for AGN1.

Finally these NIR SE estimators will be applyied in the framework of demographics studies that suffer for the AGN2 bias. Thus it will be possible to derive for the first time the SMBHMF also for obscured and low luminosity AGNs and compare it with the one found for AGN1, in order to accurately constrain the accretion history of AGNs.

Bibliography

Abramowicz, M. A. and Fragile, P. C. (2013), "Foundations of Black Hole Accretion Disk Theory," *Living Reviews in Relativity*, 16, 1.

Allen, M. G., Dopita, M. A., Tsvetanov, Z. I., and Sutherland, R. S. (1999), "Physical Conditions in the Seyfert Galaxy NGC 2992," *ApJ*, 511, 686–708.

Antonucci, R. (1993), "Unified models for active galactic nuclei and quasars," *Annual Review of Astronomy and Astrophysics*, 31, 473–521.

Balestra, I., Bianchi, S., and Matt, G. (2004), "The reprocessing features in the X-ray spectrum of the NELG MCG -5-23-16," *A&A*, 415, 437–442.

Bassani, L., Malizia, A., Molina, M., Dean, A. J., Ubertini, P., Bazzano, A., Walter, R., Lebrun, F., and Laurent, P. (2005), "Candidate AGN in the 2nd IBIS/ISGRI survey catalogue," *The Astronomer's Telegram*, 537, 1.

Baumgartner, W. H., Tueller, J., Markwardt, C. B., Skinner, G. K., Barthelmy, S., Mushotzky, R. F., Evans, P. A., and Gehrels, N. (2013), "The 70 Month Swift-BAT All-sky Hard X-Ray Survey," *ApJS*, 207, 19.

Beckmann, V., Courvoisier, T. J.-L., Gehrels, N., Lubiński, P., Malzac, J., Petrucci, P.-O., Shrader, C. R., and Soldi, S. (2008), "The efficient low-mass Seyfert MCG-05-23-016," *A&A*, 492, 93–99.

Beckmann, V., Soldi, S., Ricci, C., Alfonso-Garzón, J., Courvoisier, T. J.-L., Domingo, A., Gehrels, N., Lubiński, P., Mas-Hesse, J. M., and Zdziarski, A. A. (2009), "The second INTEGRAL AGN catalogue," *A&A*, 505, 417–439.

Bentz, M. C., Peterson, B. M., Pogge, R. W., Vestergaard, M., and Onken, C. A. (2006), "The Radius-Luminosity Relationship for Active Galactic Nuclei: The Effect of Host-Galaxy Starlight on Luminosity Measurements," *ApJ*, 644, 133–142.

Bentz, M. C., Peterson, B. M., Pogge, R. W., and Vestergaard, M. (2009), "The Black Hole Mass-Bulge Luminosity Relationship for Active Galactic Nuclei From Reverberation Mapping and Hubble Space Telescope Imaging," *ApJ*, 694, L166–L170.

Bian, W. and Gu, Q. (2007), "The Eddington Ratios in Seyfert 2 Galaxies with and without Hidden Broad-Line Regions," *ApJ*, 657, 159–166.

Boisson, C., Coupé, S., Cuby, J. G., Joly, M., and Ward, M. J. (2002), "Near IR spectroscopy of active galactic nuclei," *A&A*, 396, 489–501.

Bongiorno, A., Maiolino, R., Brusa, M., Marconi, A., Piconcelli, E., Lamastra, A., Cano-Diaz, M., Schulze, A., Magnelli, B., Vignali, C., Fiore, F., Menci, N., Cresci, G., La Franca, F., and Merloni, A. (2014), "The M_BH - M_star relation for X-ray obscured, red QSOs at 1.2< z <2.6," *ArXiv e-prints*.

Bower, R. G., Benson, A. J., Malbon, R., Helly, J. C., Frenk, C. S., Baugh, C. M., Cole, S., and Lacey, C. G. (2006), "Breaking the hierarchy of galaxy formation," *MNRAS*, 370, 645–655.

Boyle, B. J. and Terlevich, R. J. (1998), "The cosmological evolution of the QSO luminosity density and of the star formation rate," *MNRAS*, 293, L49–L51.

Braito, V., Reeves, J. N., Dewangan, G., George, I., Griffiths, R., Markowitz, A., Nandra, K., Porquet, D., Ptak, A., Turner, T. J., Yaqoob, T., and Weaver, K. (2006), "The iron emission line complex of MCG-5-23-16: the long XMM-Newton look," *Astronomische Nachrichten*, 327, 1067.

Brenneman, L. W., Risaliti, G., Elvis, M., and Nardini, E. (2013), "An examination of the spectral variability in NGC 1365 with Suzaku," *MNRAS*, 429, 2662–2676.

Buta, R. and Purcell, G. B. (1998), "NGC 3081 - Surface photometry and kinematics of a classic resonance ring barred galaxy," *AJ*, 115, 484.

Byrd, G. G., Freeman, T., and Buta, R. J. (2006), "The Inner Resonance Ring of NGC 3081. II. Star Formation, Bar Strength, Disk Surface Mass Density, and Mass-to-Light Ratio," *AJ*, 131, 1377–1393.

Cai, H.-B., Shu, X.-W., Zheng, Z.-Y., and Wang, J.-X. (2010), "The study of Seyfert 2 galaxies with and without infrared broad lines," *Research in Astronomy and Astrophysics*, 10, 427–437.

Calderone, G., Ghisellini, G., Colpi, M., and Dotti, M. (2012), "B2 0954+25A: a typical Fermi blazar or a γ-ray loud Narrow Line Seyfert 1," *MNRAS*, 424, 3081–3093.

Cattaneo, A., Faber, S. M., Binney, J., Dekel, A., Kormendy, J., Mushotzky, R., Babul, A., Best, P. N., Brüggen, M., Fabian, A. C., Frenk, C. S., Khalatyan, A., Netzer, H., Mahdavi, A., Silk, J., Steinmetz, M., and Wisotzki, L. (2009), "The role of black holes in galaxy formation and evolution," *Nature*, 460, 213–219.

Chapman, S. C., Morris, S. L., Alonso-Herrero, A., and Falcke, H. (2000), "Adaptive optics near-infrared imaging of NGC 2992 - unveiling core structures related to radio figure-of-8 loops," *MNRAS*, 314, 263–272.

Cid Fernandes, R., Heckman, T., Schmitt, H., González Delgado, R. M., and Storchi-Bergmann, T. (2001), "Empirical Diagnostics of the Starburst-AGN Connection," *ApJ*, 558, 81–108.

Colina, L., Fricke, K. J., Kollatschny, W., and Perryman, M. A. C. (1987), "Extended emission line regions in nearby Seyfert galaxies. I - NGC 2992," *A&A*, 178, 51–61.

Connolly, S. D., McHardy, I. M., and Dwelly, T. (2014), "Long-term wind-driven X-ray spectral variability of NGC 1365 with Swift," *MNRAS*, 440, 3503–3510.

Cowie, L. L., Songaila, A., Hu, E. M., and Cohen, J. G. (1996), "New Insight on Galaxy Formation and Evolution From Keck Spectroscopy of the Hawaii Deep Fields," *AJ*, 112, 839.

Croton, D. J., Springel, V., White, S. D. M., De Lucia, G., Frenk, C. S., Gao, L., Jenkins, A., Kauffmann, G., Navarro, J. F., and Yoshida, N. (2006), "The many lives of active galactic nuclei: cooling flows, black holes and the luminosities and colours of galaxies," *MNRAS*, 365, 11–28.

de Grijp, M. H. K., Keel, W. C., Miley, G. K., Goudfrooij, P., and Lub, J. (1992), "Warm IRAS sources. II - Optical spectroscopy of objects from the point source catalog," *A&A*, 96, 389–428.

Denney, K. D., Peterson, B. M., Dietrich, M., Vestergaard, M., and Bentz, M. C. (2009), "Systematic Uncertainties in Black Hole Masses Determined from Single-Epoch Spectra," *ApJ*, 692, 246–264.

Denney, K. D., Peterson, B. M., Pogge, R. W., Adair, A., Atlee, D. W., Au-Yong, K., Bentz, M. C., Bird, J. C., Brokofsky, D. J., Chisholm, E., Comins, M. L., Dietrich, M., and Doroshenko, V. T. (2010), "Reverberation Mapping Measurements of Black Hole Masses in Six Local Seyfert Galaxies," *ApJ*, 721, 715–737.

Dewangan, G. C. and Griffiths, R. E. (2005), "Type 2 Counterparts of Narrow-Line Seyfert 1 Galaxies," *ApJ*, 625, L31–L34.

Di Matteo, T., Springel, V., and Hernquist, L. (2005), "Energy input from quasars regulates the growth and activity of black holes and their host galaxies," *Nature*, 433, 604–607.

Dibai, E. A. (1977), "Mass of the central bodies of active galaxy nuclei," *Soviet Astronomy Letters*, 3, 1–3.

Dietrich, M. and Hamann, F. (2004), "Implications of Quasar Black Hole Masses at High Redshifts," *ApJ*, 611, 761–769.

Dong, R., Greene, J. E., and Ho, L. C. (2012), "X-Ray Properties of Intermediate-mass Black Holes in Active Galaxies. III. Spectral Energy Distribution and Possible Evidence for Intrinsically X-Ray-weak Active Galactic Nuclei," *ApJ*, 761, 73.

Dong, X. Y. and De Robertis, M. M. (2006), "Low-Luminosity Active Galaxies and Their Central Black Holes," *AJ*, 131, 1236–1252.

Ebrero, J., Carrera, F. J., Page, M. J., Silverman, J. D., Barcons, X., Ceballos, M. T., Corral, A., Della Ceca, R., and Watson, M. G. (2009), “The XMM-Newton serendipitous survey. VI. The X-ray luminosity function,” *A&A*, 493, 55–69.

Ebrero, J., Costantini, E., Kaastra, J. S., de Marco, B., and Dadina, M. (2011), “Probing the unified model in NGC 7314,” *A&A*, 535, A62.

Edri, H., Rafter, S. E., Chelouche, D., Kaspi, S., and Behar, E. (2012), “Broad-band Photometric Reverberation Mapping of NGC 4395,” *ApJ*, 756, 73.

Eguchi, S., Ueda, Y., Awaki, H., Aird, J., Terashima, Y., and Mushotzky, R. (2011), “Suzaku View of the Swift/BAT Active Galactic Nuclei. III. Application of Numerical Torus Models to Two Nearly Compton Thick Active Galactic Nuclei (NGC 612 and NGC 3081),” *ApJ*, 729, 31.

Fabian, A. C. and Iwasawa, K. (1999), “The mass density in black holes inferred from the X-ray background,” *MNRAS*, 303, L34–L36.

Falco, E. E., Kurtz, M. J., Geller, M. J., Huchra, J. P., Peters, J., Berlind, P., Mink, D. J., Tokarz, S. P., and Elwell, B. (1999), “The Updated Zwicky Catalog (UZC),” *PASP*, 111, 438–452.

Ferrarese, L. and Merritt, D. (2000), “A Fundamental Relation between Supermassive Black Holes and Their Host Galaxies,” *ApJ*, 539, L9–L12.

Filippenko, A. V. and Ho, L. C. (2003), “A Low-Mass Central Black Hole in the Bulgeless Seyfert 1 Galaxy NGC 4395,” *ApJ*, 588, L13–L16.

Filippenko, A. V. and Sargent, W. L. W. (1989), “Discovery of an extremely low luminosity Seyfert 1 nucleus in the dwarf galaxy NGC 4395,” *ApJ*, 342, L11–L14.

Filippenko, A. V., Ho, L. C., and Sargent, W. L. W. (1993), “HST observations of NGC 4395, the least luminous Seyfert 1 nucleus - Evidence against the starburst hypothesis for broad-lined active galactic nuclei,” *ApJ*, 410, L75–L78.

Franceschini, A., Hasinger, G., Miyaji, T., and Malquori, D. (1999), "On the relationship between galaxy formation and quasar evolution," *MNRAS*, 310, L5–L9.

Fraquelli, H. A., Storchi-Bergmann, T., and Levenson, N. A. (2003), "Extended gas in Seyfert 2 galaxies: implications for the nuclear source," *MNRAS*, 341, 449–463.

Friedrich, S., Davies, R. I., Hicks, E. K. S., Engel, H., Müller-Sánchez, F., Genzel, R., and Tacconi, L. J. (2010), "Adaptive optics near infrared integral field spectroscopy of NGC 2992," *A&A*, 519, A79.

Gebhardt, K., Bender, R., Bower, G., Dressler, A., Faber, S. M., Filippenko, A. V., Green, R., Grillmair, C., Ho, L. C., Kormendy, J., Lauer, T. R., Magorrian, J., Pinkney, J., Richstone, D., and Tremaine, S. (2000), "A Relationship between Nuclear Black Hole Mass and Galaxy Velocity Dispersion," *ApJ*, 539, L13–L16.

Georgakakis, A., Coil, A. L., Laird, E. S., Griffith, R. L., Nandra, K., Lotz, J. M., Pierce, C. M., Cooper, M. C., Newman, J. A., and Koekemoer, A. M. (2009), "Host galaxy morphologies of X-ray selected AGN: assessing the significance of different black hole fuelling mechanisms to the accretion density of the Universe at z ˜ 1." *MNRAS*, 397, 623–633.

Giacconi, R., Gursky, H., Paolini, F. R., and Rossi, B. B. (1962), "Evidence for x Rays From Sources Outside the Solar System," *Physical Review Letters*, 9, 439–443.

Gilli, R., Maiolino, R., Marconi, A., Risaliti, G., Dadina, M., Weaver, K. A., and Colbert, E. J. M. (2000), "The variability of the Seyfert galaxy NGC 2992: the case for a revived AGN," *A&A*, 355, 485–498.

Gilli, R., Comastri, A., and Hasinger, G. (2007), "The synthesis of the cosmic X-ray background in the Chandra and XMM-Newton era," *A&A*, 463, 79–96.

Glass, I. S. (1997), "Variability of Seyfert galaxies in the near-infrared. I - an outburst in NGC 2992," *MNRAS*, 292, L50–L54.

Glikman, E., Helfand, D. J., and White, R. L. (2006), “A Near-Infrared Spectral Template for Quasars,” *ApJ*, 640, 579–591.

Goodrich, R. W., Veilleux, S., and Hill, G. J. (1994), “Infrared spectroscopy of Seyfert 2 galaxies: A look through the obscuring Torus?” *ApJ*, 422, 521–536.

Graham, A. W. (2008), “Populating the Galaxy Velocity Dispersion - Supermassive Black Hole Mass Diagram: A Catalogue of (M_{bh}, σ) Values,” *PASA*, 25, 167–175.

Graham, A. W. and Scott, N. (2013), “The M $_{BH}$-L $_{spheroid}$ Relation at High and Low Masses, the Quadratic Growth of Black Holes, and Intermediate-mass Black Hole Candidates,” *ApJ*, 764, 151.

Graham, A. W., Onken, C. A., Athanassoula, E., and Combes, F. (2011), “An expanded M_{bh}-σ diagram, and a new calibration of active galactic nuclei masses,” *MNRAS*, 412, 2211–2228.

Granato, G. L., Silva, L., Monaco, P., Panuzzo, P., Salucci, P., De Zotti, G., and Danese, L. (2001), “Joint formation of QSOs and spheroids: QSOs as clocks of star formation in spheroids,” *MNRAS*, 324, 757–768.

Granato, G. L., De Zotti, G., Silva, L., Bressan, A., and Danese, L. (2004), “A Physical Model for the Coevolution of QSOs and Their Spheroidal Hosts,” *ApJ*, 600, 580–594.

Greene, J. E. (2012), “Low-mass black holes as the remnants of primordial black hole formation,” *Nature Communications*, 3.

Greene, J. E. and Ho, L. C. (2005a), “A Comparison of Stellar and Gaseous Kinematics in the Nuclei of Active Galaxies,” *ApJ*, 627, 721–732.

Greene, J. E. and Ho, L. C. (2005b), “Estimating Black Hole Masses in Active Galaxies Using the Hα Emission Line,” *ApJ*, 630, 122–129.

Greene, J. E. and Ho, L. C. (2007a), “A New Sample of Low-Mass Black Holes in Active Galaxies,” *ApJ*, 670, 92–104.

Greene, J. E. and Ho, L. C. (2007b), “The Mass Function of Active Black Holes in the Local Universe,” *ApJ*, 667, 131–148.

Greene, J. E., Hood, C. E., Barth, A. J., Bennert, V. N., Bentz, M. C., Filippenko, A. V., Gates, E., Malkan, M. A., Treu, T., Walsh, J. L., and Woo, J.-H. (2010), "The Lick AGN Monitoring Project: Alternate Routes to a Broad-line Region Radius," *ApJ*, 723, 409–416.

Grier, C. J., Martini, P., Watson, L. C., Peterson, B. M., Bentz, M. C., Dasyra, K. M., Dietrich, M., Ferrarese, L., Pogge, R. W., and Zu, Y. (2013), "Stellar Velocity Dispersion Measurements in High-luminosity Quasar Hosts and Implications for the AGN Black Hole Mass Scale," *ApJ*, 773, 90.

Grupe, D., Wills, B. J., Leighly, K. M., and Meusinger, H. (2004), "A Complete Sample of Soft X-Ray-Selected AGNs. I. The Data," *AJ*, 127, 156–179.

Guainazzi, M., Matt, G., Fiore, F., and Perola, G. C. (2002), "The Phoenix galaxy: UGC 4203 re-birth from its ashes?" *A&A*, 388, 787–792.

Hasinger, G. (2008), "Absorption properties and evolution of active galactic nuclei," *A&A*, 490, 905–922.

Hasinger, G., Miyaji, T., and Schmidt, M. (2005), "Luminosity-dependent evolution of soft X-ray selected AGN. New Chandra and XMM-Newton surveys," *A&A*, 441, 417–434.

Hawkins, M. R. S. (2004), "Naked active galactic nuclei," *A&A*, 424, 519–529.

Heckman, T. M., Miley, G. K., van Breugel, W. J. M., and Butcher, H. R. (1981), "Emission-line profiles and kinematics of the narrow-line region in Seyfert and radio galaxies," *ApJ*, 247, 403–418.

Heckman, T. M., Kauffmann, G., Brinchmann, J., Charlot, S., Tremonti, C., and White, S. D. M. (2004), "Present-Day Growth of Black Holes and Bulges: The Sloan Digital Sky Survey Perspective," *ApJ*, 613, 109–118.

Heisler, C. A. and De Robertis, M. M. (1999), "A Near-Infrared Spectroscopic Study of 60 Micron Peakers," *AJ*, 118, 2038–2054.

Hes, R., Barthel, P. D., and Hoekstra, H. (1995), "The far infrared properties of 3CR quasars and radio galaxies." *A&A*, 303, 8.

Hicks, E. K. S. and Malkan, M. A. (2008), “Circumnuclear Gas in Seyfert 1 Galaxies: Morphology, Kinematics, and Direct Measurement of Black Hole Masses,” *ApJS*, 174, 31–73.

Ho, L. C. and Peng, C. Y. (2001), “Nuclear Luminosities and Radio Loudness of Seyfert Nuclei,” *ApJ*, 555, 650–662.

Ho, L. C., Filippenko, A. V., and Sargent, W. L. W. (1993), “A Reevaluation of the Excitation Mechanism of LINERs,” *ApJ*, 417, 63.

Ho, L. C., Filippenko, A. V., and Sargent, W. L. (1995), “A search for ’dwarf’ Seyfert nuclei. 2: an optical spectral atlas of the nuclei of nearby galaxies,” *ApJS*, 98, 477–593.

Ho, L. C., Feigelson, E. D., Townsley, L. K., Sambruna, R. M., Garmire, G. P., Brandt, W. N., Filippenko, A. V., Griffiths, R. E., Ptak, A. F., and Sargent, W. L. W. (2001), “Detection of Nuclear X-Ray Sources in Nearby Galaxies with Chandra,” *ApJ*, 549, L51–L54.

Horne, K., Peterson, B. M., Collier, S. J., and Netzer, H. (2004), “Observational Requirements for High-Fidelity Reverberation Mapping,” *PASP*, 116, 465–476.

Iwasawa, K., Fabian, A. C., Almaini, O., Lira, P., Lawrence, A., Hayashida, K., and Inoue, H. (2000), “X-ray absorption and rapid variability of the dwarf Seyfert nucleus of NGC 4395,” *MNRAS*, 318, 879–888.

Jones, D. H., Read, M. A., Saunders, W., Colless, M., Jarrett, T., Parker, Q. A., Fairall, A. P., Mauch, T., Sadler, E. M., Watson, F. G., Burton, D., Campbell, L. A., Cass, P., Croom, S. M., Dawe, J., Fiegert, K., Frankcombe, L., Hartley, M., Huchra, J., James, D., Kirby, E., Lahav, O., Lucey, J., Mamon, G. A., Moore, L., Peterson, B. A., Prior, S., Proust, D., Russell, K., Safouris, V., Wakamatsu, K.-I., Westra, E., and Williams, M. (2009), “The 6dF Galaxy Survey: final redshift release (DR3) and southern large-scale structures,” *MNRAS*, 399, 683–698.

Kaspi, S., Smith, P. S., Netzer, H., Maoz, D., Jannuzi, B. T., and Giveon, U. (2000), “Reverberation Measurements for 17 Quasars and the Size-Mass-Luminosity Relations in Active Galactic Nuclei,” *ApJ*, 533, 631–649.

Kaspi, S., Maoz, D., Netzer, H., Peterson, B. M., Vestergaard, M., and Jannuzi, B. T. (2005), “The Relationship between Luminosity and Broad-Line Region Size in Active Galactic Nuclei,” *ApJ*, 629, 61–71.

Keel, W. C., de Grijp, M. H. K., Miley, G. K., and Zheng, W. (1994), “Warm IRAS Sources from the Point Source Catalog - Part Three - Emission Line Properties Correlations and AGN / Active Galactic Nuclei / Unified Models,” *A&A*, 283, 791.

Kelly, B. C., Vestergaard, M., and Fan, X. (2009), “Determining Quasar Black Hole Mass Functions from their Broad Emission Lines: Application to the Bright Quasar Survey,” *ApJ*, 692, 1388–1410.

Kelly, B. C., Vestergaard, M., Fan, X., Hopkins, P., Hernquist, L., and Siemiginowska, A. (2010), “Constraints on Black Hole Growth, Quasar Lifetimes, and Eddington Ratio Distributions from the SDSS Broad-line Quasar Black Hole Mass Function,” *ApJ*, 719, 1315–1334.

Kim, D., Im, M., and Kim, M. (2010), “New Estimators of Black Hole Mass in Active Galactic Nuclei with Hydrogen Paschen Lines,” *ApJ*, 724, 386–399.

Koratkar, A. and Blaes, O. (1999), “The Ultraviolet and Optical Continuum Emission in Active Galactic Nuclei: The Status of Accretion Disks,” *PASP*, 111, 1–30.

Koribalski, B. and Dickey, J. M. (2004), “Neutral hydrogen gas in interacting galaxies: the NGC 6221/6215 galaxy group,” *MNRAS*, 348, 1255–1274.

Kormendy, J. and Richstone, D. (1995), “Inward Bound—The Search For Supermassive Black Holes In Galactic Nuclei,” *Annual Review of Astronomy and Astrophysics*, 33, 581.

Kormendy, J., Bender, R., and Cornell, M. E. (2011), “Supermassive black holes do not correlate with galaxy disks or pseudobulges,” *Nature*, 469, 374–376.

Krolik, J. H. (1998), *Active Galactic Nuclei: From the Central Black Hole to the Galactic Environment.*

La Franca, F., Fiore, F., Comastri, A., Perola, G. C., Sacchi, N., Brusa, M., Cocchia, F., Feruglio, C., Matt, G., Vignali, C., Carangelo, N., Ciliegi, P., Lamastra, A., Maiolino, R., Mignoli, M., Molendi, S., and Puccetti, S. (2005), "The HELLAS2XMM Survey. VII. The Hard X-Ray Luminosity Function of AGNs up to z = 4: More Absorbed AGNs at Low Luminosities and High Redshifts," *ApJ*, 635, 864–879.

Landt, H., Bentz, M. C., Ward, M. J., Elvis, M., Peterson, B. M., Korista, K. T., and Karovska, M. (2008), "The Near-Infrared Broad Emission Line Region of Active Galactic Nuclei. I. The Observations," *ApJS*, 174, 282–312.

Landt, H., Elvis, M., Ward, M. J., Bentz, M. C., Korista, K. T., and Karovska, M. (2011), "The near-infrared broad emission line region of active galactic nuclei - II. The 1-μm continuum," *MNRAS*, 414, 218–240.

Landt, H., Ward, M. J., Peterson, B. M., Bentz, M. C., Elvis, M., Korista, K. T., and Karovska, M. (2013), "A near-infrared relationship for estimating black hole masses in active galactic nuclei," *MNRAS*, 432, 113–126.

Levenson, N. A., Cid Fernandes, Jr., R., Weaver, K. A., Heckman, T. M., and Storchi-Bergmann, T. (2001), "The Obscuring Starburst of NGC 6221 and Implications for the Hard X-Ray Background," *ApJ*, 557, 54–66.

Lusso, E., Comastri, A., Simmons, B. D., Mignoli, M., Zamorani, G., Vignali, C., Brusa, M., Shankar, F., Lutz, D., Trump, J. R., Maiolino, R., Gilli, R., Bolzonella, M., Puccetti, S., Salvato, M., Impey, C. D., Civano, F., Elvis, M., Mainieri, V., Silverman, J. D., Koekemoer, A. M., Bongiorno, A., Merloni, A., Berta, S., Le Floc'h, E., Magnelli, B., Pozzi, F., and Riguccini, L. (2012), "Bolometric luminosities and Eddington ratios of X-ray selected active galactic nuclei in the XMM-COSMOS survey," *MNRAS*, 425, 623–640.

Madau, P., Ferguson, H. C., Dickinson, M. E., Giavalisco, M., Steidel, C. C., and Fruchter, A. (1996), "High-redshift galaxies in the Hubble Deep Field: colour selection and star formation history to z˜4," *MNRAS*, 283, 1388–1404.

Magorrian, J., Tremaine, S., Richstone, D., Bender, R., Bower, G., Dressler, A., Faber, S. M., Gebhardt, K., Green, R., Grillmair, C., Kormendy, J., and Lauer, T. (1998), "The Demography of Massive Dark Objects in Galaxy Centers," *AJ*, 115, 2285–2305.

Maiolino, R., Rieke, G. H., and Rieke, M. J. (1996), "Correction of the Atmospheric Transmission in Infrared Spectroscopy," *AJ*, 111, 537.

Maiolino, R., Salvati, M., Bassani, L., Dadina, M., della Ceca, R., Matt, G., Risaliti, G., and Zamorani, G. (1998), "Heavy obscuration in X-ray weak AGNs," *A&A*, 338, 781–794.

Maiolino, R., Risaliti, G., Salvati, M., Pietrini, P., Torricelli-Ciamponi, G., Elvis, M., Fabbiano, G., Braito, V., and Reeves, J. (2010), ""Comets" orbiting a black hole," *A&A*, 517, A47.

Malizia, A., Bassani, L., Zhang, S. N., Dean, A. J., Paciesas, W. S., and Palumbo, G. G. C. (1999), "BATSE Observations of the Piccinotti Sample of Active Galactic Nuclei," *ApJ*, 519, 637–641.

Malizia, A., Malaguti, G., Bassani, L., Cappi, M., Comastri, A., Di Cocco, G., Palazzi, E., and Vignali, C. (2002), "BeppoSAX/PDS identification of the true counterpart of the Piccinotti source H0917-074," *A&A*, 394, 801–805.

Marconi, A. and Hunt, L. K. (2003), "The Relation between Black Hole Mass, Bulge Mass, and Near-Infrared Luminosity," *ApJ*, 589, L21–L24.

Marconi, A., Risaliti, G., Gilli, R., Hunt, L. K., Maiolino, R., and Salvati, M. (2004), "Local supermassive black holes, relics of active galactic nuclei and the X-ray background," *MNRAS*, 351, 169–185.

Marquez, I., Boisson, C., Durret, F., and Petitjean, P. (1998), "A kinematical analysis of NGC 2992," *A&A*, 333, 459–465.

Masetti, N., Pretorius, M. L., Palazzi, E., Bassani, L., Bazzano, A., Bird, A. J., Charles, P. A., Dean, A. J., Malizia, A., Nkundabakura, P., Stephen, J. B., and Ubertini, P. (2006), "Unveiling the nature of INTEGRAL objects through optical spectroscopy. III. Observations of seven southern sources," *A&A*, 449, 1139–1149.

Mathez, G. (1976), "Evolution of the luminosity function of quasars - A model with constant density and luminosity evolution," *A&A*, 53, 15–21.

Matsuta, K., Gandhi, P., Dotani, T., Nakagawa, T., Isobe, N., Ueda, Y., Ichikawa, K., Terashima, Y., Oyabu, S., Yamamura, I., and Stawarz, Ł. (2012), "Infrared and Hard X-Ray Diagnostics of Active Galactic Nucleus Identification from the Swift/BAT and AKARI All-sky Surveys," *ApJ*, 753, 104.

Mattson, B. J. and Weaver, K. A. (2004), "RXTE and BeppoSAX Observations of MCG -5-23-16: Reflection from Distant Cold Material," *ApJ*, 601, 771–777.

Mazzalay, X. and Rodríguez-Ardila, A. (2007), "Optical and NIR spectroscopy of Mrk 1210: constraints and physical conditions of the active nucleus," *A&A*, 463, 445–454.

McLure, R. J. and Jarvis, M. J. (2002), "Measuring the black hole masses of high-redshift quasars," *MNRAS*, 337, 109–116.

McNamara, B. R., Wise, M., Nulsen, P. E. J., David, L. P., Sarazin, C. L., Bautz, M., Markevitch, M., Vikhlinin, A., Forman, W. R., Jones, C., and Harris, D. E. (2000), "Chandra X-Ray Observations of the Hydra A Cluster: An Interaction between the Radio Source and the X-Ray-emitting Gas," *ApJ*, 534, L135–L138.

Menci, N., Fiore, F., Perola, G. C., and Cavaliere, A. (2004), "X-Ray Evolution of Active Galactic Nuclei and Hierarchical Galaxy Formation," *ApJ*, 606, 58–66.

Menci, N., Fontana, A., Giallongo, E., and Salimbeni, S. (2005), "Bimodal Color Distribution in Hierarchical Galaxy Formation," *ApJ*, 632, 49–57.

Menci, N., Fiore, F., Puccetti, S., and Cavaliere, A. (2008), "The Blast Wave Model for AGN Feedback: Effects on AGN Obscuration," *ApJ*, 686, 219–229.

Merloni, A. and Heinz, S. (2008), "A synthesis model for AGN evolution: supermassive black holes growth and feedback modes," *MNRAS*, 388, 1011–1030.

Merloni, A. and Heinz, S. (2013), *Evolution of Active Galactic Nuclei*, p. 503.

Merloni, A., Bongiorno, A., Bolzonella, M., Brusa, M., Civano, F., Comastri, A., Elvis, M., Fiore, F., and et al., . (2010), "On the Cosmic Evolution of the Scaling Relations Between Black Holes and Their Host Galaxies: Broad-Line Active Galactic Nuclei in the zCOSMOS Survey," *ApJ*, 708, 137–157.

Middleton, M., Done, C., and Schurch, N. (2008), "High-energy X-ray spectra of Seyferts and Unification schemes for active galactic nuclei," *MNRAS*, 383, 1501–1505.

Moran, E. C., Filippenko, A. V., Ho, L. C., Shields, J. C., Belloni, T., Comastri, A., Snowden, S. L., and Sramek, R. A. (1999), "The Nuclear Spectral Energy Distribution of NGC 4395, the Least Luminous Type 1 Seyfert Galaxy," *PASP*, 111, 801–808.

Moran, E. C., Barth, A. J., Kay, L. E., and Filippenko, A. V. (2000), "The Frequency of Polarized Broad Emission Lines in Type 2 Seyfert Galaxies," *ApJ*, 540, L73–L77.

Mullaney, J. R., Alexander, D. M., Goulding, A. D., and Hickox, R. C. (2011), "Defining the intrinsic AGN infrared spectral energy distribution and measuring its contribution to the infrared output of composite galaxies," *MNRAS*, 414, 1082–1110.

Netzer, H. and Laor, A. (1993), "Dust in the narrow-line region of active galactic nuclei," *ApJ*, 404, L51–L54.

Netzer, H. and Peterson, B. M. (1997), "Reverberation Mapping and the Physics of Active Galactic Nuclei," in *Astronomical Time Series*, eds. D. Maoz, A. Sternberg, and E. M. Leibowitz, vol. 218 of *Astrophysics and Space Science Library*, p. 85.

Onken, C. A., Ferrarese, L., Merritt, D., Peterson, B. M., Pogge, R. W., Vestergaard, M., and Wandel, A. (2004), "Supermassive Black Holes in Active Galactic Nuclei. II. Calibration of the Black Hole Mass-Velocity Dispersion Relationship for Active Galactic Nuclei," *ApJ*, 615, 645–651.

Onken, C. A., Valluri, M., Peterson, B. M., Pogge, R. W., Bentz, M. C., Ferrarese, L., Vestergaard, M., Crenshaw, D. M., Sergeev, S. G., McHardy, I. M., Merritt, D., Bower, G. A., Heckman, T. M., and Wandel, A. (2007), "The Black Hole Mass of NGC 4151: Comparison of Reverberation Mapping and Stellar Dynamical Measurements," *ApJ*, 670, 105–115.

Panessa, F., Bassani, L., Cappi, M., Dadina, M., Barcons, X., Carrera, F. J., Ho, L. C., and Iwasawa, K. (2006), "On the X-ray, optical emission line and black hole mass properties of local Seyfert galaxies," *A&A*, 455, 173–185.

Park, C., Choi, Y.-Y., Kim, J., Gott, III, J. R., Kim, S. S., and Kim, K.-S. (2012), "The Challenge of the Largest Structures in the Universe to Cosmology," *ApJ*, 759, L7.

Pence, W. D. and Blackman, C. P. (1984), "Dynamics of gas in barred spiral galaxies. I - NGC 6221," *MNRAS*, 207, 9–23.

Peterson, B. M. (1993), "Reverberation mapping of active galactic nuclei," *PASP*, 105, 247–268.

Peterson, B. M. (1997), "Book Review: An introduction to active galactic nuclei / Cambridge U Press, 1997," *The Observatory*, 117, 314.

Peterson, B. M. (2010), "Masses of Black Holes in Active Galactic Nuclei," in *American Astronomical Society Meeting Abstracts #215*, vol. 42 of *Bulletin of the American Astronomical Society*, p. 373.01.

Peterson, B. M., Bentz, M. C., Desroches, L.-B., Filippenko, A. V., Ho, L. C., Kaspi, S., Laor, A., Maoz, D., Moran, E. C., Pogge, R. W., and Quillen, A. C. (2005), "Multiwavelength Monitoring of the Dwarf Seyfert 1 Galaxy NGC 4395. I. A Reverberation-based Measurement of the Black Hole Mass," *ApJ*, 632, 799–808.

Press, W. H., Teukolsky, S. A., Vetterling, W. T., and Flannery, B. P. (2007), *Numerical recipes: the art of scientific computing, 3rd edn.*, Cambridge Univ. Press, Cambridge.

Ramos Almeida, C., Pérez García, A. M., and Acosta-Pulido, J. A. (2009), "Near-Infrared Spectroscopy of Seyfert Galaxies. Nuclear Activity and Stellar Population," *ApJ*, 694, 1379–1394.

Ramos Almeida, C., Sánchez-Portal, M., Pérez García, A. M., Acosta-Pulido, J. A., Castillo, M., Asensio Ramos, A., González-Serrano, J. I., Alonso-Herrero, A., Rodríguez Espinosa, J. M., Hatziminaoglou, E., Coia, D., Valtchanov, I., Pović, M., Esquej, P., Packham, C., and Altieri, B. (2011), "Resolving the nuclear dust distribution of the Seyfert 2 galaxy NGC 3081," *MNRAS*, 417, L46–L50.

Reeves, J. N., Awaki, H., Dewangan, G. C., Fabian, A. C., Fukazawa, Y., Gallo, L., Griffiths, R., Inoue, H., Kunieda, H., Markowitz, A., Miniutti, G., Mizuno, T., Mushotzky, R., Okajima, T., Ptak, A., Takahashi, T., Terashima, Y., Ushio, M., Watanabe, S., Yamasaki, T., Yamauchi, M., and Yaqoob, T. (2007), "Revealing the High Energy Emission from the Obscured Seyfert Galaxy MCG-5-23-16 with Suzaku," *PASJ*, 59, 301–314.

Riffel, R., Rodríguez-Ardila, A., and Pastoriza, M. G. (2006), "A 0.8-2.4 μm spectral atlas of active galactic nuclei," *A&A*, 457, 61–70.

Riffel, R. A., Storchi-Bergmann, T., Riffel, R., Pastoriza, M. G., Rodríguez-Ardila, A., Dors, O. L., Fuchs, J., Diniz, M. R., Schönell, A. J., Hennig, M. G., and Brum, C. (2013), "A correlation between the stellar and [Fe II] velocity dispersions in active galaxies," *MNRAS*, 429, 2587–2593.

Risaliti, G. and Elvis, M. (2004), "A Panchromatic View of AGN," in *Supermassive Black Holes in the Distant Universe*, ed. A. J. Barger, vol. 308 of *Astrophysics and Space Science Library*, p. 187.

Risaliti, G., Elvis, M., Fabbiano, G., Baldi, A., and Zezas, A. (2005), "Rapid Compton-thick/Compton-thin Transitions in the Seyfert 2 Galaxy NGC 1365," *ApJ*, 623, L93–L96.

Risaliti, G., Elvis, M., Fabbiano, G., Baldi, A., Zezas, A., and Salvati, M. (2007), "Occultation Measurement of the Size of the X-Ray-emitting Region in the Active Galactic Nucleus of NGC 1365," *ApJ*, 659, L111–L114.

Risaliti, G., Miniutti, G., Elvis, M., Fabbiano, G., Salvati, M., Baldi, A., Braito, V., Bianchi, S., Matt, G., Reeves, J., Soria, R., and Zezas, A. (2009), "Variable Partial Covering and A Relativistic Iron Line in NGC 1365," *ApJ*, 696, 160–171.

Risaliti, G., Harrison, F. A., Madsen, K. K., Walton, D. J., Boggs, S. E., Christensen, F. E., Craig, W. W., Grefenstette, B. W., Hailey, C. J., Nardini, E., Stern, D., and Zhang, W. W. (2013), "A rapidly spinning supermassive black hole at the centre of NGC 1365," *Nature*, 494, 449–451.

Rix, H.-W., Rieke, G., Rieke, M., and Carleton, N. P. (1990), "Probing intermediate Seyfert galaxies by Pa(beta) spectroscopy," *ApJ*, 363, 480–487.

Rousselot, P., Lidman, C., Cuby, J.-G., Moreels, G., and Monnet, G. (2000), "Night-sky spectral atlas of OH emission lines in the near-infrared," *A&A*, 354, 1134–1150.

Sani, E., Marconi, A., Hunt, L. K., and Risaliti, G. (2011), "The Spitzer/IRAC view of black hole-bulge scaling relations," *MNRAS*, 413, 1479–1494.

Schmidt, M. (1968), "Space Distribution and Luminosity Functions of Quasi-Stellar Radio Sources," *ApJ*, 151, 393.

Schmitt, H. R., Donley, J. L., Antonucci, R. R. J., Hutchings, J. B., and Kinney, A. L. (2003), "A Hubble Space Telescope Survey of Extended [O III] λ5007 Emission in a Far-Infrared Selected Sample of Seyfert Galaxies: Observations," *ApJS*, 148, 327–352.

Schulz, H., Knake, A., and Schmidt-Kaler, T. (1994), "Long-slit spectroscopy of three low-luminosity Seyfert-1 galaxies," *A&A*, 288, 425–432.

Schulz, H., Komossa, S., Schmitz, C., and Mücke, A. (1999), "Clues on the obscured active nucleus of NGC 1365," *A&A*, 346, 764–768.

Severgnini, P., Caccianiga, A., Della Ceca, R., Moretti, A., Vignali, C., La Parola, V., and Cusumano, G. (2010), "Heavily obscured AGN in the local Universe," *X-ray Astronomy 2009; Present Status, Multi-Wavelength Approach and Future Perspectives*, 1248, 511–512.

Severgnini, P., Caccianiga, A., Della Ceca, R., Braito, V., Vignali, C., La Parola, V., and Moretti, A. (2011), "Suzaku and SWIFT-BAT observations of a newly discovered Compton-thick AGN," *A&A*, 525, A38.

Shakura, N. I. and Sunyaev, R. A. (1973), "Black holes in binary systems. Observational appearance." *A&A*, 24, 337–355.

Shankar, F., Salucci, P., Granato, G. L., De Zotti, G., and Danese, L. (2004), “Supermassive black hole demography: the match between the local and accreted mass functions,” *MNRAS*, 354, 1020–1030.

Shankar, F., Weinberg, D. H., and Miralda-Escudé, J. (2013), “Accretion-driven evolution of black holes: Eddington ratios, duty cycles and active galaxy fractions,” *MNRAS*, 428, 421–446.

Shen, Y. (2013), “The mass of quasars,” *Bulletin of the Astronomical Society of India*, 41, 61–115.

Shen, Y. and Kelly, B. C. (2012), “The Demographics of Broad-line Quasars in the Mass-Luminosity Plane. I. Testing FWHM-based Virial Black Hole Masses,” *ApJ*, 746, 169.

Shen, Y. and Liu, X. (2012), “Comparing Single-epoch Virial Black Hole Mass Estimators for Luminous Quasars,” *ApJ*, 753, 125.

Shih, D. C., Iwasawa, K., and Fabian, A. C. (2003), “Evidence for an intermediate-mass black hole and a multi-zone warm absorber in NGC 4395,” *MNRAS*, 341, 973–980.

Silk, J. and Rees, M. J. (1998), “Quasars and galaxy formation,” *A&A*, 331, L1–L4.

Soifer, B. T., Charmandaris, V., Brandl, B. R., Armus, L., Appleton, P. N., Burgdorf, M. J., Devost, D., Herter, T., Higdon, S. J. U., Higdon, J. L., Houck, J. R., Lawrence, C. R., Morris, P. W., Teplitz, H. I., Uchida, K. I., van Cleve, J., and Weedman, D. (2004), “Spitzer Infrared Spectrograph (IRS) Observations of the Redshift 3.91 Quasar APM 08279+5255,” *ApJS*, 154, 151–154.

Soldi, S., Beckmann, V., Bassani, L., Courvoisier, T. J.-L., Landi, R., Malizia, A., Dean, A. J., de Rosa, A., Fabian, A. C., and Walter, R. (2005), “INTEGRAL observations of six AGN in the Galactic Plane,” *A&A*, 444, 431–441.

Soltan, A. (1982), “Masses of quasars,” *MNRAS*, 200, 115–122.

Storchi-Bergmann, T., Fernandes, R. C., and Schmitt, H. R. (1998), “The Nature of the Optical Light in Seyfert 2 Galaxies with Polarized Continua,” *ApJ*, 501, 94–102.

Strauss, M. A., Huchra, J. P., Davis, M., Yahil, A., Fisher, K. B., and Tonry, J. (1992), “A redshift survey of IRAS galaxies. VII - The infrared and redshift data for the 1.936 Jansky sample,” *ApJS*, 83, 29–63.

Tran, H. D. (1995), “The Nature of Seyfert 2 Galaxies with Obscured Broad-Line Regions. II. Individual Objects,” *ApJ*, 440, 578.

Tran, H. D., Miller, J. S., and Kay, L. E. (1992), “Detection of obscured broad-line regions in four Seyfert 2 galaxies,” *ApJ*, 397, 452–456.

Treister, E. and Urry, C. M. (2005), “Active Galactic Nuclei Unification and the X-Ray Background,” *ApJ*, 630, 115–121.

Treister, E. and Urry, C. M. (2006), “The Evolution of Obscuration in Active Galactic Nuclei,” *ApJ*, 652, L79–L82.

Treister, E., Urry, C. M., and Virani, S. (2009), “The Space Density of Compton-Thick Active Galactic Nucleus and the X-Ray Background,” *ApJ*, 696, 110–120.

Tremaine, S., Gebhardt, K., Bender, R., Bower, G., Dressler, A., Faber, S. M., Filippenko, A. V., Green, R., Grillmair, C., Ho, L. C., Kormendy, J., Lauer, T. R., Magorrian, J., Pinkney, J., and Richstone, D. (2002), “The Slope of the Black Hole Mass versus Velocity Dispersion Correlation,” *ApJ*, 574, 740–753.

Trippe, M. L., Crenshaw, D. M., Deo, R., and Dietrich, M. (2008), “Long-Term Variability in the Optical Spectrum of the Seyfert Galaxy NGC 2992,” *AJ*, 135, 2048–2054.

Trippe, M. L., Crenshaw, D. M., Deo, R. P., Dietrich, M., Kraemer, S. B., Rafter, S. E., and Turner, T. J. (2010), “A Multi-wavelength Study of the Nature of Type 1.8/1.9 Seyfert Galaxies,” *ApJ*, 725, 1749–1767.

Tueller, J., Mushotzky, R. F., Barthelmy, S., Cannizzo, J. K., Gehrels, N., Markwardt, C. B., Skinner, G. K., and Winter, L. M. (2008), "Swift BAT Survey of AGNs," *ApJ*, 681, 113–127.

Tueller, J., Baumgartner, W. H., Markwardt, C. B., Skinner, G. K., Mushotzky, R. F., Ajello, M., Barthelmy, S., Beardmore, A., Brandt, W. N., Burrows, D., Chincarini, G., Campana, S., Cummings, J., Cusumano, G., Evans, P., Fenimore, E., Gehrels, N., Godet, O., Grupe, D., Holland, S., Kennea, J., Krimm, H. A., Koss, M., Moretti, A., Mukai, K., Osborne, J. P., Okajima, T., Pagani, C., Page, K., Palmer, D., Parsons, A., Schneider, D. P., Sakamoto, T., Sambruna, R., Sato, G., Stamatikos, M., Stroh, M., Ukwata, T., and Winter, L. (2010), "The 22 Month Swift-BAT All-Sky Hard X-ray Survey," *ApJS*, 186, 378–405.

Ueda, Y., Akiyama, M., Ohta, K., and Miyaji, T. (2003), "Cosmological Evolution of the Hard X-Ray Active Galactic Nucleus Luminosity Function and the Origin of the Hard X-Ray Background," *ApJ*, 598, 886–908.

Urry, C. M. and Padovani, P. (1995), "Unified Schemes for Radio-Loud Active Galactic Nuclei," *PASP*, 107, 803.

Vacca, W. D., Cushing, M. C., and Rayner, J. T. (2003), "A Method of Correcting Near-Infrared Spectra for Telluric Absorption," *PASP*, 115, 389–409.

Vasudevan, R. V. and Fabian, A. C. (2007), "Piecing together the X-ray background: bolometric corrections for active galactic nuclei," *MNRAS*, 381, 1235–1251.

Vasudevan, R. V., Brandt, W. N., Mushotzky, R. F., Winter, L. M., Baumgartner, W. H., Shimizu, T. T., Schneider, D. P., and Nousek, J. (2013), "X-Ray Properties of the Northern Galactic Cap Sources in the 58 Month Swift/BAT Catalog," *ApJ*, 763, 111.

Veilleux, S., Goodrich, R. W., and Hill, G. J. (1997), "Infrared Spectroscopy of Seyfert 2 Galaxies: A Look through the Obscuring Torus? II." *ApJ*, 477, 631–660.

Veron, P., Lindblad, P. O., Zuiderwijk, E. J., Veron, M. P., and Adam, G. (1980), "On the nature of the so-called narrow-line X-ray galaxies," *A&A*, 87, 245–249.

Véron-Cetty, M.-P. and Véron, P. (2010), "A catalogue of quasars and active nuclei: 13th edition," *A&A*, 518, A10.

Vestergaard, M. (2002), "Determining Central Black Hole Masses in Distant Active Galaxies," *ApJ*, 571, 733–752.

Vestergaard, M. (2004), "Early Growth and Efficient Accretion of Massive Black Holes at High Redshift," *ApJ*, 601, 676–691.

Vestergaard, M. and Osmer, P. S. (2009), "Mass Functions of the Active Black Holes in Distant Quasars from the Large Bright Quasar Survey, the Bright Quasar Survey, and the Color-selected Sample of the SDSS Fall Equatorial Stripe," *ApJ*, 699, 800–816.

Vestergaard, M. and Peterson, B. M. (2006), "Determining Central Black Hole Masses in Distant Active Galaxies and Quasars. II. Improved Optical and UV Scaling Relationships," *ApJ*, 641, 689–709.

Vestergaard, M., Denney, K., Fan, X., Jensen, J. J., Kelly, B. C., Osmer, P. S., Peterson, B. M., and Tremonti, C. A. (2011), "Black hole mass estimations: limitations and uncertainties," in *Narrow-Line Seyfert 1 Galaxies and their Place in the Universe.*

Walton, D. J., Reis, R. C., and Fabian, A. C. (2010), "Explaining the hard excesses in active galactic nuclei," *MNRAS*, 408, 601–606.

Wandel, A. and Mushotzky, R. F. (1986), "Observational determination of the masses of active galactic nuclei," *ApJ*, 306, L61–L65.

Wandel, A., Peterson, B. M., and Malkan, M. A. (1999), "Central Masses and Broad-Line Region Sizes of Active Galactic Nuclei. I. Comparing the Photoionization and Reverberation Techniques," *ApJ*, 526, 579–591.

Wang, J.-M. and Zhang, E.-P. (2007), "The Unified Model of Active Galactic Nuclei. II. Evolutionary Connection," *ApJ*, 660, 1072–1092.

Ward, M., Penston, M. V., Blades, J. C., and Turtle, A. J. (1980), "New optical and radio observations of the X-ray galaxies NGC 7582 and NGC 2992," *MNRAS*, 193, 563–582.

Watanabe, M., Nagata, T., Sato, S., Nakaya, H., and Hough, J. H. (2003), "Simultaneous Optical and Near-Infrared Spectropolarimetry of Type 2 Seyfert Galaxies," *ApJ*, 591, 714–732.

Weaver, K. A., Yaqoob, T., Mushotzky, R. F., Nousek, J., Hayashi, I., and Koyama, K. (1997), "Iron Kα Evidence for Two X-Ray Reprocessors in MCG -5-23-16," *ApJ*, 474, 675–685.

Winter, L. M., Mushotzky, R. F., Reynolds, C. S., and Tueller, J. (2009), "X-Ray Spectral Properties of the BAT AGN Sample," *ApJ*, 690, 1322–1349.

Winter, L. M., Mushotzky, R., Lewis, K., Veilleux, S., Koss, M., and Keeney, B. (2010), "Optical and X-ray Properties of the Swift BAT-detected AGN," *X-ray Astronomy 2009; Present Status, Multi-Wavelength Approach and Future Perspectives*, 1248, 369–372.

Woltjer, L. (1959), "Emission Nuclei in Galaxies." *ApJ*, 130, 38.

Woo, J.-H., Treu, T., Barth, A. J., Wright, S. A., Walsh, J. L., Bentz, M. C., Martini, P., Bennert, V. N., Canalizo, G., Filippenko, A. V., Gates, E., Greene, J., Li, W., Malkan, M. A., Stern, D., and Minezaki, T. (2010), "The Lick AGN Monitoring Project: The M $_{BH}$-σ_* Relation for Reverberation-mapped Active Galaxies," *ApJ*, 716, 269–280.

Yu, Q. and Tremaine, S. (2002), "Observational constraints on growth of massive black holes," *MNRAS*, 335, 965–976.

Zoghbi, A., Reynolds, C., Cackett, E. M., Miniutti, G., Kara, E., and Fabian, A. C. (2013), "Discovery of Fe Kα X-Ray Reverberation around the Black Holes in MCG-5-23-16 and NGC 7314," *ApJ*, 767, 121.

Appendix A

Proposal

Appendix B

List of publications

In this Appendix the list of publications in which I have been involved during my PhD are listed. The papers topics are not strictly related to the main project on which I worked during my Ph.D. thesis.

- F. La Franca, F. Onori, F. Ricci, E. Sani, M. Brusa, R. Maiolino, S. Bianchi, A. Bongiorno, F. Fiore, A. Marconi and C. Vignali, "Extending Virial Black Hole Mass Estimates to Low-Luminosity or Obscured AGN: the cases of NGC 4395 and MCG 01-024-012", MNRAS, 2014 *Submitted*).

- Brusa, M.; Bongiorno, A.; Cresci, G.; Perna, M.; Marconi, A.; Mainieri, V.; Maiolino, R.; Salvato, M.; Lusso, E.; Santini, P.; Comastri, A.; Fiore, F.; Gilli, R.; Franca, F. La; Lanzuisi, G.; Lutz, D.; Merloni, A.; Mignoli, M.; Onori, F.; Piconcelli, E.; Rosario, D.; Vignali, C.; Zamorani, G. (2015), " X-shooter reveals powerful outflows in z $\sim$1.5 X-ray selected obscured quasi-stellar objects", MNRAS, 446, 2394-2417.
- Bianchi, Stefano; Panessa, Francesca; Barcons, Xavier; Carrera, Francisco J.; La Franca, Fabio; Matt, Giorgio; Onori, Francesca; Wolter, Anna; Corral, Amalia; Monaco, Lorenzo; Ruiz, Angel; Brightman, Murray (2012), " Simultaneous X-ray and optical observations of true type 2 Seyfert galaxies", MNRAS, 426, 3225-3240.

É una follia odiare tutte le rose perché una spina ti ha punto, abbandonare tutti i sogni perché uno di loro non si é realizzato, rinunciare a tutti i tentativi perché uno é fallito. É una follia condannare tutte le amicizie perché una ti ha tradito, non credere in nessun amore solo perché uno di loro é stato infedele, buttare via tutte le possibilitádi essere felici solo perché qualcosa non é andato per il verso giusto. Ci sará sempre un'altra opportunitá, un'altra amicizia, un altro amore, una nuova forza.
Per ogni fine c'é un nuovo inizio.

Antoine de Saint-Exupéry, Il piccolo principe.